Aerodynamic Performance Measurements of a Film-Cooled Turbine Stage

by

Rory Keogh

B. Eng., Mechanical Engineering, University College Galway, (June 1989)
S.M., Aeronautics and Astronautics, Massachusetts Institute of Technology, (February 1998)

Submitted to the Department of Aeronautics and Astronautics
in partial fulfillment of the requirements for the degree of

Doctor of Philosophy
at the
Massachusetts Institute of Technology

February 2001

Author _____
Department of Aeronautics and Astronautics
November 29, 2000

Certified by _____
Dr. Gerald R. Guenette
Principal Research Engineer, Committee Chairman

Certified by _____
Professor Alan H. Epstein
R. C. Maclaurin Professor of Aeronautics and Astronautics

Certified by _____
Professor Jack L. Kerrebrock
Professor of Aeronautics and Astronautics, Emeritus

Accepted by _____
Professor Nesbitt W. Hagood
Associate Professor of Aeronautics and Astronautics
Chairman, Department Graduate Committee

Aerodynamic Performance Measurements of a Film-Cooled Turbine Stage

by

Rory Keogh

Submitted to the Department of Aeronautics and Astronauticson November 29, 2000,
in partial fulfillment of the requirements for the degree of Doctor of Philosophy

Abstract

The goal of this research is to measure the aerodynamic performance of a film-cooled turbine stage and to quantify the loss caused by film-cooling. A secondary goal of the research is to provide a detailed breakdown of the losses associated with film-cooling for the turbine stage being tested.

The experimental work was carried out at the MIT Blowdown Turbine Facility using a highly loaded turbine stage. The Blowdown Turbine Facility is a short duration test facility capable of testing turbine stages under fully scaled conditions for a test duration of 0.5 seconds. The facility was modified to enable the measurement of the turbine mass flow and shaft torque. These newly developed measurement techniques, along with previously developed total pressure and temperature instruments, have enabled the measurement of the stage isentropic efficiency. A highly loaded turbine stage (without film-cooling) was designed, fabricated, and tested using the newly developed measurement techniques. The turbine stage was then modified to incorporate vane, blade and rotor casing coolant manifolds using precision electrical discharge machining. The film-cooling hole geometry was created using a laser drilling process to produce the required 43,000 cooling holes. The film-cooled stage was then tested over a range of operating conditions (pressure ratios and corrected speeds) and over a range of coolant-to-mainstream mass flow and temperature ratios.

The loss due to film-cooling is defined as the difference in performance between the film-cooled turbine and an ideal turbine with the same velocity triangles and airfoil Mach number distributions. However, there is no uncooled turbine geometry that will produce the same flow conditions as the film-cooled turbine stage, and consequently, there is no experimental baseline that can be tested to determine the loss due to film-cooling. A meanline velocity triangle model of the turbine stage was developed using published correlations and loss models to estimate the performance of this ideal stage. The model was calibrated against the baseline test results without coolant and it was then used to estimate the loss due to film-cooling.

The estimated loss due to film-cooling was 3.0% at the design point, which corresponds to 0.3% per percent of coolant. The estimated repeatability (U_{95}) for the efficiency measurement of the uncooled turbine geometry is $\pm$ 0.14%. Based on this measurement repeatability, the net effect of a design change can be determined with an uncertainty of just $\pm$0.1% if four measurements are repeated for each design configuration. The estimated measurement uncertainty for the film-cooled stage efficiency is 0.55% and for back-to-back measurements the uncertainty is 0.45%.

Thesis Supervisor: Dr. Gerald R. Guenette
Title: Principal Research Engineer

Acknowledgments

I would like to express my gratitude to Dr. Gerald R. Guenette for his guidance and direction throughout the course of this research. I also wish to thank Professor Alan H. Epstein for his guidance, and for being a great teacher and mentor; to Professor Jack L. Kerrebrock who's guidance and feedback is gratefully acknowledged.

I would also like to thank all the members of the 'pit crew' who contributed to the success of this research. They include; Chris Spadaccini, Jason Jacobs, Léo Grépin, and Yi Cai. Also a special thanks to James Letendre, Viktor Dubrowski, and Bill Ames for their invaluable assistance in running this experiment; to Mariano Hellwig and Tom Ryan for their instrumentation assistance; to Holly Anderson for all the money.

I wish to thank all the Engineers of Alstom Power (formerly ABB) who contributed to this research, especially Dr. Thomas P. Sommer. Also all of the vendors, without who's efforts this work would not have succeeded; Laser Services Inc., Johnson Precision Inc., Peterson Machine Corp., and Mal Tool.

In addition would like to thank the students of the Gas Turbine Laboratory who have made my experience here an enjoyable one, especially; Zolti, Luc, Amit, Adam, Asif, John, Bret, Jinwoo, and Duncan; also a special thanks to Lori Martinez for improving the atmosphere for all of the students at the Lab; and to Dr. Choon Tan for all of the insightful discussions over the past five years.

Finally I'd like to thank my family for all of their support, especially my wife Glenna for her forbearance while I pursued my dreams.

Contents

List of Figures

List of Tables

Nomenclature

Roman

h	Specific enthalpy (J/kg)
s	Specific entropy (kJ/kgK)
I	Rotor inertia $(kg\,m^2)$
A	Area (m^2)
L	Characteristic length scale (m)
M	Mach number
	Mass of test gas between turbine and venturi (kg)
P	Pressure (Pa)
Re	Reynolds number
T	Temperature (K)
U	Velocity (m/sec)
V	Volume (m^3)

Greek

α	Swirl angle (rad)
β	Flow exit algle (rad)
ϵ	Total blade turbing (rad)
η	Efficiency
γ	Specific heat ratio
ν	Kinematic viscosity (m^2/sec)
ω	Angular speed (Hz)
Ω	Angular speed (rad/sec)
ϕ	Equivalence ratio
ρ	Density (kg/m^3)

θ	Momentum thickness (m)
τ	Time constant (sec)
δ^*	Displacement thickness (m)
ζ	Entropy loss coefficient

Subscripts

a	Turbine inlet
c	Turbine exit
	Compressor
	Coolant
b	Rotor inlet (NGV exit)
is	Isentropic
g	Upstream
h	Heatshield (or Casing)
n	Nozzle guide vane
r	Rotor
	Turbine radial exit location
m	Mixed out
t	Total conditions
	Turbine
th	High pressure turbine
	NGV throat
tl	Low pressure turbine
s	Stored between turbine and venturi
pr	Due to pressure loss
T	Tangential

Full quantities

Cp	Specific heat at constant pressure (J/kgK)
C_d	Discharge coefficient
C_{*i}	Ideal gas critical flow coefficient
C_r	Real gas critical flow coefficient

N_c	Corrected speed, % of design
P_c	Corrected power, % of design
W_c	Corrected mass Flow, % of design
L_{ref}	Reference length (m)
$\dot{m}$	Mass flow rate (kg/sec)
η_{adia}	Adiabaticity efficiency
P_t	Total pressure (Pa)
P_b	Base pressure (Pa)
$\mathcal{P}$	Turbine power (W)
$\mathcal{P}_{Ideal}$	Ideal turbine power (W)
$\dot{Q}$	Heat loss (W)
Re_d	Reynold's number of critical flow ventui nozzle
T_t	Total temperature (K)
$\mathcal{T}$	Turbine Torque (Nm)

Acronyms

$ASME$	American Society of Mechanical Engineers
$ANSI$	American National Standards Instituite
BDT	Blowdown Turbine
$CEESI$	Colorado Experimental Engineering Station, Inc.
CFD	Computational Fluid Dynamics
$CFVN$	Critical Flow Venturi Nozzle
$CO2$	Carbon Dioxide
DAQ	Data Acquisition System
DC	Direct Current
ECB	Eddy Current Brake
EDM	Electrical Discharge Machining
GTL	Gas Turbine Laboratory
HPT	High Pressure Turbine
$MISES$	Multiple blade Interacting Streamtube Euler Solver
MIT	Massachusetts Institute of Technology
$NIST$	National Institute of Standards and Technology
NGV	Nozzle Guide Vane
NPV	Net Present Value

RTD Resistance Temperature Detector

Chapter 1

Introduction

1.1 Motivation

To meet the demand for higher power densities from gas turbine systems, designers have devoted much effort over the past half-century toward increasing turbine inlet temperature. This has been accomplished through the development of both extraordinary turbine and disk materials and sophisticated internal and external cooling arrangements. The aerodynamic performance of turbines has likewise increased enormously, leading to polytropic efficiencies in the low 90% range. This efficiency increase has come through improved design techniques based on a better understanding of the fluid mechanics of turbines and the application of increasingly more powerful computational tools.

With the gas temperature much higher than the turbine material can tolerate, cooling must be applied to keep the metal temperature close to uniform and within allowable limits, to avoid thermal stress and surface oxidation, and to control the life of the parts. For this purpose, elaborate cooling schemes have been devised that distribute cooling air around the airfoil surface, using relatively cool air extracted from the compressor. Figure 1-1 illustrates the different cooling schemes that can be implemented individually or in combination. They include: internal convective cooling, internal impingement cooling, and film-cooling. Internal cooling (cooling airflow inside the hollow turbine airfoil) aims at absorbing the heat conducted into the blade thereby reducing the blade temperature without affecting the external fluid dynamics. Film-cooling, on the other hand, bleeds coolant air through holes or slots on the airfoil surface, forming a thin 'film' barrier between the hot surrounding gas and the blade. High pressure first stage turbines often use as much as 15-20% of compressor core mass flow as cooling air, with considerable penalties on turbine aerodynamics. In this context, it is highly desirable to optimize the cooling distribution and effectiveness and minimize the cooling flow requirement.

Modern state of the art commercial transport engines have turbine inlet temperatures of over 1700K, and it is higher for military engines with shorter turbine life. This temperature level, however, is much less

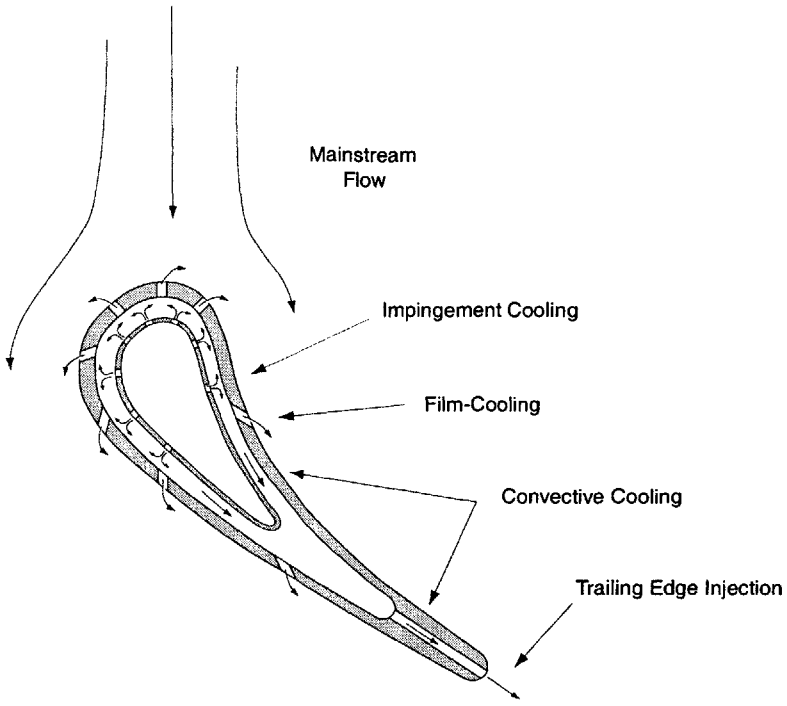

Figure 1-1: Nozzle guide vane cooling schemes.

than the stoichiometric combustion temperature of ≈2500K [1], so that there is still a substantial margin for improvement. The benefits to be achieved from the employment of progressively more elaborate external film-cooling schemes must be weighed against a variety of design issues. One critical issue is the impact of main flow/coolant flow interactions on turbine aerodynamic performance. The increase in turbine inlet temperature has come at the expense of turbine aerodynamic efficiency. The ability to quantitatively measure such penalties, however, has always been in question.

Many investigations on the interaction of the coolant flow with the turbine main flow have focused on the heat transfer problem. This is understandable given that small changes in the inlet temperature produce dramatic changes on the cycle performance and on the structural integrity and life of the highly stressed turbine components. Achieving the desired balance between these competing factors is a challenging task in the design process.

It is worthwhile illustrating the degree to which increased turbine inlet temperatures improve the cycle performance. Two figures of merit commonly used to describe the performance of a gas turbine are the cycle efficiency and the specific work. Figures 1-2(a) and 1-2(b) show the cycle efficiency and specific work for the simple cycle depicted in figure 1-2(a). This illustrative example assumes that the turbine heat load is proportional to the difference between the mainstream and metal temperatures, and a constant cooling system effectiveness. The assumptions are presented in Appendix A. Three examples are shown: the first assumes an ideal turbine that does not require cooling, the second is for a turbine that is cooled but without

[1] For hydrocarbons with $\phi = 1.0$, $\pi_c = 25$ and $\eta_c = 0.89$

incurring any additional loss, and the third is a turbine with cooling and loss. The efficiency of the cooled turbine with additional cooling system loss is assumed to decrease by 0.3% for each percent of coolant flow[2]. The cycle efficiency and specific work increase dramatically with turbine inlet temperature for the ideal turbine. The improved cycle efficiency and specific work are offset significantly for the cooled turbine. The additional reduction in efficiency and specific work is small for the cooled turbine with increased loss. For this simple example, the cycle efficiency cannot be increased past $\approx 1700K$ if compressor discharge air is used to cool the turbine. However, the specific work continues to increase up to a turbine exit temperature of $\approx 2300K$. Both the cycle efficiency and specific work can be increased significantly by reducing the amount of compressor air required to cool the turbine.

The reduced cycle efficiency due to a drop in HPT efficiency is small compared to the direct impact of cooling on the cycle performance. Only 20% of the reduction in cycle efficiency (when comparing the ideal turbine and the cooled turbine with additional HPT loss) is due to the additional HTP loss. The remaining 80% is due to the use of compressor discharge air as a heat sink for the cooled turbine. From a cycle perspective, this flow goes through the system and incurs loss without producing any useful work. This simple example illustrates why so much attention has been focused on improving cooling effectiveness and thereby reducing the coolant flow rate, and comparatively little attention has been focused on the impact of coolant injection on the turbine performance. Figures 1-2(a) and 1-2(b) appear to suggest that the impact of cooling on the turbine performance is a second order effect.

So why try and quantify this loss with a greater degree of accuracy than can be obtained through experience based on past designs? The answer is based on business and not technical considerations alone. Companies that design and manufacture gas turbines are often required to sell their product to launch customers when the design is in the preliminary design phase, and there is a high degree of uncertainty associated with the predicted performance. Any shortcomings in the performance of the delivered product result in penalties against the manufacturer. These penalties are intended to protect the operator from unreasonable performance claims by the manufacturer.

It is worthwhile considering a financial example to illustrate how a shortfall in the performance of the delivered product will impact the net income of the gas turbine operator. Figure 1-3 contains the results of a simple worksheet that illustrates how a one-percent shortfall in the HPT performance affects the net income of a utility that operates a single 179MW simple cycle gas turbine. The net income for the utility is the difference between two large numbers, so a small shortfall in performance can have a dramatic impact on the net income. A one-percent drop in the HPT efficiency results in a reduced NPV income, over the 30 [3] years that the gas turbine will operate, of 7 million dollars. This corresponds to approximately 20% of the cost of the gas turbine, which is a major component of the overall cost of the plant. If the penalties incurred are commensurate with the cost to the operator, it is reasonable to assume that a one-percent shortfall in

[2]This assumption is shown to be reasonable in Chapter 5.

[3]This example assumes a discount rate of 10% and that fuel, O&M and electricity prices increase at 2.5 % per annum. The sources for the fuel, o&m, electricity and capital equipment costs are cited in reference [15].

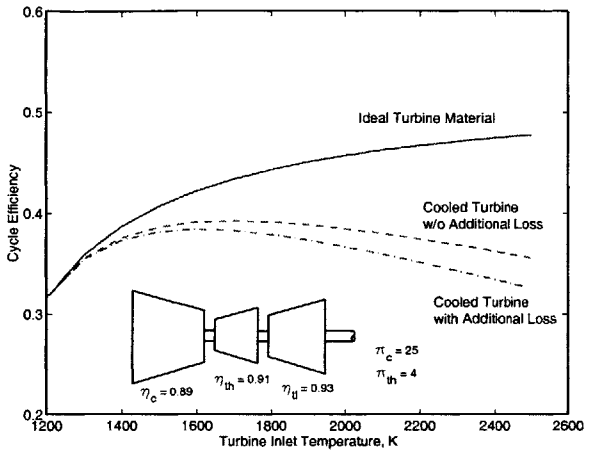

(a) Cycle Efficiency vs. Turbine Inlet Temperature (Illustrative).

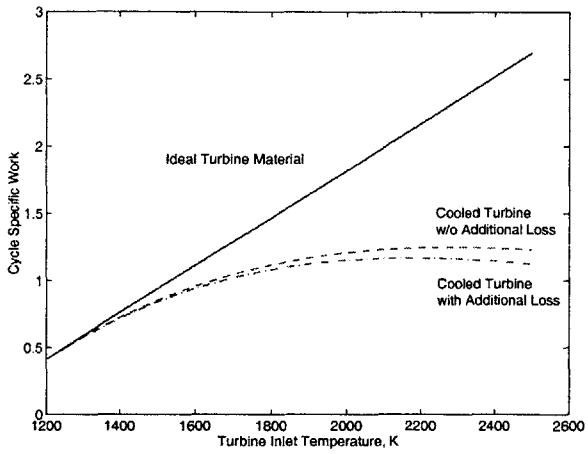

(b) Cycle Specific Work vs. Turbine Inlet Temperature (Illustrative).

Figure 1-2: Simple Cycle Analysis.

the cooled turbine efficiency would eliminate a substantial portion of the profit from the sale of the gas turbine. Gas turbine manufacturers cannot simply be conservative with their performance predictions, as this will result in lost sales and a failure to capitalize on the true performance of the design. Any error in performance predictions will result in reduced profits for the gas turbine manufacturer. With this in mind, the uncertainty associated with the turbine loss due to cooling has very serious implications for the development of new and derivative gas turbines. The current research is motivated primarily by the uncertainty associated with the loss due to turbine cooling.

1.2 Previous Work

Relatively few detailed experimental studies have been published that investigate the performance penalties due to film-cooling in turbines. The following three studies have measured the loss due to cooling:

- Vlasic et al. (1996) tested a high work single-stage research turbine with a pressure ratio of 5.0, and a stage loading of 2.2, and a cooled rotor and stator. The tests were carried out in a cold flow test rig and a meanline efficiency audit was used to compare the results with a gas generator test rig. The effect of cooling, as measured in the cold flow rig, reduced the turbine efficiency by 2.1%. The nozzle guide vane cooling scheme used showerhead film-cooling and an internal cooling passage with pressure

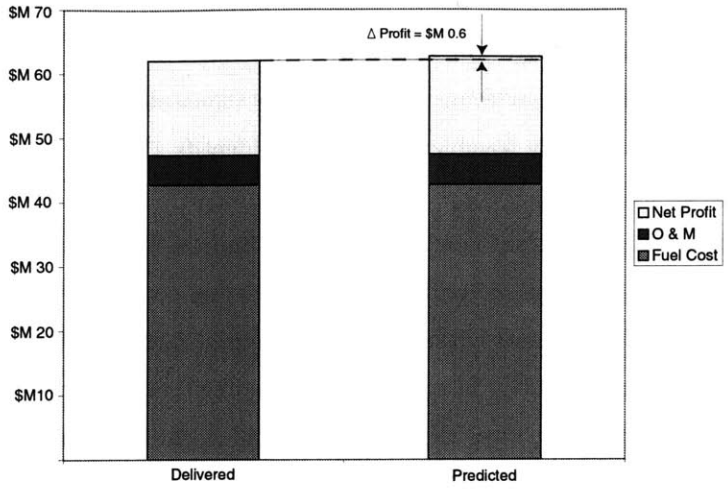

Figure 1-3: Simple Cycle GT Yearly Revenue and Costs

surface ejection. The rotor cooling used a multipass configuration with trailing edge injection. The vane and blade cooling flow rates were 7.5% and 3.5% respectively, as a percentage of the vane inlet flow.

- Nouse et al. (1975) investigated the influence of turbine cooling on the performance of a two-stage axial turbine with an overall pressure ratio of 4.08. The aerodynamic characteristics of the two-stage turbine without coolants were tested in a cold flow test rig. The first stage of the two stage turbine was then tested with coolants in a gas generator test rig. The nozzle guide vane and rotor used a combination of internal convective cooling and trailing edge ejection. The total cooling flow rate was 8.9%, 2.5% of which was rotor cooling. The first stage uncooled efficiency was estimated using stationary interstage total pressure and temperature measurements. Comparing this with the cooled single stage efficiency, the authors estimated an efficiency reduction of 8.3% due to cooling.

- Crow et al. (1980) tested a turbine, uncooled and with stator and rotor cooling, as part of the joint P&W-NASA Energy Efficient Engine (E3) program. They demonstrated an efficiency drop of 2.5% due to cooling. This result was reported by Vlasic (1996). The reference cited by Vlasic reported the uncooled measurements only. The cooling configuration studied by Crow was not published.

The stage cooling configuration studied in this thesis is more advanced than those studied by Vlasic and Nouse. The NGV cooling consists of 'full coverage' film-cooling, which consists of shower head, pressure and suction surface film-cooling, trailing edge ejection, and endwall film-cooling. The rotor blades have leading edge ejection, and pressure and suction surface film-cooling.

1.3 Objective and Approach

The goal of this research is to measure the aerodynamic performance of a film-cooled turbine stage and to quantify the loss caused by film-cooling. The main challenges are; Firstly, to develop a method of testing the turbine stage that models all of the relevant fluid physics, is repeatable enough to be measure the impact of design changes, and is economically feasible; Secondly, to identify the loss caused by film-cooling from the overall performance measurement.

Detailed experimental study of coolant flow interactions is impossible in the engine operational environment as a result of the extremely high temperatures and oxidizing conditions present in engine turbines. The technology to perform measurements within this environment at the required level of detail and accuracy is well beyond our current capability. In an effort to overcome these limitations a technology based on short duration testing was developed. Over the past two decades, short duration test facilities have been successfully used to study turbine heat transfer phenomena. The planned approach for the current research program was extend the measurement capabilities of the short duration test facility to include the ability to make stage efficiency and mass flow measurements. These new measurement techniques could then to be used to study how film-cooling affects the aerodynamic performance of a film-cooled turbine stage.

It is difficult to identify the loss caused by film-cooling from the overall performance measurement. To extract the loss due to film-cooling, the results should be compared with an ideal stage that has the same velocity triangles and airfoil Mach number distributions, but without coolant injection. However, the film-cooling flow is an integral part of stage design and it is required to maintain the airfoil Mach number distributions and stage reaction. If the stage is tested without coolant, the reaction rate will decrease and the resulting efficiency will be lower than that of the ideal stage. If the blockage caused by film-cooling was known, the airfoil profile and endwall contours could be redesigned to account for the coolant deficit, and thereby maintain Mach number distributions and boundary layer parameters, similar to the ideal stage. However, this would result in larger airfoil trailing edge thicknesses, an increased trailing edge loss and a change in the trailing edge deviation angle. As the trailing edge loss is one of the most poorly understood turbine loss mechanisms, a change in the trailing edge thickness is not desirable. Also the blockage caused by coolant injection cannot be precisely predicted. There is no uncooled turbine geometry that would give the same Mach number distributions and stage velocity triangles as the film-cooled stage (if an approximate uncooled geometry was available it could only be used to simulate a single coolant flow rate). Consequently, there is no experimental baseline that can be tested to directly determine the loss due to film-cooling.

Alternatively, an analytical model of the stage meanline velocity triangles can be used to predict the performance of the ideal stage, and thereby estimate the loss due to film-cooling. In the current study, the uncooled geometry was tested (i.e. the same blades without cooling holes), and the results were used to calibrate a meanline velocity triangle model of the stage. This model was then used to estimate the performance of the ideal stage and the losses due to film-cooling. This model was subsequently used to provide a detailed breakdown of the cooling losses and also to identify the cooling system losses that are

unique to the MIT blowdown turbine facility.

1.4 Thesis Outline

The remainder of the thesis is organized into the following chapters.

The experimental apparatus used for the current research program is discussed in Chapter 2. The basics of the blowdown turbine facility and the test turbine procedures are described. Particular emphasis is given to the newly developed instrumentation to measure the turbine stage mass flow and shaft torque. The results of the two experimental test series are presented in Chapter 3. The data reduction procedure and the assessment of data accuracy are also presented. Chapter 4 presents the definition of turbine efficiency used for the experiment and the analytical models. In Chapter 5 a meanline velocity triangle model of the turbine stage is used to estimate performance of an ideal turbine stage without cooling, that has the same velocity triangles and work output as the film-cooled stage. Chapter 6 presents a detailed breakdown of the losses associated with film-cooling. A final summary and conclusion are provided in Chapter 7, with the contribution of this thesis outlined. Recommendations for future work are also discussed.

Chapter 2

Blowdown Turbine Test Facility

2.1 Introduction

The MIT Blowdown Turbine Facility is a short-duration, blowdown wind tunnel capable of testing a complete, rotating stage in an environment which rigorously simulates the fluid physics and heat transfer phenomena that occur in a turbine. This chapter reviews the MIT Blowdown Turbine facility. Overall configuration and operational procedures are described. Scaling of the turbine operating point to achieve full scale similarity is discussed. The individual components of the facility are examined as well as instrumentation and the recently modified coolant feed system. The data acquisition system is also briefly presented.

2.2 Facility Configuration

2.2.1 Introduction

The MIT Blowdown Turbine test facility is shown in Figure 2-1. The facility consists of seven primary components: the supply tank, fast acting valve, test section, eddy current brake torque meter, critical flow venturi nozzle, coolant feed system (not shown), and dump tank. A detailed review of the overall design of the facility can be found in Guenette [8].

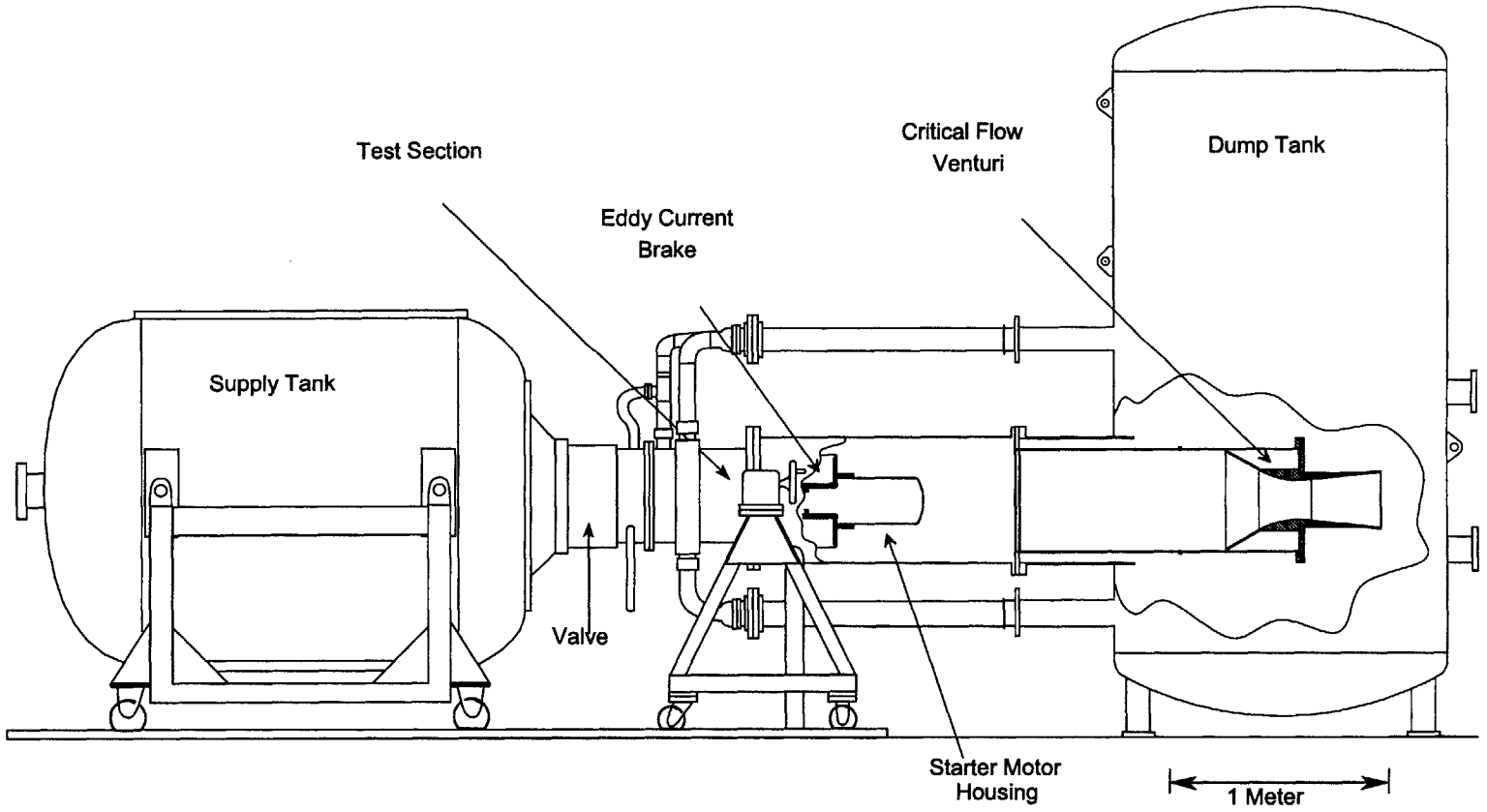

Figure 2-1: MIT Blowdown Turbine Facility

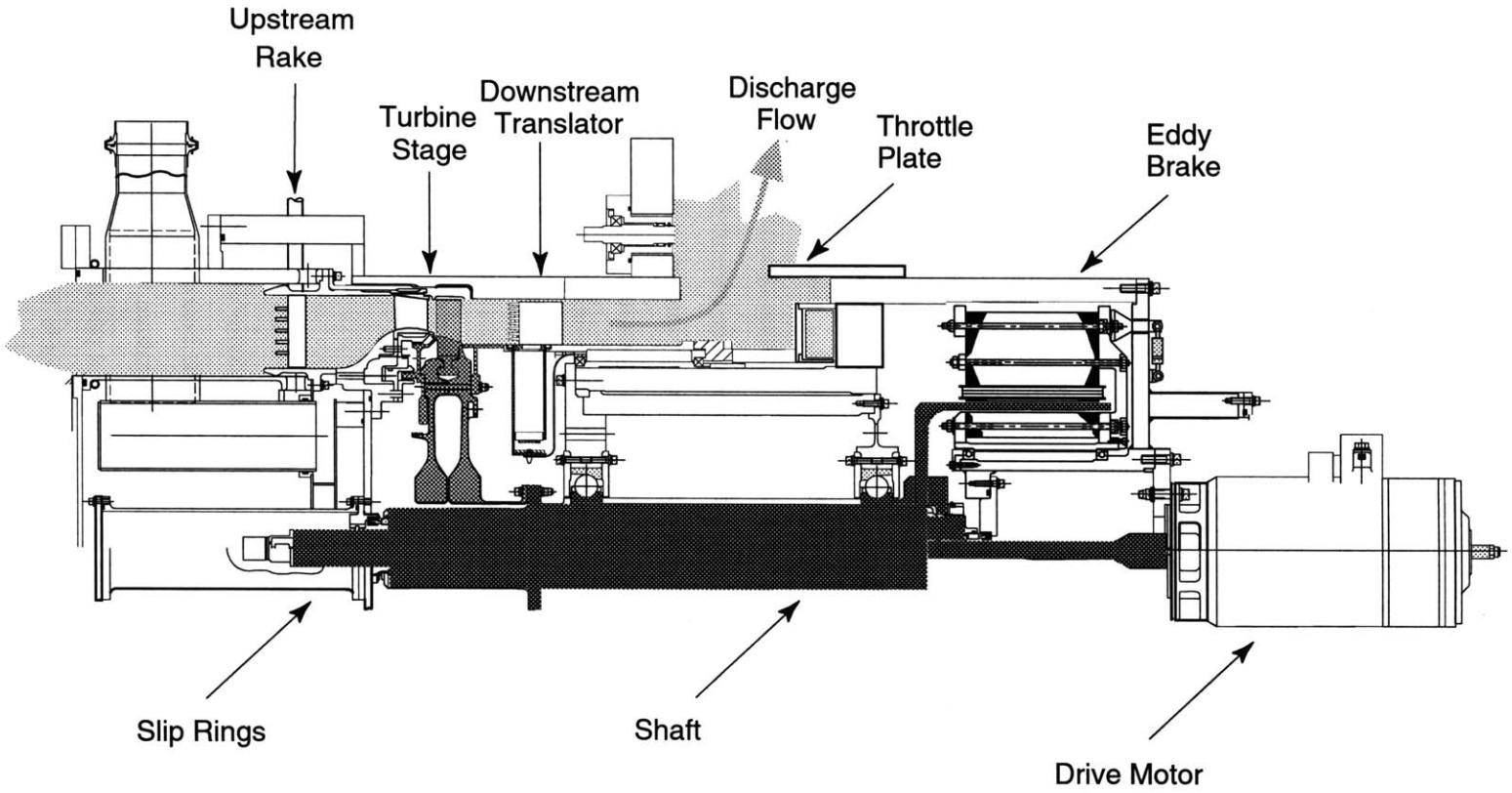

Figure 2-2: Test Section Flow Path

2.2.2 Supply Tank and Fast Acting Valve

The supply tank is a 364 cubic foot cylindrical pressure vessel rated at 150 psi. It is surrounded by an external jacket through which heat transfer oil is circulated to heat the tank to the desired test temperature. A stirring fan is employed to ensure a uniform test gas temperature distribution. The test section is separated from the supply tank by a fast-acting, axially traversing, plug valve. This valve is designed to fully open in approximately 50 milliseconds and introduce disturbance-free flow into the test section. Valve dynamics are controlled by damping chambers which produce a force on the plug whose magnitude and direction depend on its position and velocity. In its fully closed position, this force acts to seal the plug. After the seal is broken, the valve plug is accelerated open. As it nears its fully open position the plug is decelerated to rest. The force used to break the seal is provided by an internal pneumatic piston assembly actuated by a small compressed gas cylinder.

2.2.3 Turbine Test Section

A cut-away of the test section assembly is shown in Figures 2-3 and 2-2. The test section is composed of the forward frame, main frame, and the rotor unit. The forward frame contains the nozzle guide vanes, NGV coolant supply plenum and the inlet boundary layer bleeds and mates to the main valve. The forward frame is followed by the main frame which houses the turbine rotor assembly, the downstream probe translator package, the eddy current brake magnet assembly, the turbine throttle and drive motor. The rotor unit contains the rotor discs, blades, bearings, shaft, and the eddy current brake 'loss' drum (not shown). As shown in Figure 2-2, the loss drum is inserted into the eddy current brake magnet assembly.

A cross-sectional view of the test section flow path is shown in Figure 2-2. Upstream of the turbine stage a boundary layer bleed provides clean inlet flow. The rotor exit flow is exhausted through an adjustable throttling area to provide the desired pressure ratio across the turbine. Also shown in this figure are the upstream and downstream measurement locations (upstream rake and downstream translator). Downstream, the total temperature and pressure probes are mounted on a circumferential translator.

2.2.4 Downstream Translator

Both upstream and downstream circumferential translators are available to provide measurement of non-axisymmetric features of the turbine flow field. Both are composed of drums forming the inner annulus of the turbine entrance and exit and are mounted on thin-line bearings. For the experiments reported herein only the downstream translator was employed. The downstream translator houses three 'canisters', spaced 20° apart, which contain the appropriate the electrical and pneumatic connections to support either total temperature or pressure rakes. Connections are also provide for several wall static pressure taps. The translator is restricted to a 350° rotation angle, by a spring loaded hard stop, to prevent the translator from freely spinning and destroying the canisters' electrical wiring. The translator is driven by a Baldor

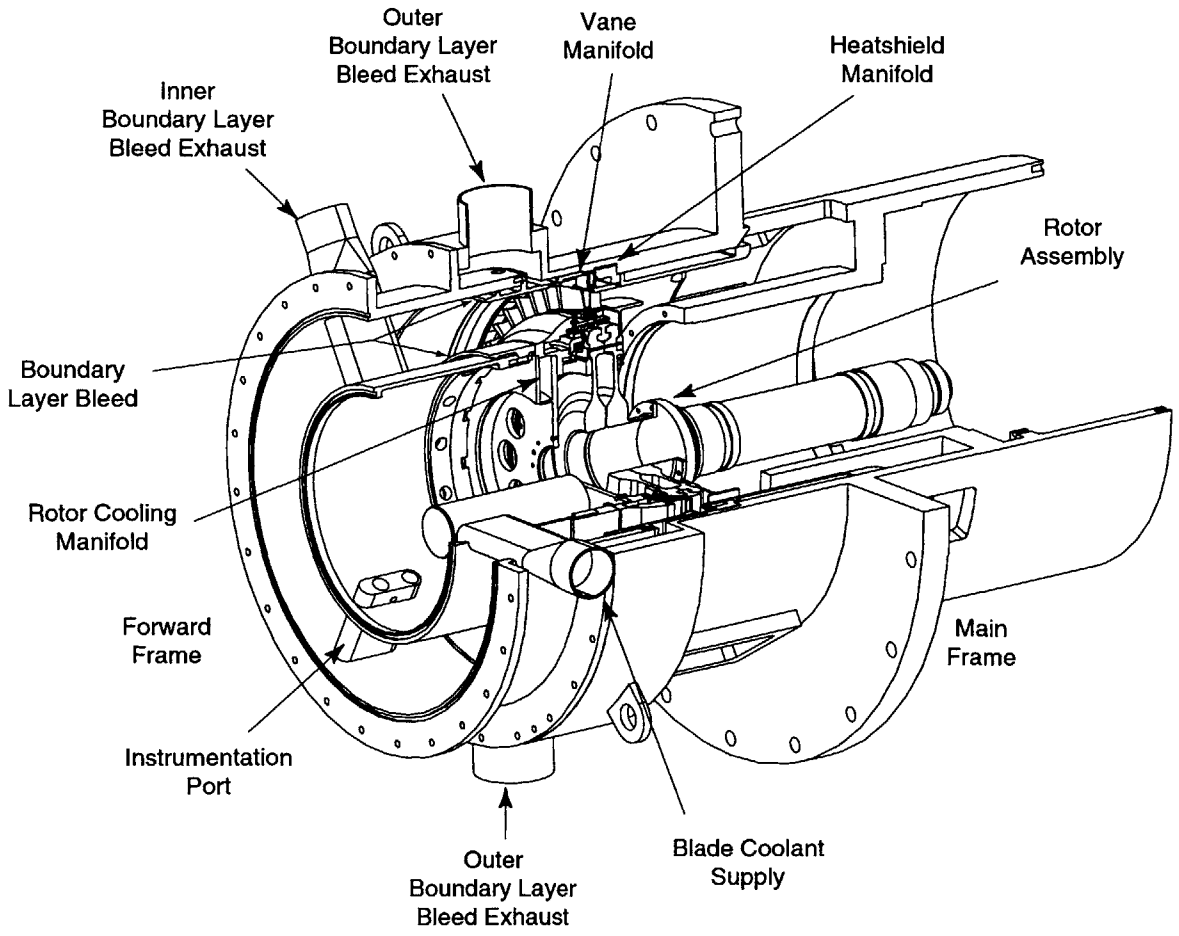

Figure 2-3: Test Section Detail

ME-4090-BLBCE servomotor delivering approximately 3(in-lb) of torque through an equivalent 13.5:1 gear ratio. This motor is controlled by a Galil DMC-400-10 card and powered by a Copley MB6-10 amplifier. In addition to the hard stop, an aluminum shear pin is installed on the shaft coupling exiting the servomotor to prevent translator runaway.

2.2.5 Eddy Current Brake Torque Meter

The eddy current brake serves as both the turbine load and the turbine torque meter. It consists of two components, a cylindrical, Inconel drum directly attached to the rotor shaft and a stationary array of DC excited electromagnets arranged circumferentially around the drum. Electric currents are induced in the drum as it rotates through the applied magnetic field. The flow of this current through electrical resistance of the drum dissipates the power produced by the turbine, which appears as resistive heating of the drum. Turbine speed is controlled by setting the magnitude of the applied magnetic field. The braking system was modified by Keogh [11] to serve as a shaft torque meter. The electromagnet assembly was mounted on bearings and force required to restrain the brake was measured using two load cells. Figure 2-4 shows a cross

section through the brake. A detailed description of the brake and its modification for torque measurement is presented in Section 2.6.5 of this thesis.

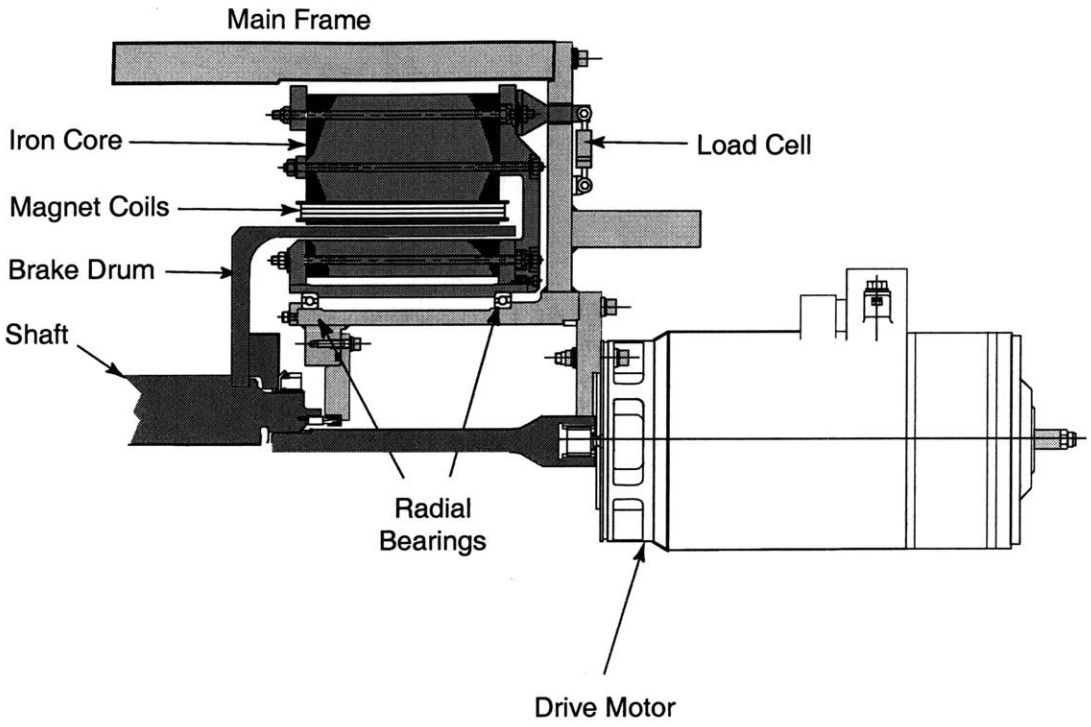

Figure 2-4: Eddy Current Brake

2.2.6 Critical Flow Venturi Nozzle

As part of this research, a critical flow venturi was developed and installed in line with the exit flow path to measure the mass flow rate through the turbine. The nozzle design and upstream duct requirements are based the ANSI standard [16] for toroidal throat critical flow venturi. Modifications to the facility were required to install the critical flow venturi nozzle. The main design challenge was to incorporate the required upstream duct length into the facility given the space restrictions. This was accomplished by installing the critical flow venturi and the upstream duct inside the dump tank (Figure 2-1). A 66 inch extension was added between the dump tank and main frame in order to relocate the eddy current brake and starter motor and provide a space to install the venturi inlet flow conditioning duct. Extensions were also required to connect the boundary layer bleeds to the dump tank, and to connect the fill system to the supply tank. A 50% open area screen is installed at the entrance to the upstream duct. This reduces the total pressure non-uniformity caused by the stepped transition from annular to circular cross section around the starter motor. The nozzle was calibrated with the upstream duct and a simulated blockage in place. The nozzle was designed and built by Flow Systems Inc. of Boulder Colorado and calibrated by Colorado Experimental Engineering Station Incorporated. This calibration is traceable to the National Institute for Standards and Technology (NIST). A cross-section of the critical flow venturi nozzle is shown in Figure 2-5 and a more detailed review of its design and usage can be found in Keogh [11].

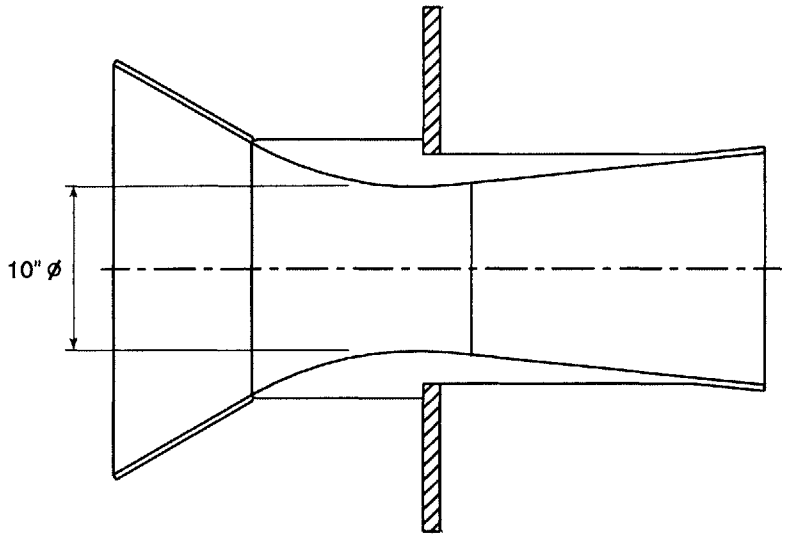

Figure 2-5: Critical Flow Venturi Nozzle

2.2.7 Coolant Feed System

The coolant system consists of a coolant supply tank, a fast-acting pneumatic ball valve, a pipe network, and several orifice plates for metering the flow. Like the facility itself, the cooling system operates in a blowdown mode. The existing facility coolant system was modified to provide three independent and

separately metered streams to the rotor blades, vanes, and tip casing. The coolant supply tank is 3.97 ft^3 and has a pressure rating of 450 psi. Like the main supply tank, it is surrounded by a metal jacket and insulation to controlling tank temperature. A flow of liquid nitrogen mixed with compressed air is used to cool the tank lining and the test gas to the desired temperature. The fast-acting ball valve at the tank exit is actuated by a 1000 psi argon bottle. It is triggered simultaneously with the main valve and closes approximately 1.2 seconds later. The piping network feeds the coolant from the supply tank into the test section and to the turbine.

Figure 2-6 shows a schematic of the cooling system. Three independent feeds are employed. One each to the rotor blades, nozzles, and tip casing. The flow is split in a manifold downstream of the ball-valve. Each split is metered by a thick, square edged, choked orifice with known discharge coefficient which accurately sets the mass flow ratios to each turbine component.

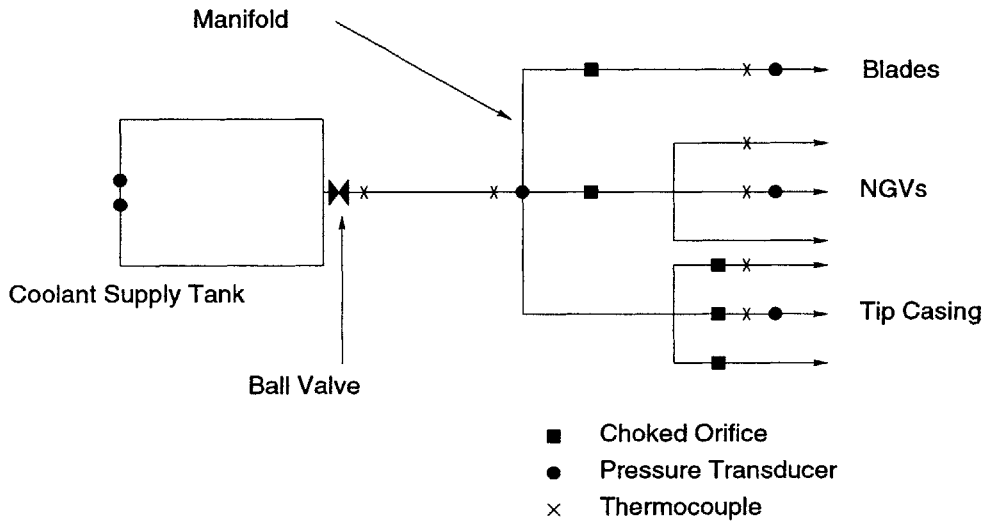

Figure 2-6: Coolant Feed System Schematic

2.3 Film-Cooled Turbine Stage Design

2.3.1 Introduction

This Section presents a description of the fabrication of the film-cooled turbine stage. In order to quantify the losses due to coolant flow injection, the $\frac{1}{4}$ scale film-cooled model turbine was required to have similar external geometry, including the film hole quantity, distribution, diameters, and injection orientations over the airfoil surfaces. The internal passages were not directly replicated since the focus the program was on external aerodynamic and heat transfer. After an initial series of tests were performed on the uncooled model stage, work then proceeded on the development and testing of the film-cooled version. As a result of programmatic considerations, it was decided to modify the existing solid un-cooled turbine airfoils. This was accomplished by the use of sophisticated machining techniques, such as electrical discharge machining

(EDM) and laser machining. Fabrication of the film-cooled turbine proved to be difficult, costly, and time consuming. The complex geometry of the holes and passages pushed existing manufacturing technologies to their limits. The cooling hole geometries and machining techniques will be reviewed here.

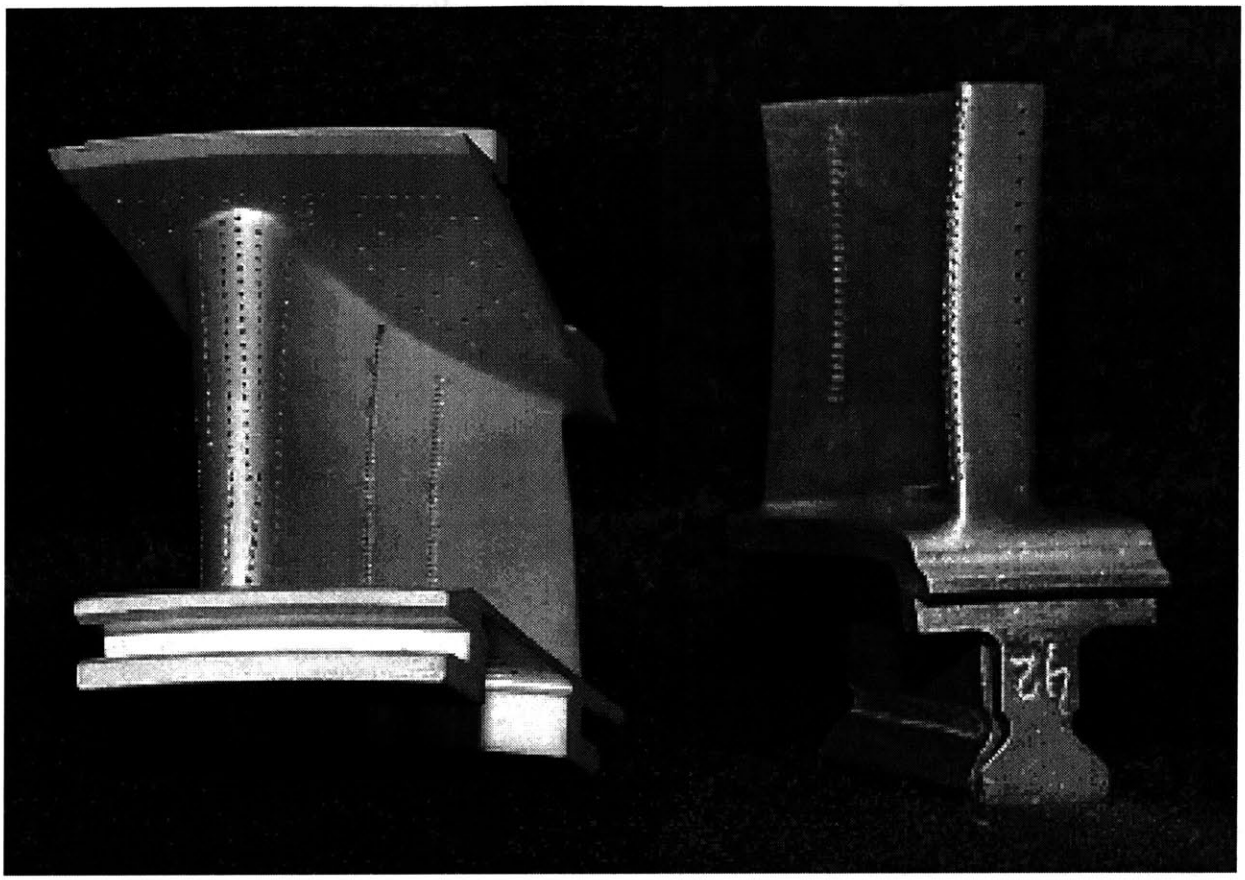

Figure 2-7: Film-Cooled Nozzle Guide Vane.

Figure 2-8: Film-Cooled Rotor Blade.

2.3.2 Film-Cooled Nozzle Guide Vane

The scaled film-cooled nozzle guide vane can be seen in Figure 2-7. The vane cooling configuration consists of 12 rows of coolant injection holes on the airfoil surface, as well as several holes on the upper and lower platforms. Table 2.1 summarizes the important features of this layout. Two vertical channels were required to feed all of the airfoil surface cooling holes. Coolant was supplied to the platform holes via manifolds above and below the locations where the vanes mate to the facility.

2.3.3 Film-Cooled Rotor Blade

The scaled film-cooled turbine blade can be seen in Figure 2-8. The blade cooling configuration consists of five rows of coolant injection holes: two on the leading edge, one on the suction surface and one on the

Table 2.1: Vane Cooling Holes

Row/Group	# of Holes	Diameter	Location
1	14	0.028"	Trailing Edge
2	44	0.008"	Pressure Surface
3	51	0.008"	Pressure Surface
4	26	0.008"	Pressure Surface
5	28	0.008"	Leading Edge
6	21	0.008"	Leading Edge
7	29	0.008"	Leading Edge
8	19	0.008"	Leading Edge
9	45	0.008"	Suction Surface
0	42	0.008"	Suction Surface
11	40	0.008"	Suction Surface
12	22	0.008"	Pressure Surface
A	107	0.008"	Outer Platform
B	91	0.008"	Inner Platform

Table 2.2: Blade Cooling Hole Arrangement

Row	# of Holes	Diameter	Location
1	17	0.008"	Suction Surface
2	29	0.008"	Leading Edge
3	29	0.008"	Leading Edge
4	26	0.008"	Suction Surface

pressure surface. The leading edge holes are also oriented at a compound angles. The numbers and sizes of the holes are summarized in Table 2.2.

The internal passages of the engine turbine blades have not been replicated. The purpose of this work is to study the effects of film-coolant injection; therefore, only simple manifold channels through the blade are needed. Two channels were used to feed the blade cooling holes; one for the leading edge and suction surface rows, and one for the pressure surface row. These passages provide a relatively constant wall thickness. The trailing edge holes proved too difficult to manufacture, as the design required a an 0.008" hole to be drilled through $\frac{1}{4}$ of material. The blade plenums were sealed at the blade tips by laser welding end caps onto the blade.

2.3.4 Film-Cooled Rotor Tip casing

The rotor tip casing (the outer annulus wall surrounding the blade tips) also requires film-cooling holes. The engine tip casing geometry could not be directly scaled and accommodated in the MIT Blowdown Turbine facility. As a result, a geometry, which provided the same coolant flow, but could be fabricated for use in the Blowdown Turbine, was devised. This configuration consists of two rows of film-cooling holes located at the leading and trailing edges of the tip-casing ring. There are 1544 leading edge holes with a 0.012"

diameter and 1200 trailing edge holes with a 0.015" diameter.

2.4 Test Procedures

Preparations for a blowdown experiment begin by determining the required conditions for achieving full-scale turbine operating point. These consist of the upstream total temperature and pressure, coolant total temperature and pressure, test gas composition, mechanical speed, throttle area, and brake excitation. The experiment then proceeds as follows:

1. The entire facility is evacuated and the throttle plate is positioned for a predetermined area based on operational experience.
2. The main supply tank is heated to the desired upstream total temperature and is brought to thermal equilibrium.
3. The main valve is sealed and the supply tank is filled with the required test gas mixture to the desired upstream total pressure.
4. Simultaneously, the coolant supply tank is filled to the desired pressure and cooled to the predetermined temperature.
5. At this post-fill state, all differential pressure transducers are calibrated by cycling their back-pressure ports between vacuum and atmosphere. This provides a scale factor for each transducer. Instrumentation and calibration are discussed in further detail in Section .
6. The brake excitation is set.
7. The data acquisition system and translator servo-motor controller are set to stand-by mode and are waiting to be triggered.
8. The turbine rotor is then accelerated to the desired mechanical speed by a starter motor.
9. Once this speed is exceeded, the motor is powered down and the rotor spins freely in the vacuum. It is slowly decelerated by bearing friction and the applied back EMF of the drive motor .
10. When the decelerating rotor reaches the preset speed, a trigger occurs causing the main valve and coolant ball valve to open. Simultaneously, the data acquisition system begins collecting data, the downstream translator begins it traverse, and the eddy current brake torque meter is energized.
11. The test gases then flow through the test section and quasi-steady state operation is reached after a 300 ms transient. The useful test window is approximately 500 ms.
12. After approximately 1.2 seconds the coolant ball-valve closes and the brake is turned off.

13. The rotor decelerates and comes to a stop.

14. Once the gas inside the tunnel stabilizes, all differential pressure transducers are re-calibrated to check for drift.

15. The tunnel is then re-evacuated and cooled to room temperature.

2.5 Facility Scaling and Setting Run Conditions

Validity of scaled wind tunnel experiments depends on similarity between the test flow and the actual flow being simulated. In dimensionless form, the equations for mass continuity, momentum and energy transfer produce nondimensional parameters which completely characterize the physics of flow field. Similarity between experiment and reality only requires that these nondimensional parameters be reproduced. For an un-cooled turbine stage operating under adiabatic conditions, corrected mass flow and total temperature ratio (or efficiency) depend on four dimensionless parameters: total pressure ratio, corrected speed, Reynolds number, and specific heat ratio [8]. Two additional parameters are required to simulate the heat flux distribution: the gas to wall temperature ratio and the Prandtl number. For a film-cooled turbine test, the coolant mass and momentum flux ratios must also be reproduced. These parameters, which govern test similarity, can be matched by properly setting the facility initial operating conditions. The operating conditions consist of the test gas composition, upstream total temperature and pressure, coolant total temperature and pressure, mechanical speed, throttle area, and brake excitation. The supply tank temperature is set by matching the gas to wall temperature ratio. Specific heat ratio is matched by setting the test gas mixture ratio, typically Argon and CO2. Shaft mechanical speed is set by matching the corrected speeds. Initial supply pressure is set by the Reynolds number, and pressure ratio by the downstream throttle position. Table 2.3 summarizes the conditions of a typical blowdown experiment and compares them to that of a full scale engine.

2.6 Instrumentation

2.6.1 Introduction

The facility was designed to provide a rather benign experimental environment for flow measurement. The nature of the short duration experiment places a strict requirement on the time response of instrumentation used to sample its flow field. These measurements also require a high level of instrumentation accuracy. These considerations led to the development of improved total temperature and pressure instrumentation with the capability of accurately characterizing turbine performance. The design of this new instrumentation is detailed by Cai [3]. An uncertainty analysis for the total temperature and pressure measurements is also presented by Cai. Following this is a brief explanation of other instrumentation used in the Blowdown

Table 2.3: MIT Blowdown Turbine Scaling

Parameters	Full Scale Engine	MIT BDT
Geometric Scale	1.0	0.25
Ratio of Specific Heats, γ	1.28	1.28
Working Fliud	*Air*	$Argon - CO_2$
Reynolds Number	5.6×10^6	5.6×10^6
Turbine Pressure Ratio	2.0	2.0
Inlet Total Pressure	15 *atm*	7 *atm*
Exit Total Pressure	7.5 *atm*	3.5 *atm*
Metal/Gas Temp. Ratio	0.65	0.65
Mean Metal Temperature	$1100K$	300 K
Inlet Total Temperature	$1700K$	464 K
Turbine Corrected Speed	100%	100%
Design Rotor Speed	$3600rpm$	$5954rpm$
Design Mass Flow	$312kg/s$	$23.3kg/s$
Turbine Power Output	$91MW$	$1.26MW$
Test Time	*Continuous*	$0.5sec$

Turbine. Finally, the standard differential pressure transducer calibration procedure is discussed followed by a description of the data acquisition system.

2.6.2 Total Temperature Instrumentation

The work of Cai focused on reducing the transient errors resulting from the heat transfer processes within the thermocouple junction support wires and led to a design with much faster time response than previously achieved. Attention was also paid to the probe head design to reduce probe sensitivity to flow angle, which is important for downstream wake measurements. The measurement heads consist of 0.0005 inch diameter type K thermocouple junctions mounted in vented stagnation tubes. The rake probe is mounted on the downstream translator and contains an internal temperature reference junction. An identical probe with four heads is also mounted on the downstream translator and a stationary six head version is mounted upstream of the turbine. The radial rake of 6 heads is positioned roughly mid-way between two of the facility's inner annulus support struts. The inlet rake can employ either an internally mounted or external reference junction. Three additional single head probes, spaced 120° apart, are mounted upstream at mid-span on the inlet annulus. The thermocouple reference junctions for these probes are external. Three total temperature probes are dedicated to monitoring the flow through the critical flow venturi nozzle. These probes are also 0.0005" diameter type K thermocouples and have similar time response and accuracy to the upstream probes. The cooling system is instrumented with seven type K thermocouples. These probes do not require the time response of the turbine inlet and outlet sensors and employ 0.003" junctions. These probes are located at points upstream of the choked metering orifices and as close as possible to where the coolant enters the test section. All thermocouples, with the exception of the turbine inlet and outlet rakes, are referenced to Omega TRCIII ice point cells. The signals are processed using high stability DC

amplifiers and filters prior to being recorded by the data acquisition system. The long term static accuracy of the system, (consisting of the measurement head, reference junction and signal conditioning electronics), is 0.13 K.

2.6.3 Total Pressure Instrumentation

The primary concerns in the design of the total pressure sensors for this facility are fast time response and flow angle insensitivity. The second criteria is particularly important for downstream measurements where the probes are circumferentially translated through the NGV wakes. To achieve the desired time response, semiconductor strain gauge type pressure transducers, manufactured by Kulite, were used. A disadvantage of these transducers is their tendency tend to drift with changes in temperature. As a consequence, extensive run-time calibration routines were developed and used during every experiment. To allow a larger range of inlet flow angle to the probe head, either vented Kiel type or 15° beveled impact heads were employed. Acceptable flow angles are estimated to be 27.5°.

Downstream of the turbine stage a rake type pressure probe, with eight 15° beveled impact heads, was employed to survey the pressure in the radial direction. The probe was mounted on the downstream translator to resolve flow characteristics in the circumferential direction. The pressure transducers, (100 psig XCQ-063- 100), are mounted inside the probe body below the heads. Transducer reference back pressure is provided via a tubing arrangement within the translator. The estimated average uncertainty in total pressure measurement from these heads is 0.25%. More information on the design of this probe is available in reference [3]. In addition to this rake, there are differential sensors located upstream of the turbine and in the supply, coolant, and dump tanks. There are also several highly accurate (0.05%) pressure sensors (manufactured by Sensotec) mounted throughout the facility for calibration reference. The coolant system is instrumented with several lower accuracy (0.1%) Sensotec transducers.

2.6.4 Other Instrumentation

The turbine speed and translator position were monitored by their respective digital encoders. The optical shaft encoder consisted of two rings of 366 divisions per revolution in quadrature and a once per revolution ring. It was directly mounted to the turbine shaft. Both digital and analog circuitry process the encoder signals to provide shaft position and velocity for storage by the computer data acquisition system.

Two piezoelectric sensors were mounted on the bearing housing to record shaft vibration during an experiment. The eddy current brake torque meter was instrumented with two load cells which provide a measure of shaft torque. The brake voltage and current are also recorded by the data acquisition system. A list of all instrumentation is provided in Table 2.4. Facility reference instrumentation provides known conditions for use in the calibration procedures. For these, time response was traded for absolute accuracy and stability as all tunnel temperature and pressure measurements are based on these references. Pressure references are available in the supply tank and test section via slower, but more accurate capacitive type

pressure transducers. Located on the supply tank was a Sensotec Super TJE 150 psi (0.05%) transducer. A Sensotec TJE 50psia (0.1%) transducer was located in the critical flow venturi. The upstream Pitot probes are referenced to a Setra Model 228 1 psid capacitive type pressure transducer. Temperature calibrations are referenced to a Rosemount Standard Platinum Resistance Thermometer Model 162N100A and, when possible, thermocouples are referenced to Omega TRCIII ice point calibration cells.

2.6.5 Shaft Power Measurement

Figure 2-9 shows the mechanical arrangement used to restrain and measure the eddy current brake torque. The eddy current brake was instrumented with two 3,000 lb Omega LCCA-3K S-beam load cells. The compact size of the S-beam load cells proved useful for this design. Rod end ball joints were use to eliminate side loads.

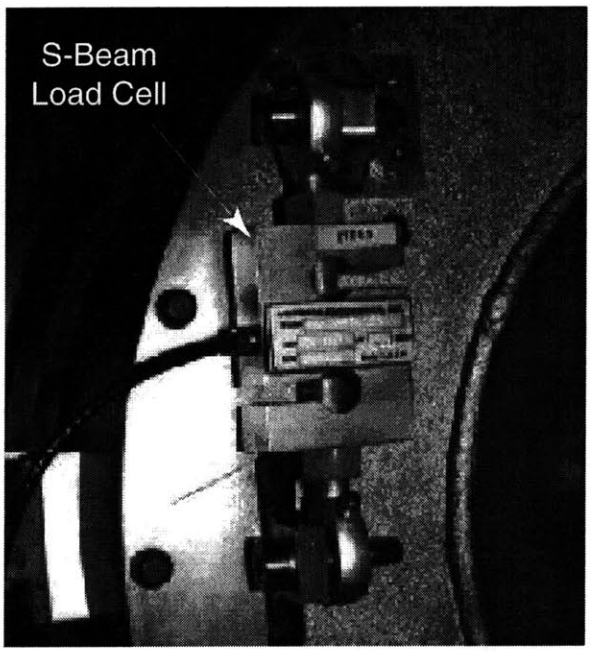

Figure 2-9: Eddy Current Brake Load Cell

2.6.6 Turbine Mass Flow Measurement

The critical flow venturi nozzle was instrumented with two of the 0.0005 inch type K thermocouples described in Section 2.6.2. The total temperature probes are installed 26 inches (one duct diameter) upstream of nozzle throat, as required by the ASME standard. A static pressure ring with four equally spaced static ports was also located at this measuring plane. The static pressure ring was connected to a Swagelok fitting located on the outer wall of the dump tank using flexible high pressure tubing to allow for ease of installation. The static pressure ring was instrumented with a 50 psi Sensotec TJE transducer. The upstream extension duct was also instrumented with two 0.0005 inch type K thermocouple probes, and the static pressure port

Table 2.4: Blowdown Turbine Instrumentation

Sensor	Type	Location
Facility Reference		
PFEF300	300 psi, Sensotec: STJE/1835/15 S/N: 589494	Calibration: Coolant Tank / Facility Run Time: Coolant Tank Initial Pressure
PREF150	150 psi, Sensotec: STJE/1833-12-04 S/N: 587965	Calibration: Supply Tank / Facility Run Time: Supply Tank Initial Pressure
PREF050	50 psi, Sensotec: TJE/0713-04TJA-12 S/N: 631656	Calibration: Facility Run Time: Critical Flow Venturi, Test Section Initial Pressure
PREF001	1 psid, Setra: 228-1 S/N:708984	Calibration: Inlet Pitot Tubes
TREF3997	Rosemount Model 162N100A, S/N3779 Std. Platinum Resistance Thermometer	Standard Calibration Reference
TREF10	0-100 C Platinum RTD	Run Time Reference
Supply Tank		
PT0A	150 psid, pressure, Kulite	Supply Tank, Internal
PT0B	150 psid, pressure, Kulite	Supply Tank, Internal
TT0A	600 F temperature, type J T/C	Supply Tank, Internal
TT0B	600 F temperature, type J T/C	Supply Tank, Internal
TT0C	600 F temperature, type J T/C	Supply Tank, Internal
Shaft Monitoring		
FTACH	Speed, Digital	Shaft/Bearing Assembly
ATACH	Speed, Analog	Shaft/Bearing Assembly
FBRING	Vibration, forward	Shaft/Bearing Assembly
RBRING	Vibration, rear	Shaft/Bearing Assembly
Eddy Current Brake		
VTOT	Excitation Volt	External
ITOT	Total Current	External
IBRK	Excitation Current	External
ECBF1	Omega LCCA-3K, S/N 645288	Internal
ECBF2	Omega LCCA-3K, S/N 674849	Internal
Main Valve		
PVLV	450 psi Kulite	Valve Damping Chamber
XVLV	0-8 in Linear Potentiometer	Valve Slider
Turbine Inlet		
PT2x, (x=A,B,C)	Total Pressure	Main Frame, 120 apart
TT2x. (x=A,B,C)	Total Temperature	Main Frame, 120 apart
PP2x, (x=A,B,C)	Dynamic Pressure	Main Frame, 120 apart
PTYRn, (n=1,2,3,4,5,6)	Total Pressure, 6 head radial rake	Main Frame, fixed location
TTR101-n,(n=1,2,3,4,5,6)	Total Temperature, 6 head radial rake	Main Frame, fixed location

Table 2.5: Blowdown Turbine Instrumentation, continued

Sensor	Type	Location
Turbine Outlet		
PT45Rn,n=1,2,3,4,5,6,7,8	Total Pressure, 8 head radial rake	Downstream Translator
TTR103-n, n=1,2,3,4,5	Total Temperature, 5 head radial rake	Downstream Translator
RTD103-n, n=1,2 T/C	Reference RTD's, 2 locations	Downstream Translator
TTR104-n, n=1,2,3,4	Total Temperature, 4 head radial rake	Downstream Translator
RDT104-n, n=1,2 T/C	Reference RTD's, 2 locations	Downstream Translator
P45HUB	50 psid wall static pressure	Downstream Translator Hub
P45A	50 psid wall static pressure	Main Frame Window
Critical Flow Venturi		
PREF050	Static Pressure	Venturi Inlet
PNOZ	Static Pressure	Flow Conditioning Nozzle
TTMFM1	Total Temperature	Venturi Inlet
TTMFM2	Total Temperature	Venturi Inlet
TTNOZ1	Total Temperature	Extension Duct
TTNOZ2	Total Temperature	Extension Duct
Dump Tank		
PDMP	Static Pressure	Dump Tank
Cooling System		
PREF300	300 psi, Sensotec: STJE/1835/15 S/N: 589494	Coolant Supply Tank
PTC0	300 psi Kulite	Coolant Supply Tank
PTC1	Total Pressure, 300psig Sensotek	Coolant Supply Manifold
PTC2V	Total Pressure, 100psig Sensotek	Vane Feed Manifold
PTC2B	Total Pressure, 100psig Sensotek	Blade Feed Manifold
PCCV	Static Pressure, 100psig Sensotek	Vane Feed Entrance
PCCC	Static Pressure, 100psig Sensotek	Tip Casing Entrance
TTC0	Total Temperature	Coolant Tank Exit
TTC1	Total Temperature	Coolant Supply Manifold
TTC2B	Total Temperature	Blade Feed Manifold
TTCBV	Total Temperature	Vane Feed Entrance, B window
TTCBC	Total Temperature	Casing Feed Entrance, B window
TTCCV	Total Temperature	Vane Feed Entrance, C window
TTCCC	Total Temperature	Casing Feed Entrance, C window

Table 2.6: Blowdown Turbine Data Acquisition

Specification	Dell Omniplex 590	Dell 486D/50	IBM PII 450
System	1	2	3
Speed	High	Low	Low
Operating System	DOS	DOS	NT 4.0
DAQ Platform	In-house	In-House	LabView
DAQ Board	ADTEK AD-830	Analogic HSDAS-16	NI MIO-64E3
Resolution	12-bit	16-bit	12-bit
Board Channels	8	4x16	64
Number of Boards	4	N/A	1
Total Channels	32 simultaneous	64 multiplexed	64 multiplexed
Sampling Rate per Channel	200 kHz	2.5 kHz	5 kHz

was instrumented with a 100 psi Druck transducer. These additional measurements are required to make a transient correction that is described in Chapter 3.

2.7 Data Acquisition

The short duration nature of the blowdown experiment not only places special requirements on instrumentation, but on data acquisition (DAQ) as well. The data acquisition system monitors all instrumented channels at a sampling rate sufficient for capturing time scales of interest during the experiment. For aerodynamic performance measurements, 5 kHz is adequate. The system typically acquires data for 2-4 seconds depending on the experimental conditions being monitored. The hardware included a Pentium II 450 MHz computer which was programmed with LabVIEW lab automation software. The current DAQ system consisted of three computers. Two low-speed systems, each of which was capable of monitoring up to 64 channels, sample at 2.5 kHz and 5 kHz. The high-speed system monitored eight channel at up to 200 kHz. Table 2.6 summarizes the Blowdown Turbine DAQ equipment.

2.8 Instrument Calibration

2.8.1 Pressure Transducer Calibration

A standard calibration procedure was used to calibrate all of the differential pressure transducers. It was performed immediately after the supply tank was filled and at the conclusion of each experiment. Calibration data just before and after each experiment allows transducer drift and non-linearity to be quantified. Figure 2-10 shows a typical calibration trace of a differential pressure transducer. This figure and the calibration sequence are described below.

1. All transducers are provided a vacuum back-pressure reference by an external vacuum pump. For a post-fill calibration this produces a zero pressure differential across the transducers which are located

inside the tunnel. For those in the supply or coolant tanks, a pressure differential equal to the initial tank pressure is recorded.

2. Data is taken at this condition for approximately two minutes as shown by the first segment of the trace in Figure 2-10.

3. After two minutes, the back-pressure reference is exposed to atmospheric pressure. Data is acquired for two minutes as shown in Figure 2-10.

4. After four minutes, the back-pressure reference is returned to vacuum where it remains for the experiment.

5. This procedure is repeated after the blowdown experiment has been completed.

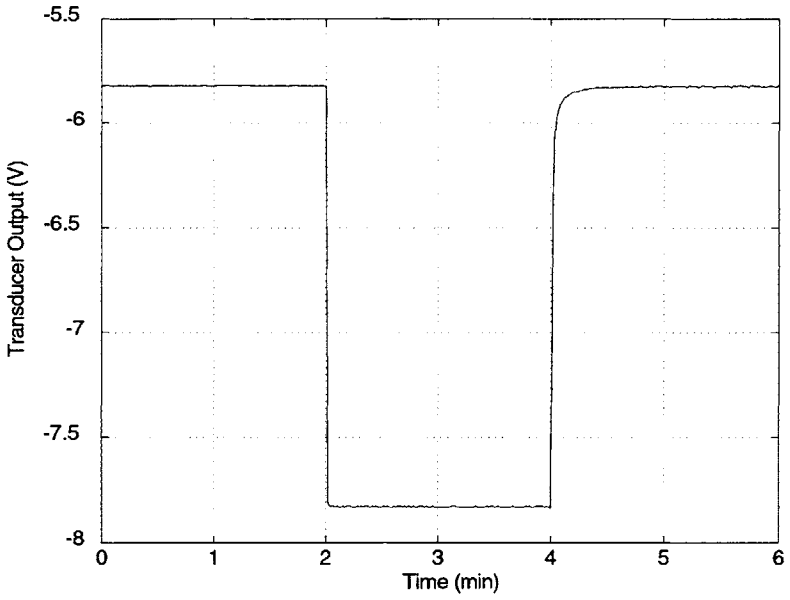

Figure 2-10: Differential Pressure Transducer Calibration

These data provide a voltage change for each differential transducer which corresponds to the local atmospheric pressure. A transducer scale factor can then be computed. Transducer zeros are taken to be the average output prior to the opening of the main valve. The scale and zero can then be used in the data reduction process via the linear calibration relation:

$$P = (Voltage - Zero)\, Scale \tag{2.1}$$

The piezoresistive strain gage pressure transducers are exposed to an extremely harsh operational environment, especially those that survey the rotor exit flow field. The pressure transducer calibration results

are monitored daily to identify any instrumentation failure. It is *extremely* important to the success of the test series to identify and replace instrumentation that has failed. A major challenge when using piezoresestive strain gages is to identify when they are about fail. Frequently, before a transducer fails its measured scale will vary significantly from run-to-run. When functioning normally the transducer scale measurement will repeat within ± 0.5% as shown for transducer PT45R3 in Figure 2-11.

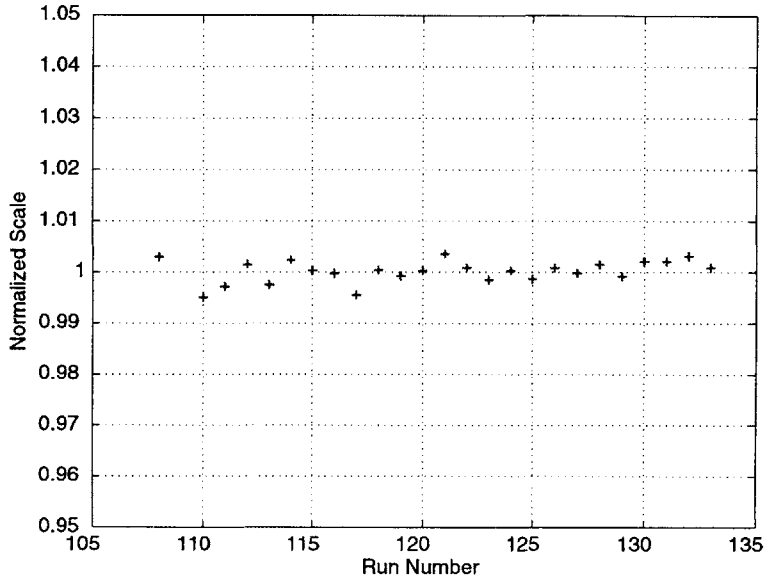

Figure 2-11: Normalized Pressure Transducer Scale - PT45R3

2.8.2 Power Measurement System Verification Tests

From run-to-run the power measurement system is calibrated by measuring the inertia of the rotor. As the rotor inertia is constant from run-to-run, its measurement can be used to verify the consistency of the torque and rotor speed measurements. The rotor inertia is estimated by spinning the rotor in vacuum up to its test speed and then braking it. The inertia is then estimated from the torque and rotor speed histories. Figure 2-12 shows the measured inertia as a function of run number. This result shows that the power measurement is very precise.

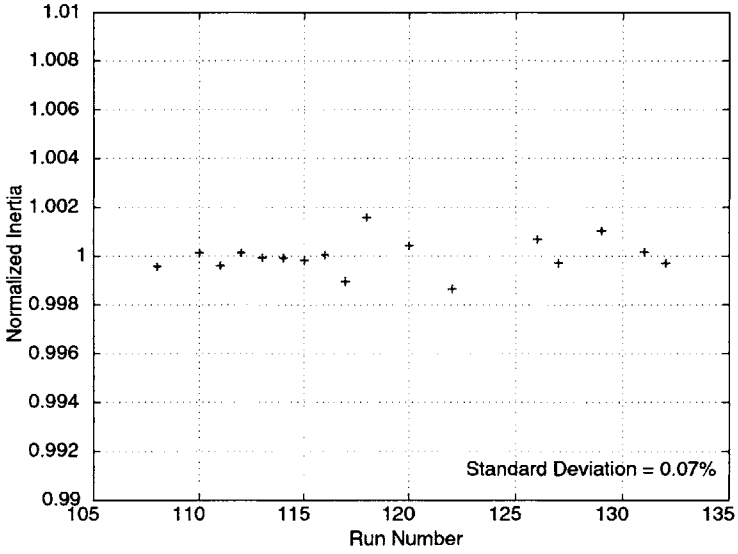

Figure 2-12: Normalized Rotor Inertia 'Run-to-Run'

2.9 Summary

This section has discussed the MIT Blowdown Turbine short duration experimental facility used to acquire turbine data for calculation of adiabatic efficiency. It has covered run-time preparations including determination of blowdown operating conditions to achieve full-scale turbine similarity. The design of new total temperature and pressure instrumentation for highly accurate flow field measurements was briefly discussed along with other instrumentation used to characterize turbine performance. This was followed by descriptions of the standard differential pressure transducer calibration procedure.

Chapter 3

Experimental Results and Data Reduction

3.1 Introduction

Recently developed techniques have enabled the measurement of turbine shaft power and mass flow in short duration blowdown type facility. These techniques have been applied to measure the isentropic efficiency of a fully scaled, film-cooled, turbine stage and a geometrically identical turbine stage without film-cooling.

The goals of this chapter are: first, to introduce the data reduction procedures used to calculate the turbine stage efficiency and corrected mass flow from the newly developed measurement techniques. Second, to provide an evaluation of these newly developed techniques, and third, to present the results of the baseline and film-cooled experiments.

Two series of tests were conducted to ascertain the influence of film-cooling on the performance of the turbine stage being studied. Firstly, the baseline [1] turbine geometry without film-cooling was parametrically tested. The turbine stage and test facility were then modified to incorporate the vane, blade, and heatshield film-cooling geometry and metering systems. The film-cooled turbine stage was then tested over the same range of operating conditions as the baseline stage, and over a range of mainstream-to-coolant mass flows and temperature ratios.

The results of these experiments show that a short duration test facility can be used to make very repeatable isentropic efficiency and mass flow measurements for both film-cooled and uncooled turbine stages. For the baseline turbine stage, the estimated uncertainty (U_{95}) for the measured efficiency is 0.40% for absolute measurements and 0.14% for back-to-back comparisons. For the film-cooled stage the estimated

[1] In this thesis the uncooled turbine stage is referred to as the baseline turbine. Since short duration test rigs are non-adiabatic, the term uncooled may be misleading. For a turbine stage without film-cooling, a short duration test simulates an internally cooled steady-state turbine.

uncertainty rose to 0.53% for absolute measurements and 0.38% for back-to-back comparisons. Comparison of the measured baseline and film-cooled turbine stage efficiencies show a reduction of 1.75% due to film-cooling at the design operating point.

3.2 Baseline Turbine Test Results

Measurements were first conducted on the baseline configuration to provide a database for the follow-on cooled tests and to assess the accuracy and repeatability of the efficiency measurement technique under more easily modeled conditions. The baseline turbine was tested using two different tip gaps over a range of operating conditions. These tests provided data on how the turbine efficiency and corrected mass flow vary with pressure ratio and corrected speed. The tests also revealed how tip clearance influences the turbine performance over a range of operating conditions.

In this chapter particular emphasis will be placed on documenting the newly developed techniques to measure the turbine stage mass flow and the shaft power in the short duration environment. Section 3.2.1 will review the data reduction procedures used to convert the measured dimensional quantities to the common nondimensional quantities used to describe a turbine performance. Section 3.2.2 will describe data reduction procedures used to build a turbine performance map to summarize the results of each test series.

Table 3.1 contains the operating point test matrix for the baseline test series. The inlet total pressure and temperature, pressure ratio, corrected speed, Reynold's number and test gas are give. The first series of runs, [024-032], tested the baseline turbine with a reduced tip gap, (1.5% of span), operating over a range of operating points [2]. Run [030] tested the turbine at a low Reynolds number. The turbine with the design tip gap (3.2% of span), was tested over a range of operating points in runs [033-038]. The influence of turbine inlet temperature (non-adiabatic effects) was studied in runs [038-040]. Run [041] tested the design tip gap at a low Reynolds number and [042] tested the same low Reynolds number using air as the test gas. An off design test point was studied in run [043], where the corrected speed was approximately 133% of the design value.

3.2.1 Baseline Test Data Reduction Procedures

Turbine Power

For a constant rotor speed the turbine power is the product of the shaft torque and speed. However, to maintain a constant rotor corrected speed throughout a blowdown test, the mechanical speed of the rotor must drop with the square root of the turbine inlet temperature. The turbine total inlet temperature drops as the test gas in the supply tank expands. Figure 3-1 shows the mechanical speed and figure 3-2 shows the brake torque for a typical blodown run. During the initial 0.3 seconds of the test the pressure ratio across

[2] Pressure ratios and corrected speeds.

Table 3.1: Baseline Turbine Test Matrix

50% Tip Gap Operating Point Test Matrix

Test	Gas	Tin, K	Pin, atm	PR	Nc, %	Re, %
abb024	CO2	350	5.4	1.93	95.6	85
abb025	CO2	351	5.4	1.94	99.8	84
abb026	CO2	350	5.4	1.94	99.5	85
abb027	CO2	351	5.4	2.05	97.8	84
abb028	CO2	350	5.4	1.92	92.3	85
abb029	CO2	350	5.4	1.96	108.9	84
abb031	CO2	350	5.4	2.13	97.5	85
abb032	CO2	349	5.4	1.78	103.9	84

50% Tip Gap - Low Reynolds Number

abb030	CO2	302	1.7	2.07	105.8	33

Design Tip Gap - Operating Point Test Matrix

abb033	CO2	351	5.4	1.78	97.4	83
abb034	CO2	350	5.4	1.95	101.2	85
abb035	CO2	351	5.4	2.07	97.7	84
abb036	CO2	351	5.4	1.94	98.2	85
abb037	CO2	351	5.4	1.97	111.6	84

Design Tip Gap - Inlet Temperature Test Matrix

abb038	CO2	331	4.9	1.94	98.8	84
abb039	CO2	342	5.2	1.95	104.4	85
abb040	CO2	351	5.4	1.96	106.5	85

Design Tip Gap - Low Reynolds Number

abb041	CO2	326	2.4	1.95	101.4	43

Design Tip Gap - Alternative Test Gas

abb042	Air	318	3.3	1.98	104.0	42

Design Tip Gap - Off Design Operating Point

abb043	CO2	352	5.4	2.1	132.6	83

the turbine stage is higher than that desired for the test. This increased pressure ratio produces additional power that accelerates the rotor by approximately 5% at the beginning of the run. This effect is taken into account when setting the initial rotor speed for each run. The shaft power, as determined from the torque and speed measurements, must be modified to account for the deceleration of rotor:

$$\mathcal{P} = \mathcal{T}\Omega + I\frac{d\Omega}{dt}\Omega \tag{3.1}$$

$\mathcal{P}$,$\mathcal{T}$ and Ω are the turbine power, torque and speed, and I is the inertia of the rotor. The deceleration of the rotor is estimated using a sliding linear fit of the measured rotor speed and the rotor inertia was estimated from the brake spin-down calibration outlined in references [11]. As shown in Figure 3-3, the deceleration of the rotor accounts for 0 to 10% of the brake power during the test window. Chapter 6 will review other minor corrections to the measured power such as disk windage and shaft bearing friction.

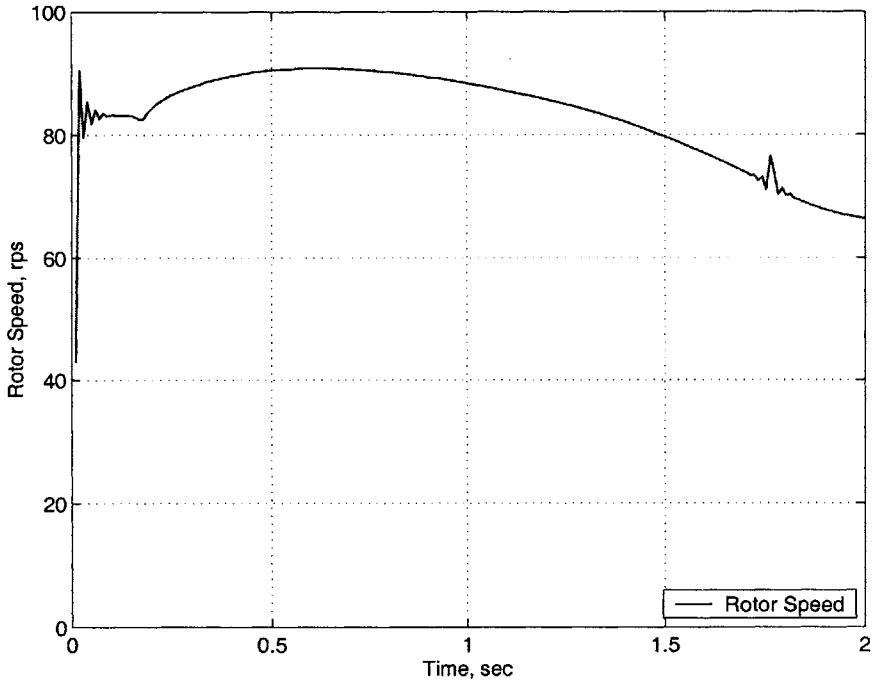

Figure 3-1: Rotor Mechanical Speed

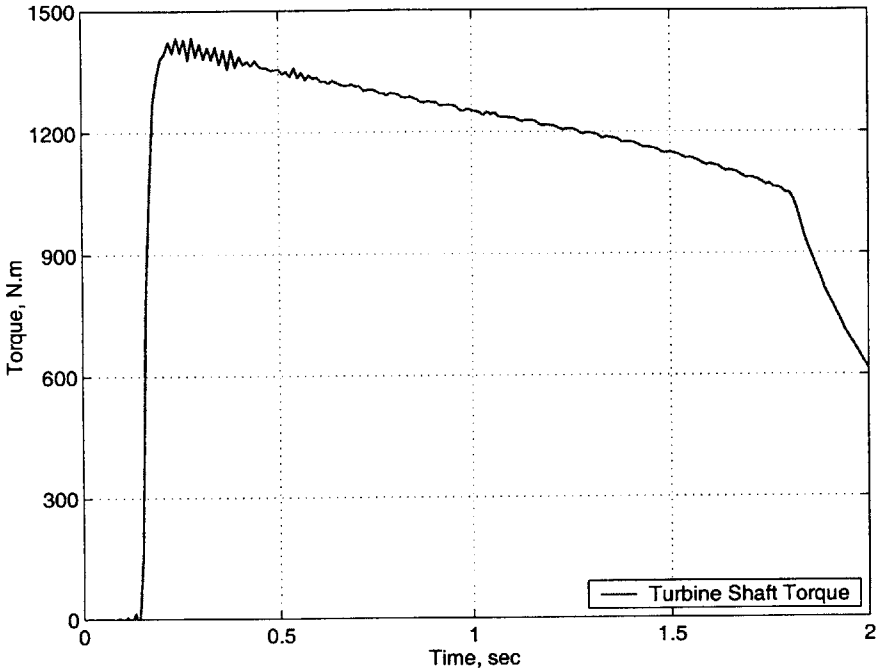

Figure 3-2: Brake Torque

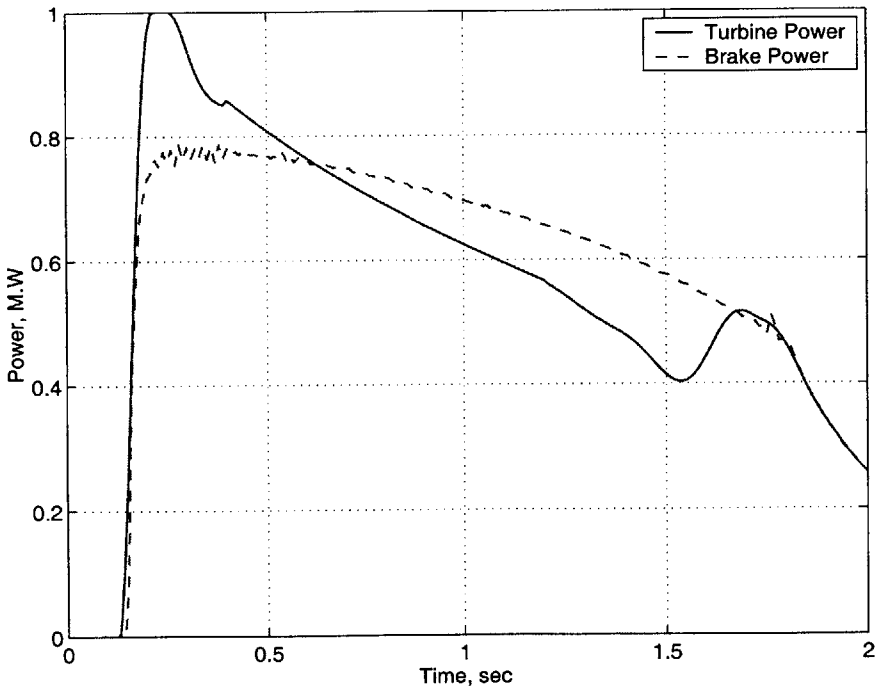

Figure 3-3: Turbine vs. Brake Power

Turbine Inlet Temperature

The turbine inlet temperature is measured at three circumferential locations at the annulus midspan. These measurements are shown in Figure 3-4. The inlet radial profile is measured at a single circumferential location using a five head total temperature rake. The inlet radial temperature profiles at test times of 0.6, 0.75, and 0.9 seconds are shown in Figure 3-5. The turbine inlet total temperature for these experiments is an area average based on these two sets of measurements:

$$T_{t\,a} = \frac{1}{3}\left(T_{t\,a1} + T_{t\,a2} + T_{t\,a3}\right)\frac{1}{A_a T_{t\,r3}}\sum_{j=1}^{5}\left(T_{t\,r_j} A_j\right) \tag{3.2}$$

$T_{t\,r3}$ is the midspan temperature of the inlet radial rake. The area averaged total inlet temperature for is shown in Figure 3-6. The steady drop in inlet temperature (from 0.3 seconds after the beginning of the test) is a result of the isentropic expansion of the test gas in the supply tank. The temperature spike at 0.2 seconds is due to a phenomenon known as compressional heating. As the valve begins to open it throttles the test gas into the annulus between the test section and the valve, which was initially in vacuum. The gas flowing into the annulus [3] compresses the gas already in the annulus and increases its total temperature. This process continues until total pressure inside the annulus is equal to the supply tank pressure. This phenomenon, also known as vessel charging, results in a mean annulus chamber temperature of γT_{ta}. The slug of hot gas is quickly convected through the facility.

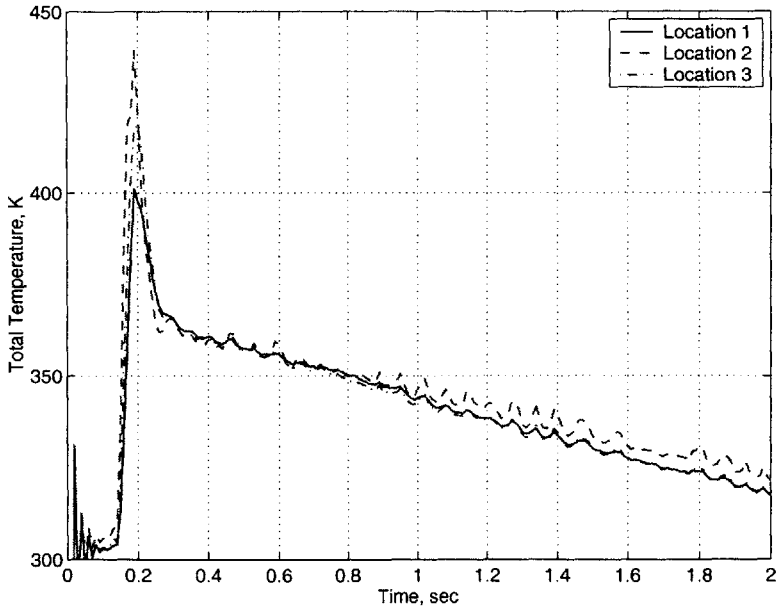

Figure 3-4: Inlet Circumferential Temperatures

[3] At the supply tank total temperature.

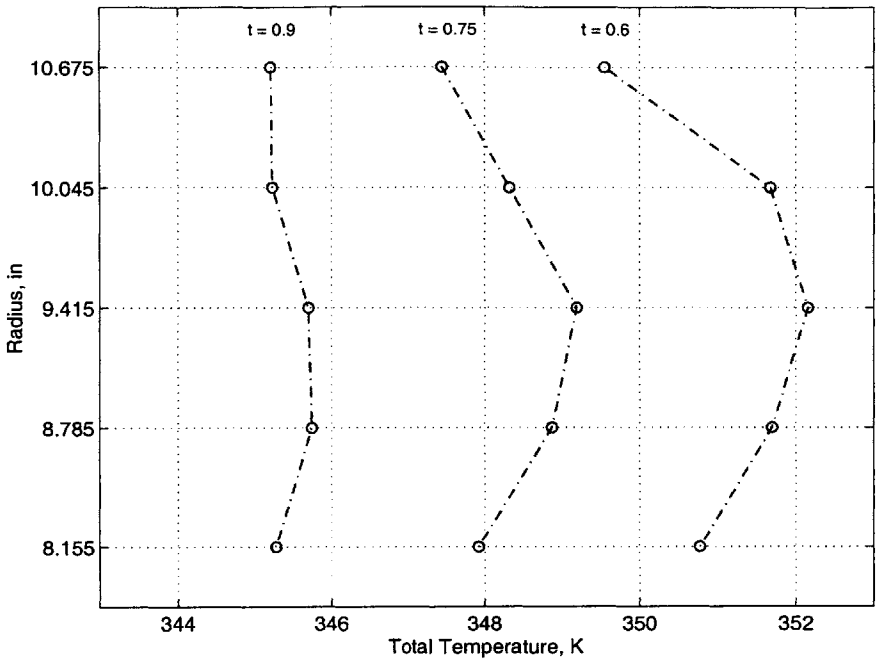

Figure 3-5: Inlet Radial Temperature Profile

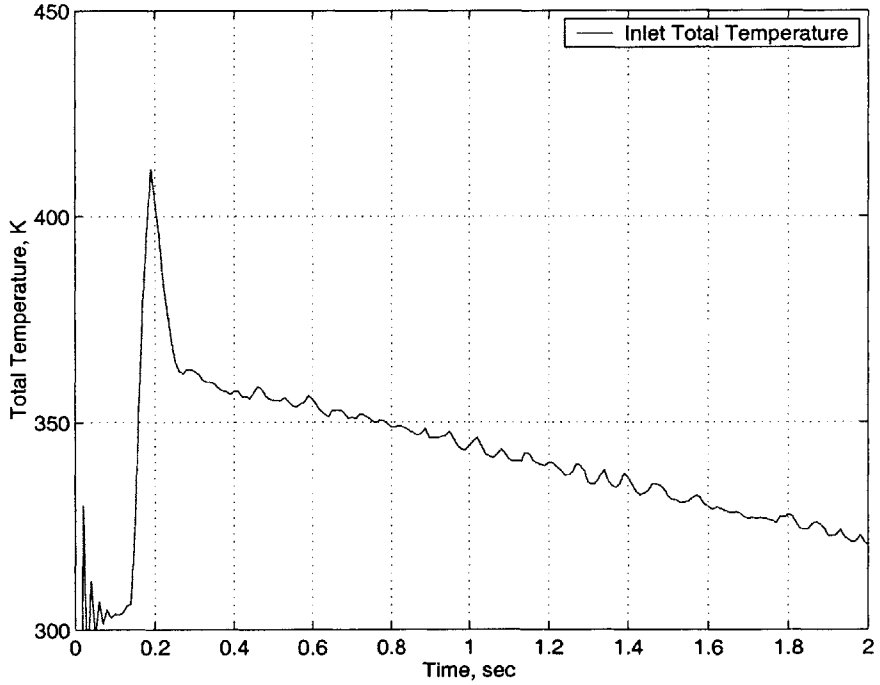

Figure 3-6: Turbine Inlet Temperature

Inlet and Outlet Total Pressures

The measured inlet and outlet total pressures are shown in Figure 3-7. The inlet total pressure was measured at three circumferential locations. The outlet total pressure is measured using an eight head radial rake that circumferentially translates the rotor exit annulus. The outlet total pressure is defined as an area average of pressures measured using this probe:

$$P_{t\,c} = \frac{1}{A_c} \sum_{j=1}^{8} \left(P_{t\,r_j} A_j \right) \tag{3.3}$$

Total pressure non-uniformities due to the nozzle guide vane wakes are visible in the downstream measurement. Jacobs [10] showed that the main frequency component of this non-uniformity matched the translator-NGV passing frequency. The low frequency disturbance caused by the NGV proved difficult to filter without changing other desired frequency components of the measurement. Instead an outlet pressure based on a third order polynomial curve fit of the data from 0.5 to 1.0 seconds was used.

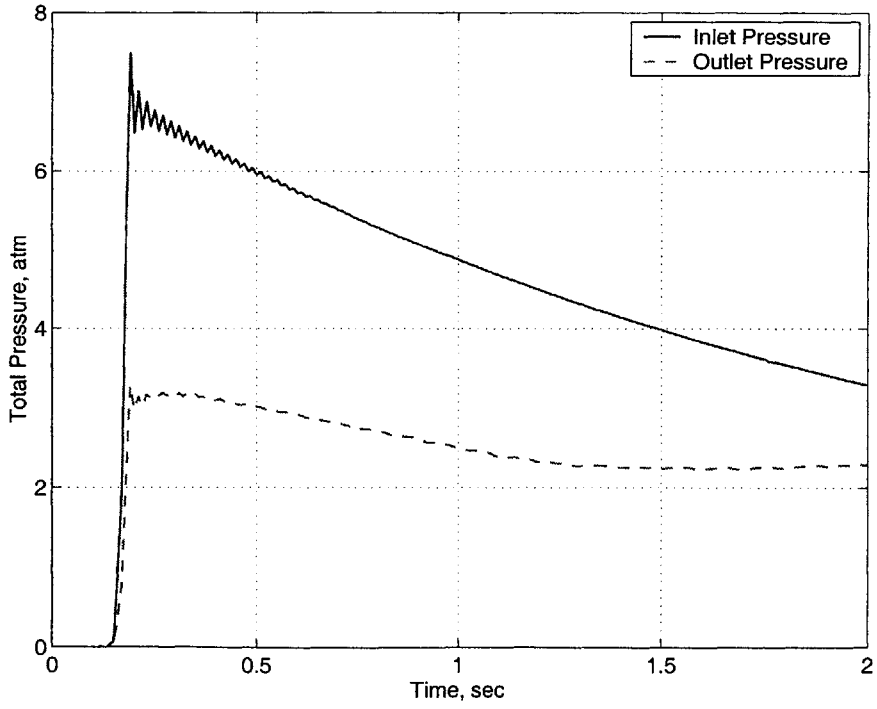

Figure 3-7: Inlet and Outlet Pressures

Turbine Mass Flow

The turbine stage mass flow was measured using a critical flow venturi nozzle (CFVN), with a correction to account for the transient pressures and temperatures in the test facility. Ideal critical flow requires three main conditions: the flow is one-dimensional, the flow is isentropic, and the gas is perfect. Under these conditions the critical mass flow rate is:

$$\dot{m} = A\,C_{*i}\,\frac{P_t}{\sqrt{RT_t}} \tag{3.4}$$

$$C_{*i} = \sqrt{\gamma\left(\frac{2}{\gamma+1}\right)^{\left(\frac{\gamma+1}{\gamma-1}\right)}} \tag{3.5}$$

However, the real gas flow rate will differ in two respects. First, the flow is not one-dimensional. Blockage due to boundary layer growth along the walls of the nozzle will reduce the mass flow. Also there is a small static pressure non-uniformity at the throat of the nozzle due to streamline curvature effects. To account for the multi-dimensional nature of the flow, A in Equation Equation (3.4) is replaced by C_dA, where C_d is the discharge coefficient of the nozzle. Second, the test gas may not be perfect and real gas thermodynamic effects must be considered. C_{*i} in Equation (3.4) is replaced by C_r, the real gas critical flow coefficient. These changes yield equation Equation (3.6):

$$\dot{m} = C_dAC_r\,\frac{P_t}{\sqrt{RT_t}} \tag{3.6}$$

The nozzle was calibrated at an independent, nationally recognized laboratory that specializes in the calibration of critical flow venturi nozzles for the natural gas and aerospace industries. The nozzle discharge coefficient is dependent on Reynolds number and is generally expressed in the form:

$$C_d = a - b\,Re_d^{-n} \tag{3.7}$$

The constants a, b, and n are obtained by calibration.

Carbon dioxide, the test gas used in this experiment, exhibits significant non- ideal gas behavior in the range of pressure and temperature under which the nozzle operates. The difference between C_i and C_r under typical test conditions for this application is 1%, which would be a significant source of error if it were not accounted for. The procedure outlined in the ANSI standard ([16]), and the NIST14 gas property database [17] were used to calculate the critical flow coefficients. The results agreed within $\pm 0.1\%$ of the

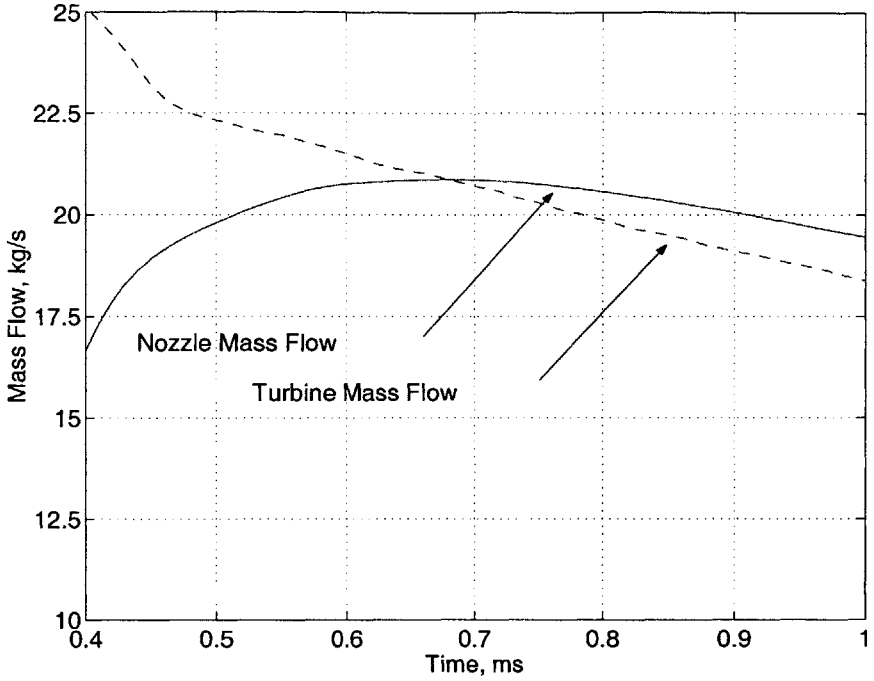

Figure 3-8: Nozzle and Turbine Mass Flow

sample values given in the ANSI standard.

Critical flow venturi nozzles are intended for steady flow application. For this application the flow is steady with respect to the time scales of the flow through the nozzle, as it is for the turbine stage itself. However, the flow is not steady with respect to the time scale of the facility. At any given time the mass flow through the nozzle may not equal that through the turbine because of the storage capacity of the compartments between the turbine exit and the CFVN. The turbine mass flow is estimated by adding a volumetric storage correction to the nozzle mass flow.

$$\dot{m}_t = \dot{m}_n + \frac{\partial M_s}{\partial t} \tag{3.8}$$

The mass stored in the compartments between the CFVN and the turbine stage is calculated from the measured temperature and pressure histories in the CFVN and the upstream duct (Figures 3-9 and 3-10). Figure 3-8 shows that the magnitude of the storage correction is small during the test window. Figures 3-9 and 3-10 show the total temperatures and static pressures between the turbine exit and the CFVN. The temperatures in the upstream duct and the CFVN asymptote to the turbine exit temperature at approximately 1 second. This transient response in these compartments is due to the first order lag as the slug of heated gas[4] is convected through the facility. Figure 3-10 shows that the static pressures in the upstream duct and the CFVN are relatively steady when compared to the other pressures in the

[4]The temperature rise of this gas is due to compressional heating.

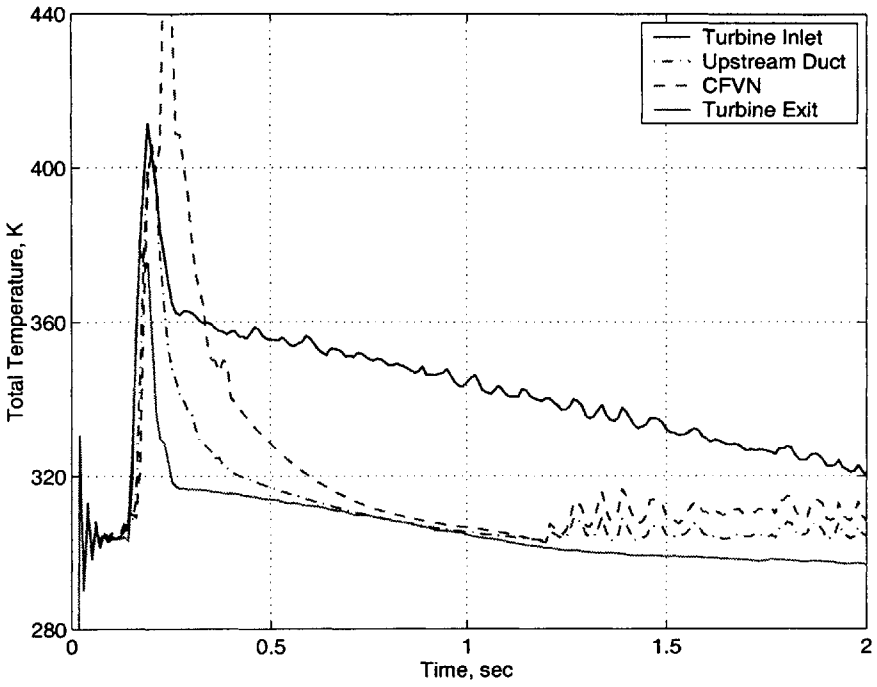

Figure 3-9: Downstream Temperatures

facility. The CFVN was designed to take advantage of the plateau in the pressures of these compartments, as this helps minimize the magnitude of correction required to determine the turbine mass flow. A one dimensional lumped parameter network model of the facility compartments was used assess the magnitude of the transient correction and the impact of the CFVN on the turbine pressure ratio. Between 0.6 and 0.7 seconds the transient correction goes through zero, and over the range of 0.5 to 1.0 seconds it varies by $\pm 5\%$ of the venturi mass flow.

Two methods were conceived to verify the magnitude of the correction. Grepin [7] installed three transient pitot probes upstream of the turbine stage, from which the NGV inlet Mach number was determined. If the effective area at the measuring plane is known then the turbine mass flow can be estimated. The effective area was calibrated against the critical flow venturi over the window where the correction is within $\pm 5\%$. The pitot probe measurements were then used to verify the volumetric storage correction over the test window of 0.6 to 0.9 seconds.

The second approach uses the blowdown Equation (Equation (3.9)) for the supply tank to estimate the turbine mass flow. Guenette [8] showed that in an isentropic blowdown-type facility, the mass flow is a unique function of supply tank stagnation pressure:

$$\begin{aligned} \dot{m}(t) &= -V\frac{d\rho}{dt} \\ &= \left(\frac{2}{\gamma-1}\right)\left(\frac{V}{\tau}\right)\frac{P_{t\,a}(t)}{RT_{t\,a}(t)}\left[1-\frac{t}{\tau}\right]^{-\frac{\gamma+1}{\gamma-1}} \end{aligned} \tag{3.9}$$

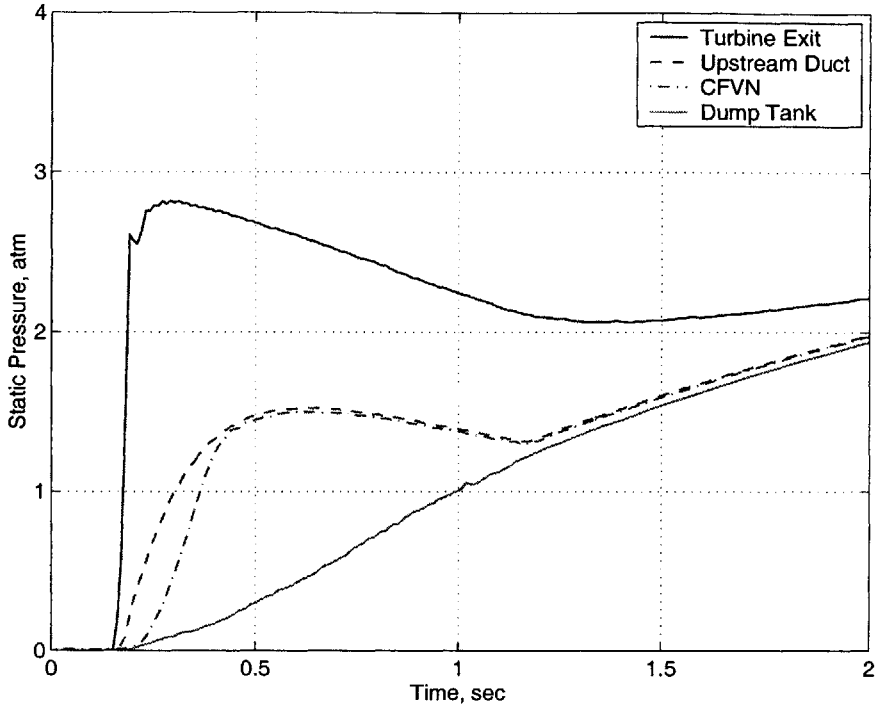

Figure 3-10: Downstream Pressures

The blowdown time constant, τ was estimated using a least squares fit to the pressure history of the supply tank. As shown by Equation (3.9), if the supply tank volume (and bleed fraction) and τ are known, the turbine mass flow can be determined. The volume was calibrated against the critical flow venturi over the test window where the transient correction is $\pm 5\%$. Sample results for this method are shown in Figure 3-11. Both of these methods verify the characteristic shape of the turbine mass flow over the test duration as estimated by Equation (3.8).

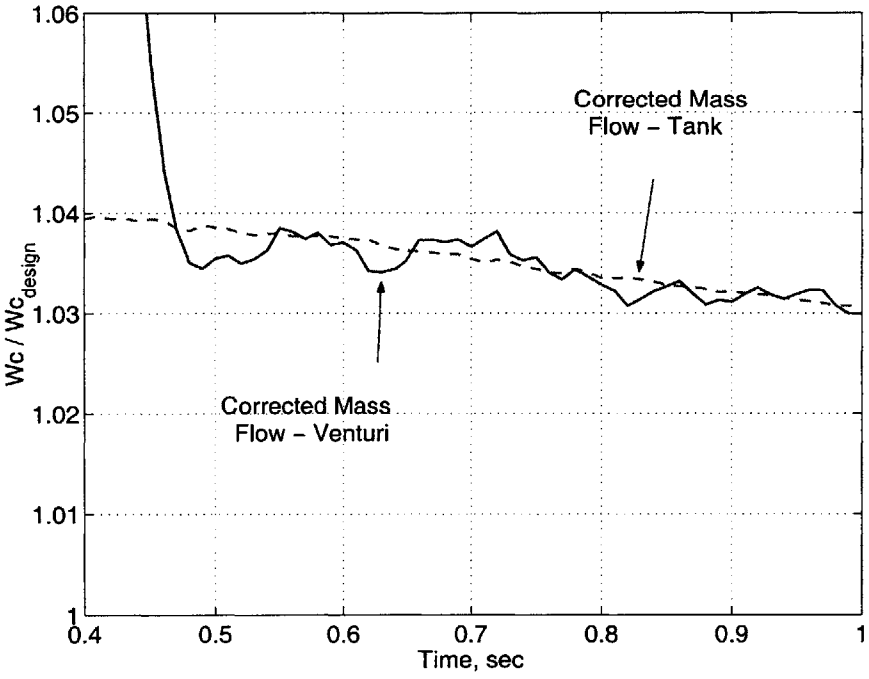

Figure 3-11: Corrected Mass Flow from Supply Tank fit to Nozzle Corrected Flow

Turbine Ideal Work

The ideal turbine power equals the ideal total enthalpy drop across the turbine. For a calorically perfect gas, the ideal enthalpy drop is the product of the mass flow, specific heat capacity and the isentropic temperature drop across the turbine:

$$P_{Ideal} = \dot{m} c_p T_{t\,a} \left(1 - \pi^{\frac{\gamma-1}{\gamma}}\right) \tag{3.10}$$

However, carbon dioxide exhibits significant non-ideal gas behavior for the range of pressures and temperatures of the experiment and Equation (3.10) would under predict the efficiency by several percent (Jacobs [10]). The ideal enthalpy drop instead is calculated from the upstream temperature and pressure and the downstream pressure using Equation (3.11):

$$P_{Ideal} = \dot{m} \left(h\left(T_{t\,a}, P_{t\,a}\right) - h\left(T_{t\,c_{is}}, P_{t\,c}\right)\right) \tag{3.11}$$

The upstream enthalpy is evaluated from the NIST14 [17] gas tables, as a function of pressure and temperature. The ideal downstream enthalpy can be determined from the measured pressure and adjusting the downstream temperature until the downstream entropy matches the inlet entropy.

Turbine Stage Non-Dimensional Parameters

The stage non-dimensional parameters are shown in Figures 3-12 to 3-15. For the test window of 0.6 to 0.9 seconds the pressure ratio was held constant to ± 1% for each run and the corrected speed was held constant to ± 2%. These two measurements are the independent parameters that are used to define the test operating point. The independent parameters; corrected mass flow and reduced power are shown in figures 3-14 and 3-15. The dimensional real and ideal power are shown in Figure 3-16. These figures show that the variation of the non-dimensional parameters is small compared to the variation of the dimensional quantaties. The corrected speed, mass flow and power are defined as follows:

$$N_c = \frac{\Omega L_{ref}}{\sqrt{\gamma R T_{t\,a}}} \tag{3.12}$$

$$W_c = \frac{\dot{m}_c \sqrt{R T_{t\,a}}}{P_{t\,a} L_{ref}^2} \tag{3.13}$$

$$\mathcal{P}_c = \frac{\mathcal{P}}{\sqrt{P_{t\,a} L_{ref}^2 \gamma R T_{t\,a}}} \tag{3.14}$$

Figures 3-13 to 3-15 show the nondimensional parameters normalized by their design point values. As the through flow time[5] for the turbine is $\approx$ 5 milliseconds, there is approximately two orders of magnitude more test time than is required for steady operation of the turbine. This test facility was originally designed with a long test time to enable the exit flow field of the turbine to be surveyed. The 0.5 seconds of test time is adequate for this purpose.

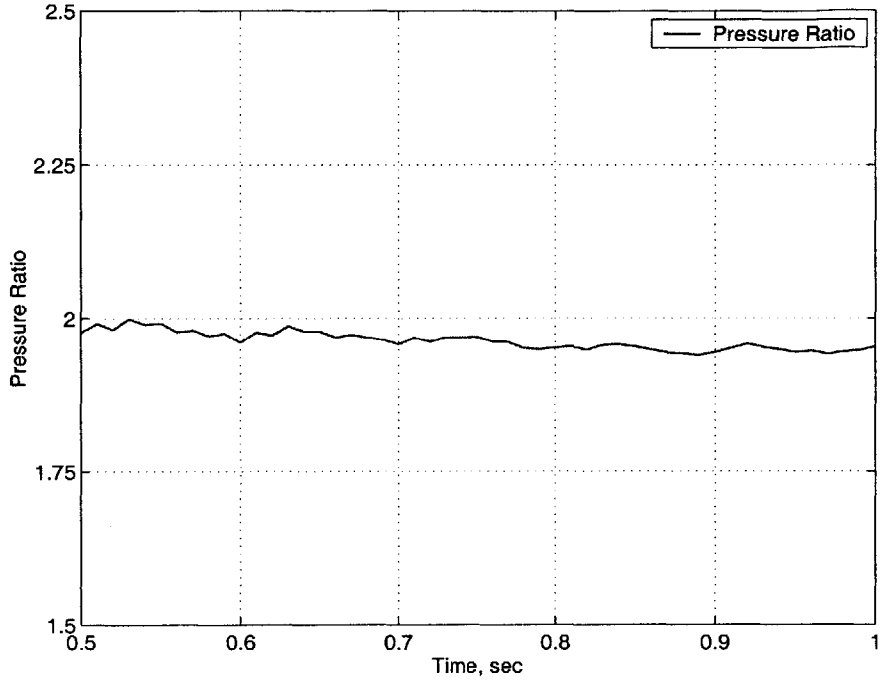

Figure 3-12: Turbine Total-to-Total Pressure Ratio

Turbine Efficiency

Figure 3-16 shows the ideal and measured turbine power, both drop by 15 % over the test window because of the changing upstream conditions. The turbine efficiency is defined as the ratio of the actual to ideal turbine power:

$$\eta = \frac{\mathcal{P}}{\mathcal{P}_{Ideal}} \tag{3.15}$$

The turbine shaft power $\mathcal{P}$ is defined by Equation 3.1 and $\mathcal{P}_{Ideal}$ is defined by Equation 3.11. The calculated isentropic efficiency is shown in Figure 3-17. For this run the efficiency changes by $\pm$ 0.2 % over the test window. The small changes in efficiency can generally be correlated to the changes in pressure ratio and corrected speed over the test window. This can be shown by developing an overall performance map of the turbine.

[5]The time required for a fluid particle to pass from the inlet to the exit measurement plane.

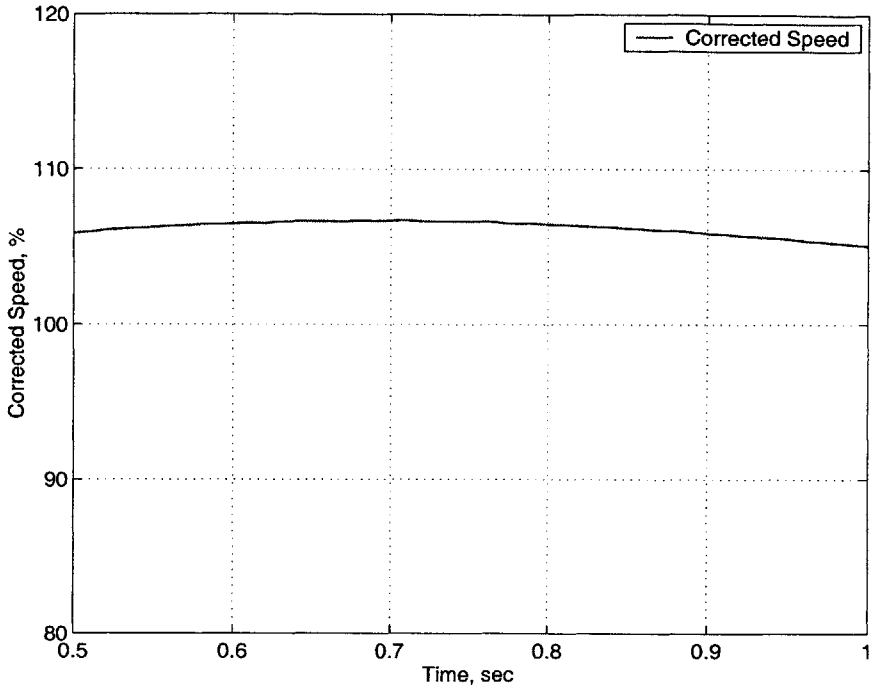

Figure 3-13: Turbine Corrected Speed

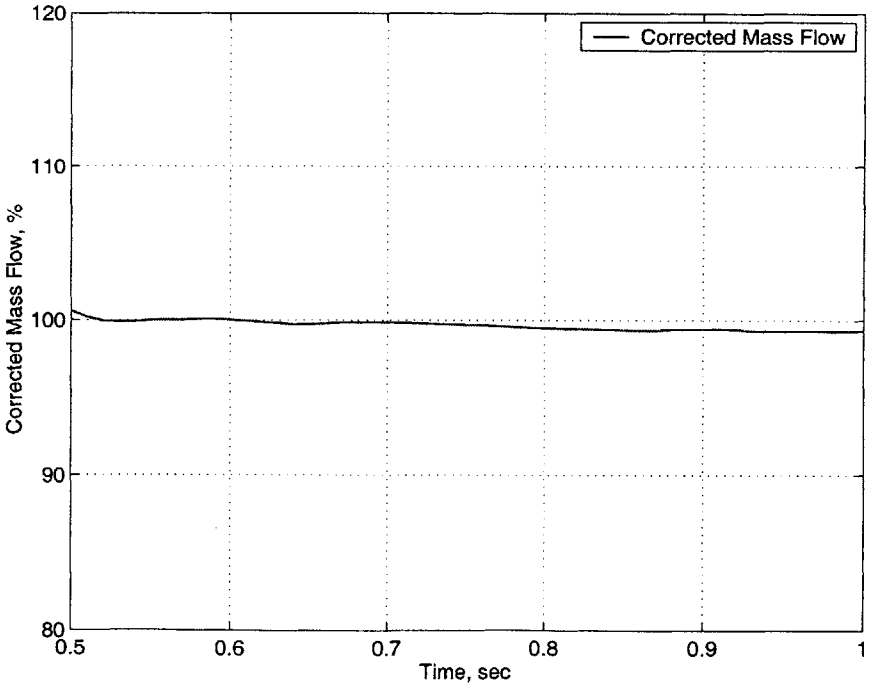

Figure 3-14: Turbine Corrected Mass Flow

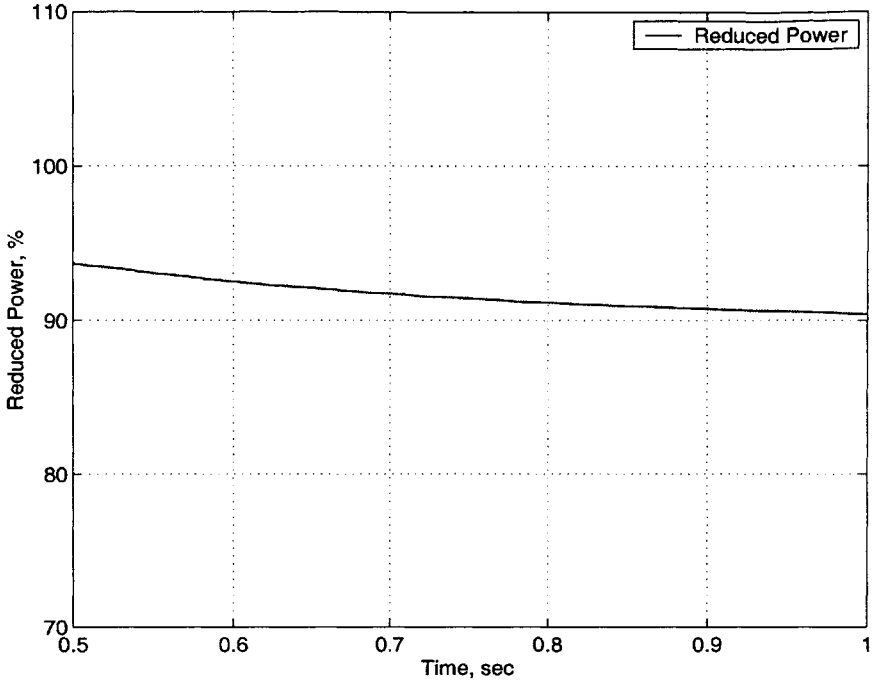

Figure 3-15: Turbine Reduced Power

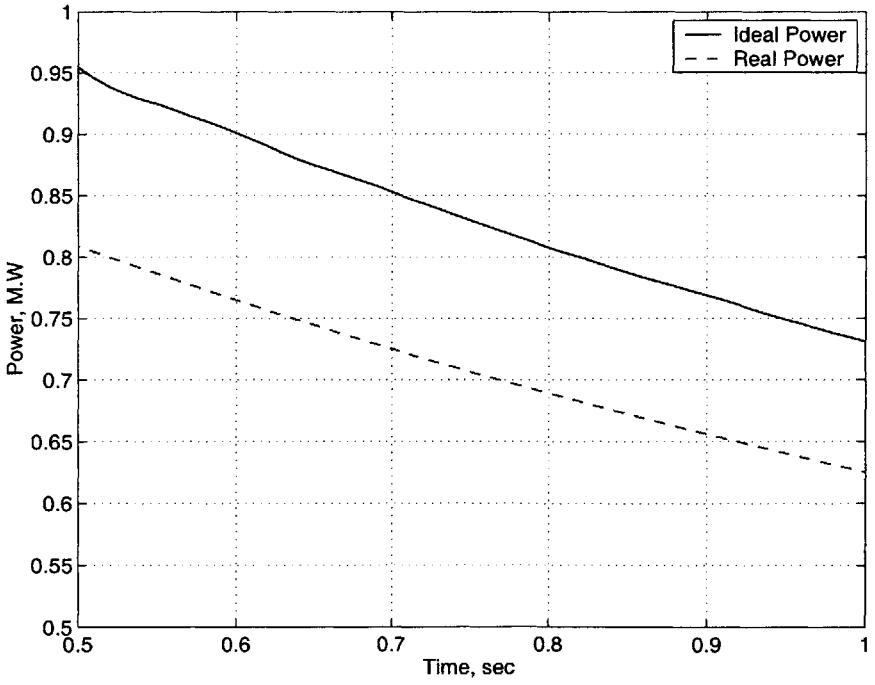

Figure 3-16: Turbine Ideal and Measured Power

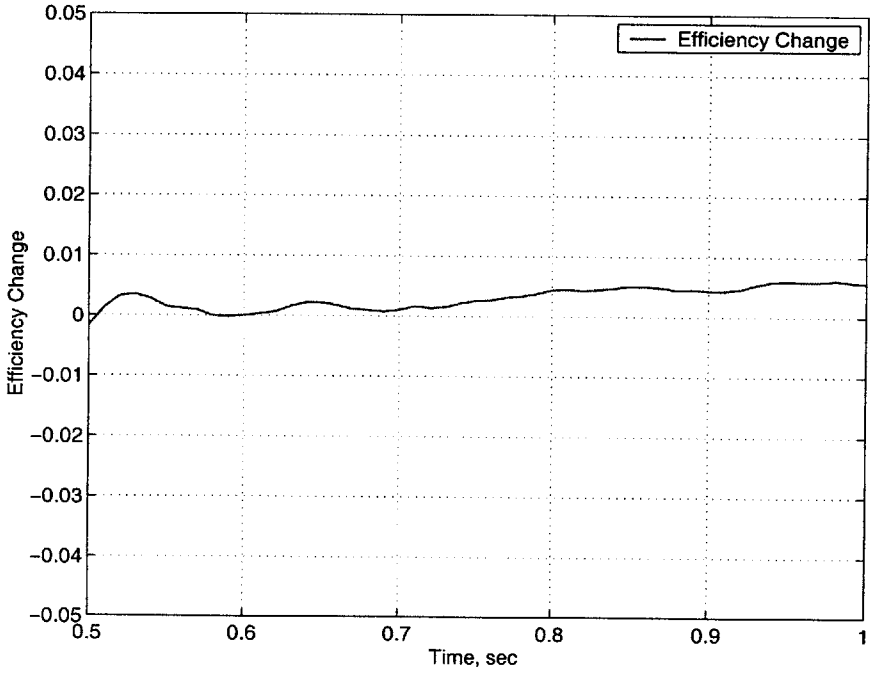

Figure 3-17: Isentropic Efficiency

3.2.2 Turbine Performance Map

Figures 3-18 and 3-19 shows the ranges of pressure ratio and corrected speed over which the baseline turbine was tested. A quadratic least squares fit (applied to the measured isentropic efficiency from all of the runs) was used to estimate the sensitivity to changes in pressure ratio and corrected speed:

$$\begin{aligned}\eta\left(\delta\pi, \delta N_c\right) = A_1 + B_1\left(\delta\pi\right) \\ +C_1\left(\delta N_c\right) + B_2\left(\delta\pi\right)^2 + C_2\left(\delta N_c\right)^2\end{aligned} \tag{3.16}$$

Figures 3-20 and 3-21 show the results of the two dimensional quadratic curve fit of efficiency for the two tip gap configurations. Figure 3-22 shows the isentropic efficiency as a function of pressure ratio and Figure 3-23 shows the efficiency as a function of corrected speed. In order to simplify the presentation of the data, the points shown in figure 3-22 are the measured data as a function of pressure ratio corrected to the design corrected speed. Similarly, Figure 3-23 are the measured data as a function of corrected speed with corrections made for the changes in pressure ratio over each run.

At the design operating point the stage efficiency increased by 2.5%, after reducing the rotor tip gap by 50%. Assuming a linear relationship between the tip gap and the reduction in efficiency, the measured sensitivity to tip gap is a 1.7% drop in efficiency per percent of tip gap. The measured sensitivity varies with operating point. As shown in Figure 3-23 the sensitivity is higher at high corrected speeds. This result is not consistent with many tip gap correlations (Horlock [9]), most of which predict that the tip gap loss increases with higher loading (reduced speed). Figure 3-22 shows that the change in sensitivity to tip gap versus pressure ratio is small when compared to that of the corrected speed. It should also be noted that the design tip gap was tested over a limited range of pressure ratios. The trends predicted the curve fit should not be used to extrapolate beyond the range that was actually measured.

Figures 3-24 to 3-27 show the measured trends for the variation of corrected mass flow with pressure ratio and corrected speed. The corrected mass flow is reduced as the pressure ratio is reduced and also as the corrected speed is increased. The corrected mass flow is normalized by its design point value. These trends are consistent with a mean line velocity triangle model of the stage, as will be shown in Chapter 5. Similar trends were measured for both tip gaps.

The post-test uncertainty estimate for back-to-back measurements based on the standard deviation of the quadratic curve fits for two tip gaps is 0.14%. The estimated absolute uncertainty, which includes bias estimates, is 0.40%. The uncertainty analysis for the baseline and film-cooled tests is presented in Appendix A.

Table 3.2: Baseline Turbine Performance Map

Parameter	Test Condition	A_1	B_1	B_2	C_1	C_2
η	50 % Tip Gap	0.0254	7.844e-003	-3.957e-002	9.644e-004	-1.342e- 005
W_c	50 % Tip Gap	104.47e	3.497e+000	-1.748e+001	-1.631e-002	- 1.230e-003
η	Design Tip Gap	0.0	-1.538e-002	-1.924e-001	4.903e-004	- 1.645e-005
W_c	Design Tip Gap	100.0	3.139e+000	-1.569e+001	-2.659e-002	-1.887e- 003

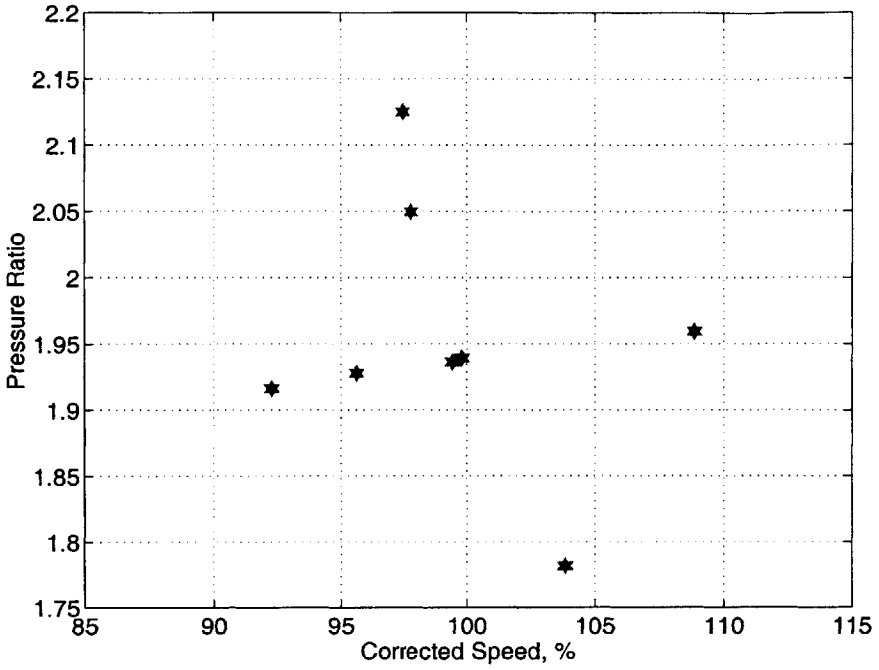

Figure 3-18: Baseline Operating Points - 50% Tip Gap

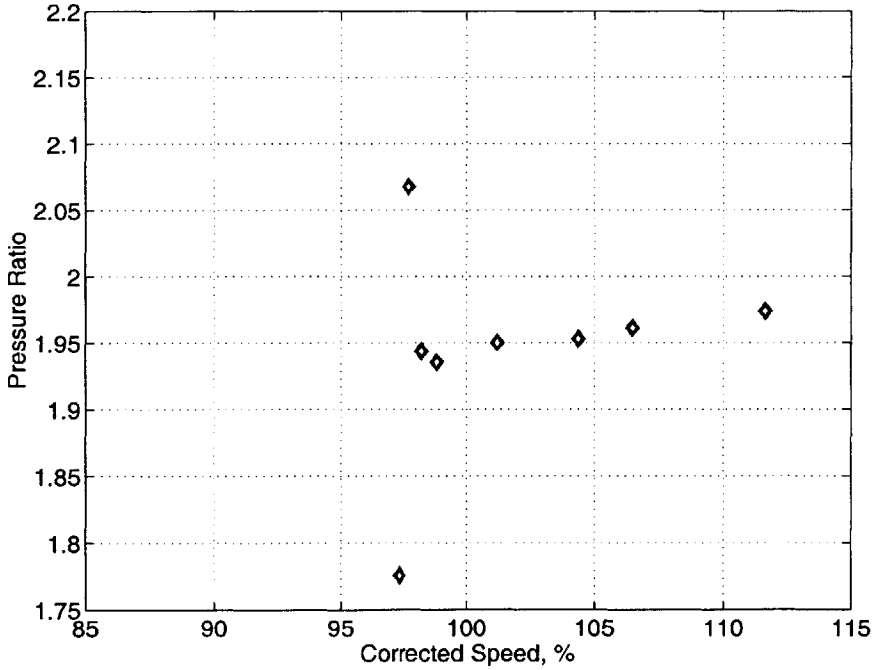

Figure 3-19: Baseline Operating Points - Design Tip Gap

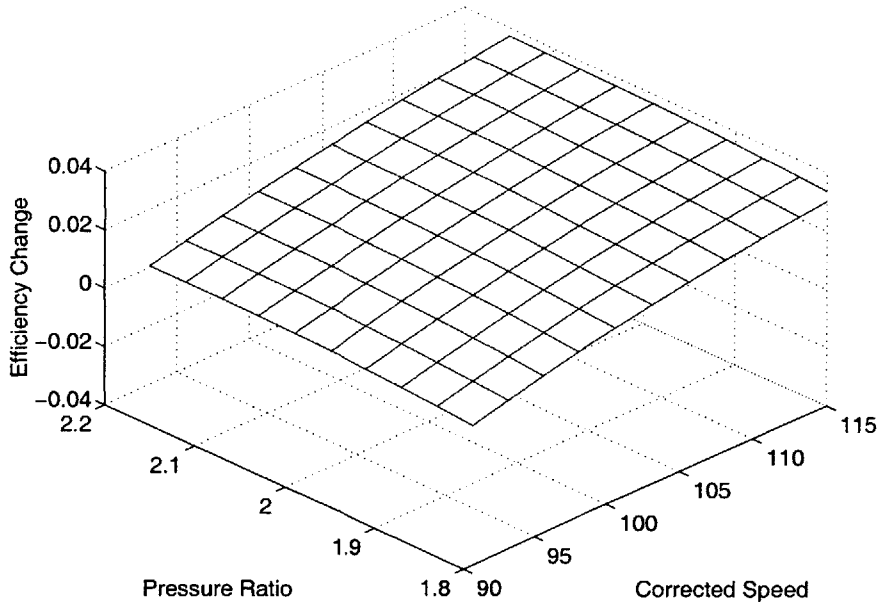

Figure 3-20: Isentropic Efficiency Curve Fit - 50% Tip Gap

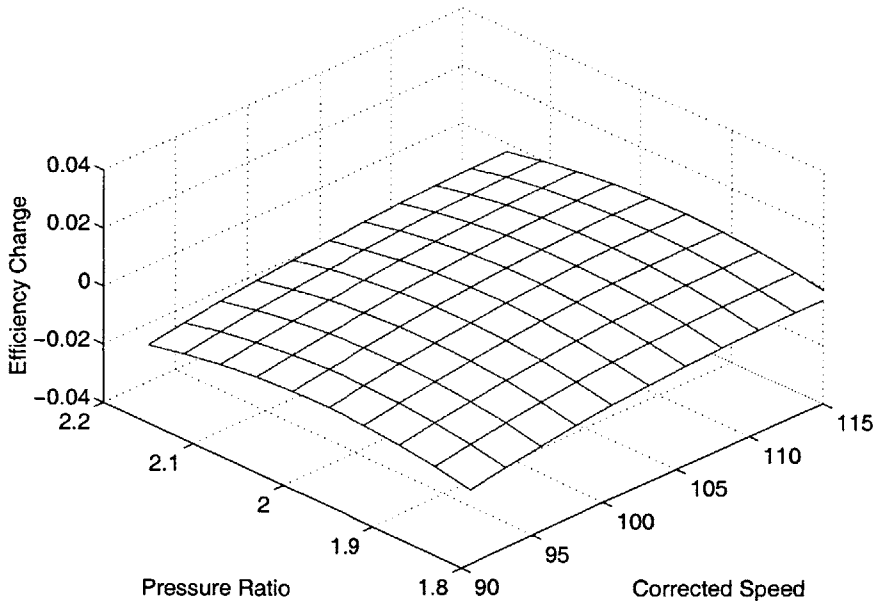

Figure 3-21: Isentropic Efficiency Curve Fit - Design Tip Gap

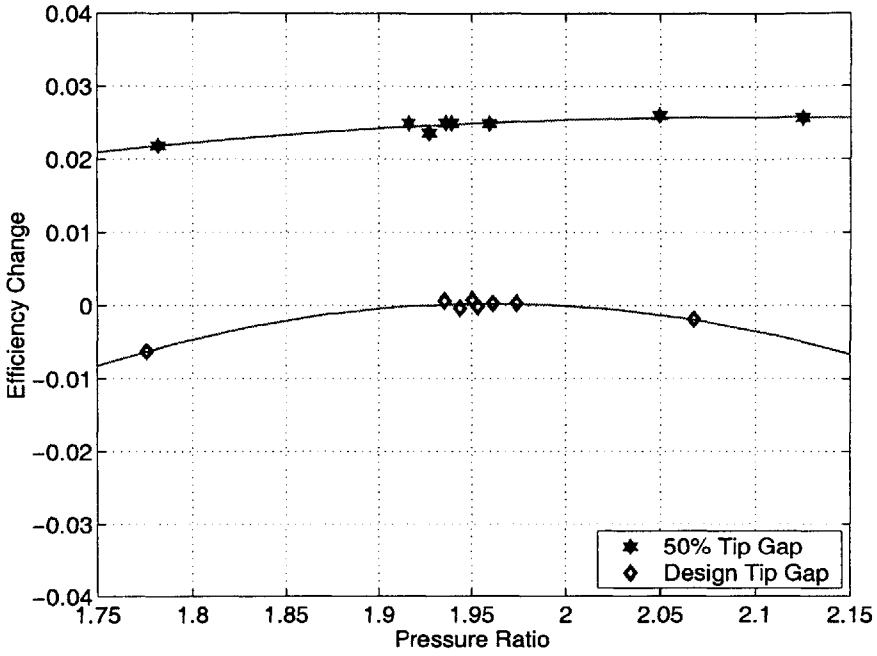

Figure 3-22: Isentropic Efficiency vs. Pressure Ratio

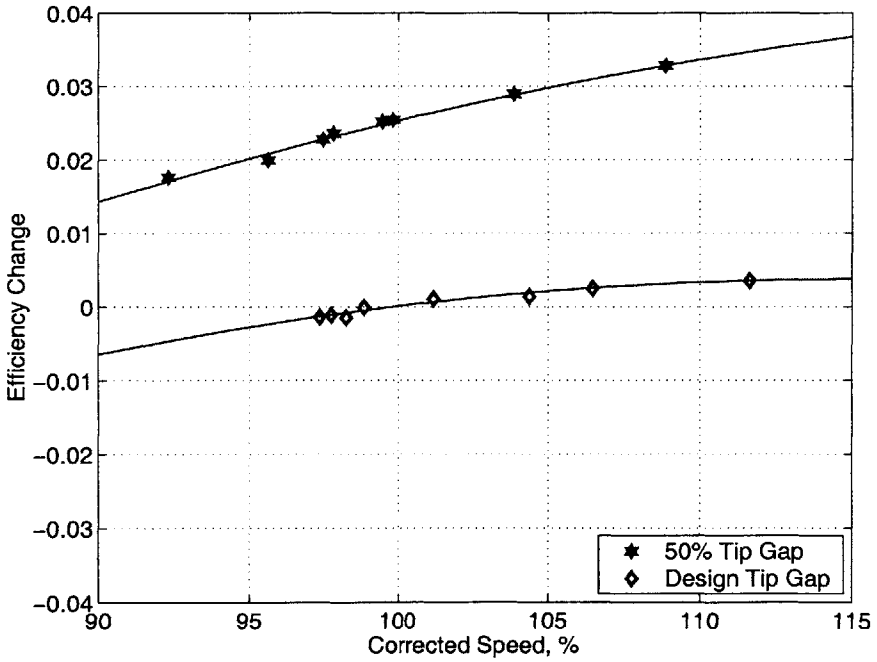

Figure 3-23: Isentropic Efficiency vs. Corrected Speed

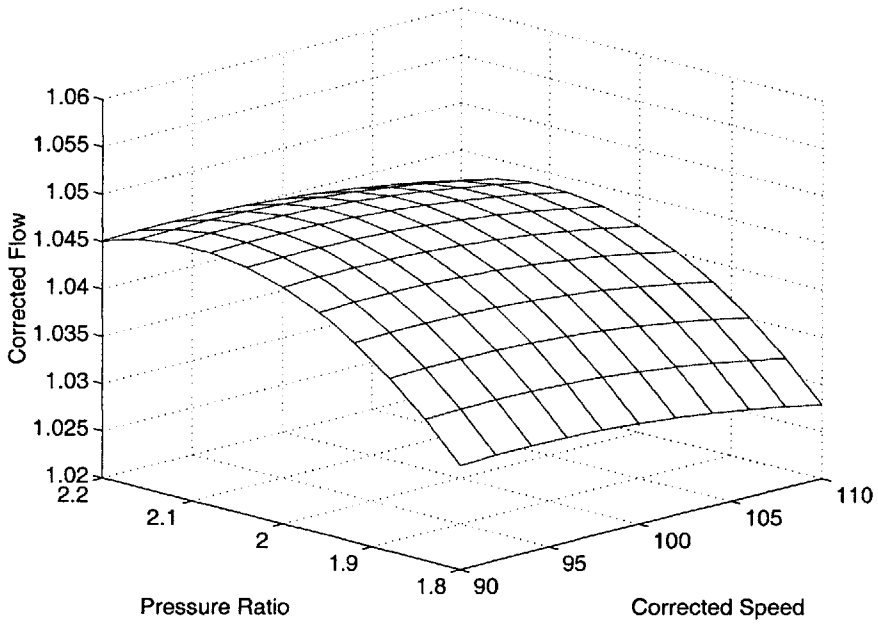

Figure 3-24: Corrected Mass Flow Curve Fit 50% Tip Gap

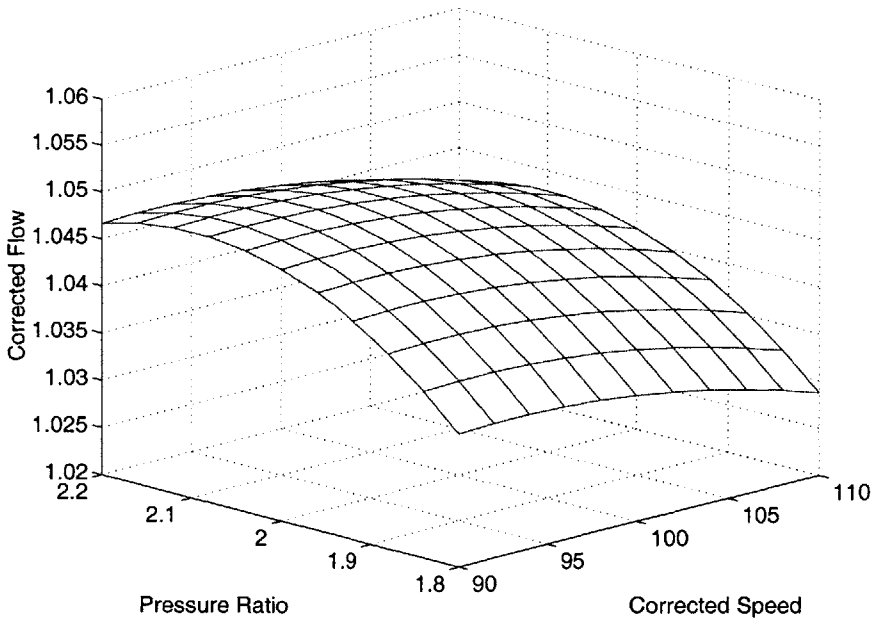

Figure 3-25: Corrected Mass Flow Curve Fit Design Tip Gap

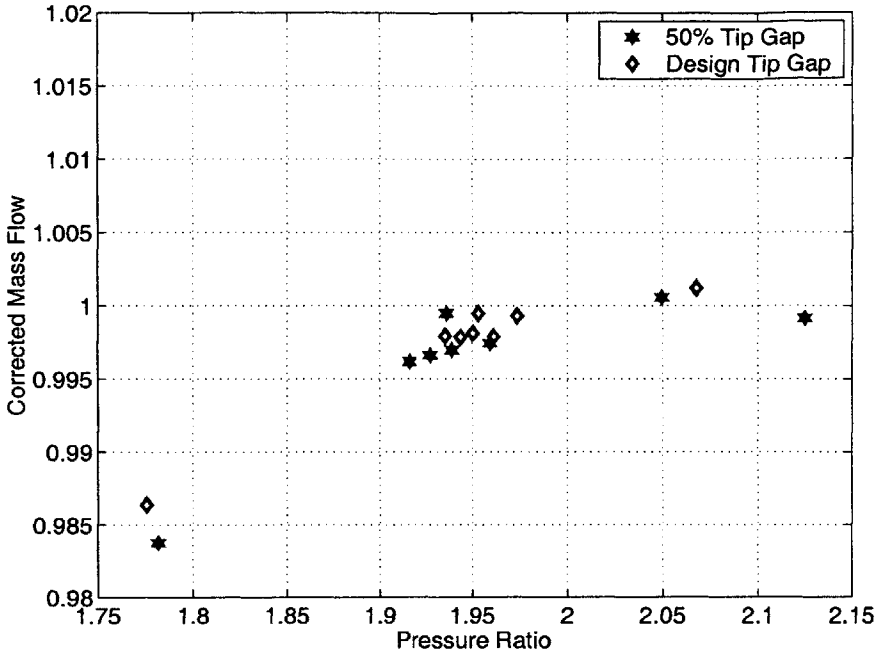

Figure 3-26: Corrected Mass Flow vs. Pressure Ratio

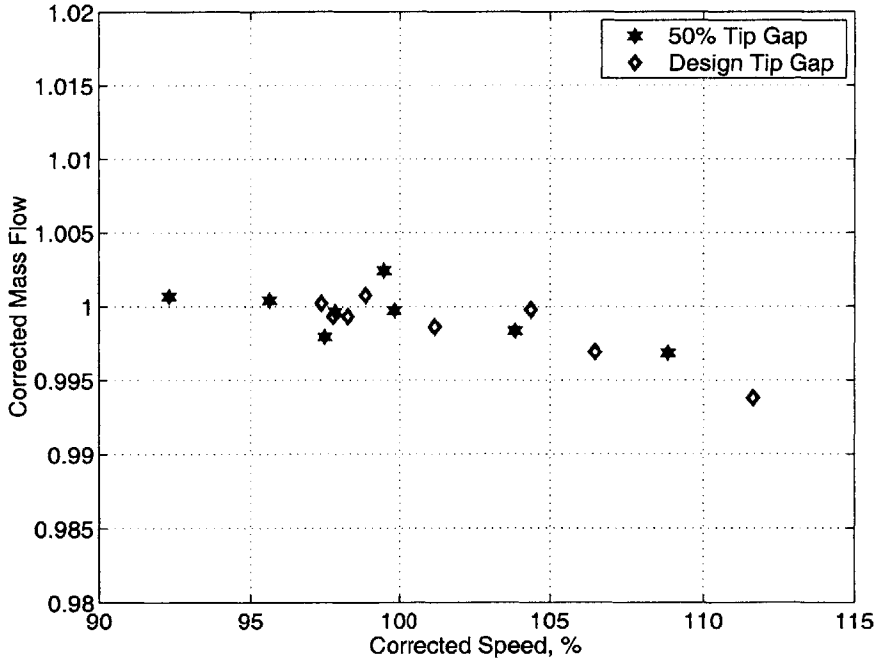

Figure 3-27: Corrected Mass Flow vs. Corrected Speed

3.2.3 Turbine Inlet Temperature

The baseline turbine was tested at two reduced temperatures to examine the degree to which non-adiabatic effects influenced the turbine efficiency. For these two tests the inlet Reynolds number was matched by reducing the supply tank pressure, as shown in Table 3.1. The results of these tests are compared with the results from the operating point test matrix in Figure 3-28. Figure 3-28 shows that the inlet temperature was varied by 20 degrees Kelvin for these tests. As the metal temperature is held at approximately 300K, the variation in inlet temperature corresponds to change of 40% in the NGV heat load. An analysis by Denton [4], based on the first and second laws of thermodynamics, indicated that the turbine efficiency should have increased by approximately $\approx 0.1\%$ for this reduction in heat load. This thermodynamic benefit may be offset by increased boundary layer losses as the heat load is reduced. As can be seen from the data, no influence of inlet temperature (non-adiabatic effects) was observed.

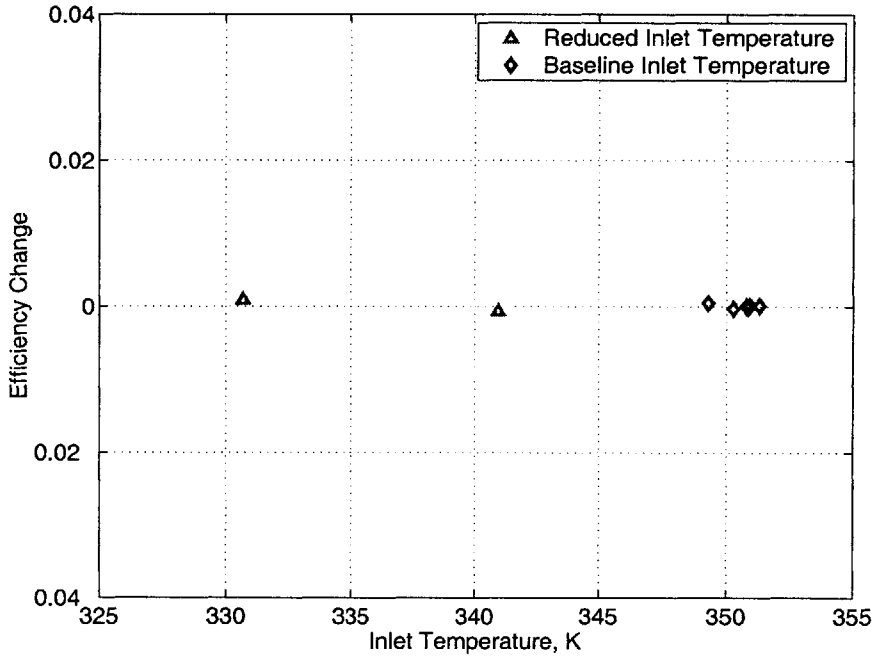

Figure 3-28: Isentropic Efficiency vs. Turbine Inlet Temperature

3.3 Film-Cooled Test Results

The film-cooled turbine was tested at the design tip gap over a range of pressure ratios and corrected speeds, at the design coolant mass flow and gas-to-metal temperature ratio. These tests examine the degree to which the influence of film-cooling is affected by changes in turbine pressure ratio and corrected speed. The turbine was then tested at its design point pressure ratio and corrected speed, with a range of coolant mass flows. The turbine was also tested at a low gas-to-metal temperature ratio over a range of mass flows to determine if the turbine losses scaled with coolant to mainstream momentum flux ratio as has been observed in cascade tests. Table 3.3 summarizes the experimental conditions for the film-cooled turbine test series. The cooled turbine was tested at a higher inlet temperature to match the gas-to-metal temperature of the engine. Runs [118-126,128,130,131] tested the cooled turbine over a range of operating points. The design point operating conditions were repeated in order to establish the repeatability of the measurements. Runs [127,129] tested the cooled turbine over a range of inlet temperatures to help characterize the non-adiabatic effects for the film-cooled turbine. Runs [114-116,132-133] tested the cooled turbine at the design gas-to-metal temperature ratio over a range coolant mass flows. A range of coolant mass flows was tested in runs [110,111,113,117] at a lower turbine inlet temperature. A high Reynolds number case was tested in run [112] at the same low inlet temperature.

3.3.1 Film-Cooled Data and Data Reduction

Chapter 2 outlined the calibration process for reducing the measured instrument voltages to engineering units. This section provides a sample of the measured data (in engineering units) used to make film-cooled turbine efficiency measurements. The data reduction procedure for the coolant mass flow and the ideal turbine work for the film-cooled turbine is outlined. The reduction procedures for the actual turbine work, inlet temperature, overall mass flow, and inlet and outlet pressures are the same as those described for the baseline configuration.

Coolant Mass Flow

The coolant mass flow is metered using thick square edged orifices. The vane and blade coolant feeds each have a single orifice. Three orifices were used for the heatshield coolant feed system in order to minimize the volume downstream of the orifices. This is required to reduce the time constant, or lag associated with the downstream volume. The coolant mass flow is calculated in a similar manner as described for the critical flow venturi nozzle:

$$\dot{m}_i = C_d A_i C_r \frac{P_{ti}}{\sqrt{R T_{ti}}} + V_i \frac{\partial \rho_i}{\partial t} \tag{3.17}$$

Table 3.3: Film-Cooled Turbine Test Matrix

Low Inlet Temperature - Coolant Mass Flow

Test	Gas	Tin, K	Pin, atm	PR	Nc, %	Re, %	Mcool, %	Tin/Tvane
abb110	CO2	329	3.6	2.07	106.3	63	4.8	1.11
abb111	CO2	329	3.6	2.04	106.2	64	8.4	1.12
abb113	CO2	330	3.6	2.02	106.0	64	10.0	1.13
abb117	CO2	331	3.6	2.01	105.8	64	11.7	1.16

Low Inlet Temperature - High Reynolds Number

abb112	CO2	331	5.4	2.04	109.6	95	6.6	1.13

High Inlet Temperature - Operating Point

abb118	CO2	441	5.2	2.03	102.7	63	9.9	1.58
abb119	CO2	439	5.3	2.03	104.5	63	9.2	1.52
abb120	CO2	446	5.3	2.01	96.1	62	9.7	1.58
abb121	CO2	445	5.3	1.98	90.3	63	9.7	1.57
abb122	CO2	448	5.3	1.81	94.2	61	9.8	1.58
abb123	CO2	447	5.3	2.12	96.1	62	9.6	1.58
abb124	CO2	445	5.3	2.01	93.6	63	9.9	1.60
abb125	CO2	444	5.3	2.01	97.6	63	10.0	1.60
abb126	CO2	445	5.2	2.01	97.0	62	9.9	1.60
abb128	CO2	442	5.3	2.04	112.3	63	9.9	1.58
abb130	CO2	439	5.3	2.02	99.8	63	9.8	1.56
abb131	CO2	442	5.3	2.06	99.7	63	9.9	1.58

High Inlet Temperature - Inlet Temperature

abb127	CO2	420	4.9	2.02	98.7	62	9.6	1.50
abb129	CO2	394	4.5	2.02	98.8	62	9.1	1.39

High Inlet Temperature - Coolant Mass Flow

abb114	CO2	435	5.3	2.07	109.1	63	7.2	1.53
abb115	CO2	440	5.2	2.05	104.6	63	8.7	1.57
abb116	CO2	436	5.2	2.06	106.9	63	7.2	1.53
abb132	CO2	439	5.3	2.03	98.6	64	12.0	1.58
abb133	CO2	441	5.3	2.03	100.4	64	12.1	1.59

Table 3.4: Coolant Orifice Configurations

	Vane	Blade	Casing		
Orifice Configuration 1, in	0.7515	0.4853	0.1548	0.1550	0.1549
Orifice Configuration 2, in	0.8232	0.5297	0.1706	0.1711	0.1719
Orifice Configuration 3, in	0.9500	0.6140	0.1955	0.1690	0.1965
Downstream Volumes, ft^3	0.25	0.45	0.05		

An orifice discharge coefficient of 0.838 is used for each of the orifices, as recommended by Ward-Smith [] [6]. C_r was calculated using the same procedure outlined in Section 3.2.1. The transient correction was calculated using the volumes listed in Table 3.4 and a sliding linear curve fit of the coolant manifold density. The orifice diameters for the there cooling configurations tested are also shown in Table 3.4. Figure 3-29 and Figure 3-30 show the cooling system temperature and pressure ratios for a typical cooled experiment. The coolant system pressures and temperatures are normalized by the turbine inlet quantities. The ratios remain constant through out the test window. The measured mass flows for the cooling system are shown in Figure 3-31.

Film-Cooled Turbine Ideal Work

The ideal enthalpy change across the cooled turbine is the mass weighted ideal enthalpy change of each of the mainstream, NGV, rotor and heatshield streams.

$$\begin{aligned}\mathcal{P}_{Ideal} = &(\dot{m}_c - \dot{m}_n - \dot{m}_r - \dot{m}_h)\left(h\left(T_{t\,a}, P_{t\,a}\right) - h\left(T_{t\,c_{is}}, P_{t\,c}\right)\right) \\ &+ \dot{m}_n\left(h\left(T_{t\,n}, P_{t\,n}\right) - h\left(T_{t\,n_{is}}, P_{t\,c}\right)\right) \\ &+ \dot{m}_r\left(h\left(T_{t\,r}, P_{t\,c}\right) - h\left(T_{t\,r_{is}}, P_{t\,c}\right)\right) \\ &+ \dot{m}_h\left(h\left(T_{t\,h}, P_{t\,h}\right) - h\left(T_{t\,h_{is}}, P_{t\,c}\right)\right)\end{aligned} \tag{3.18}$$

$T_{t\,n_{is}}$, $T_{t\,r_{is}}$,and $T_{t\,h_{is}}$ are the isentropic outlet temperatures for the NGV, rotor, and heatshield. Each is calculated, assuming an isentropic expansion from their respective cooling manifolds to the measured outlet total pressure.

[6]The length-to-diameter ratio for these orifices was kept between 1 to 6, as recommended.

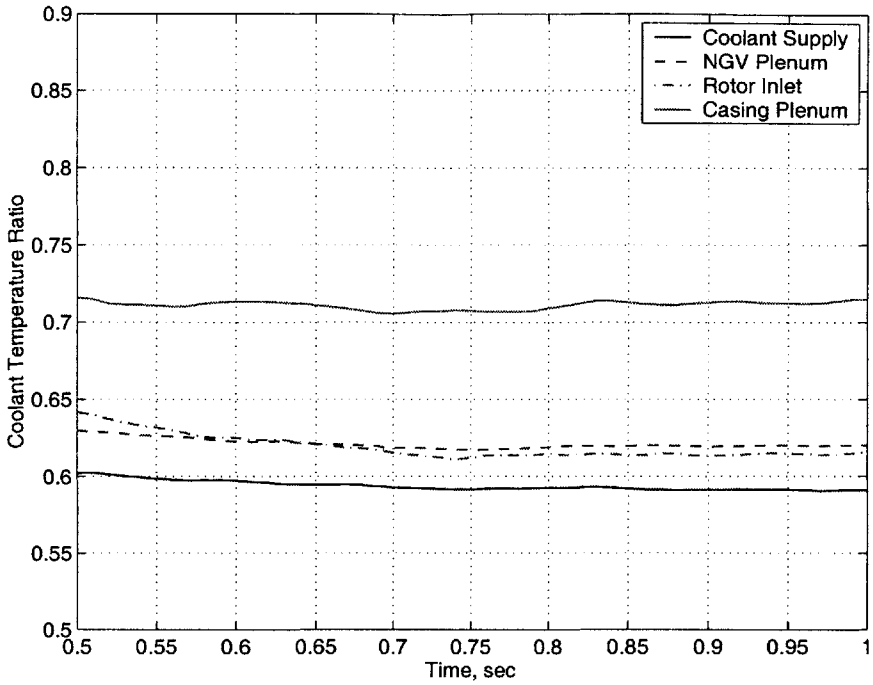

Figure 3-29: Cooling System Temperatures

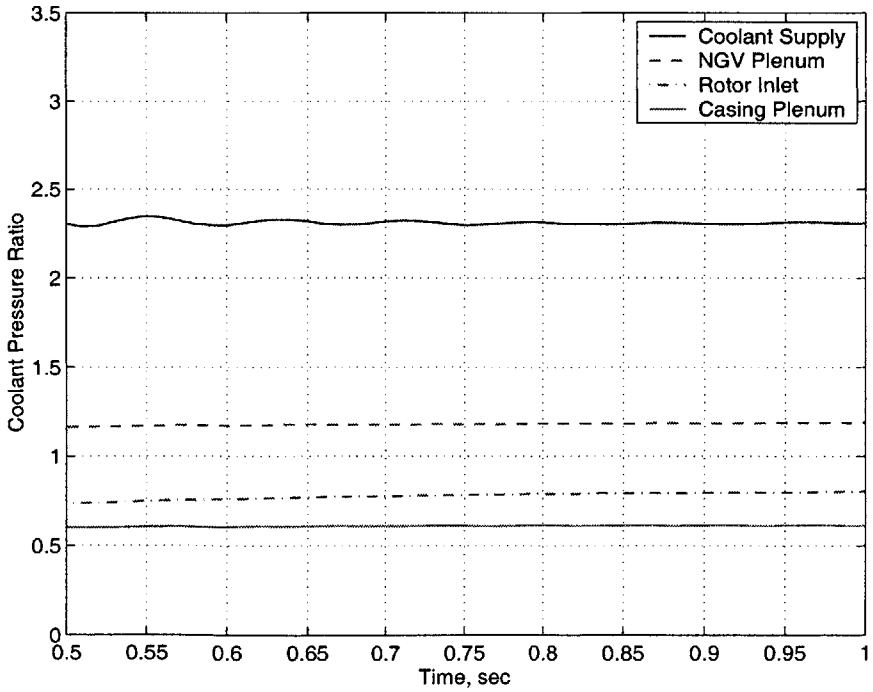

Figure 3-30: Cooling System Pressures

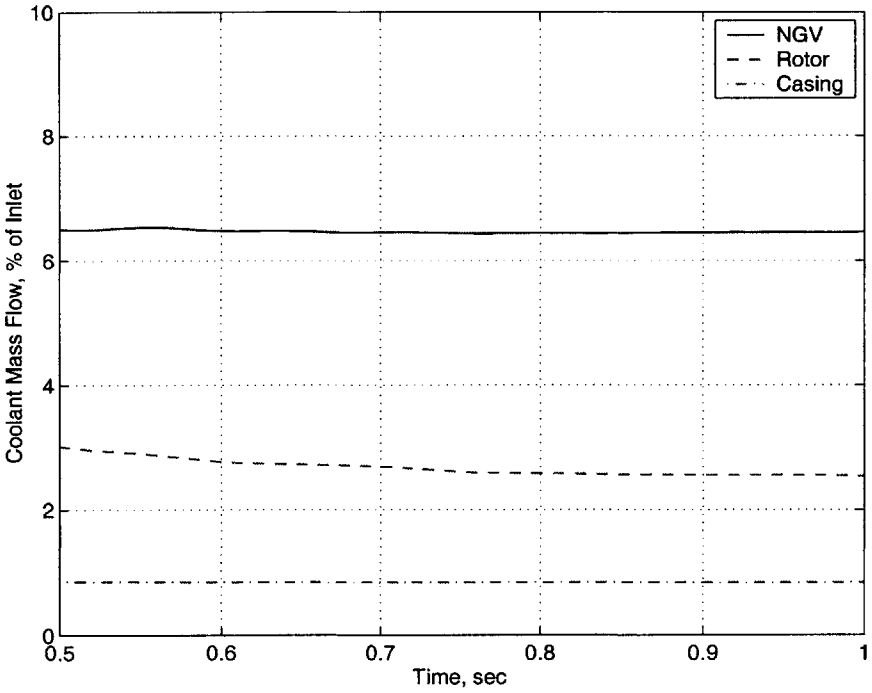

Figure 3-31: Coolant Mass Flow

3.3.2 Film-Cooled Turbine Performance Map

The same procedure as was described for the baseline stage was used to build the film-cooled stage performance map . The results for the quadratic curve fit for efficiency and corrected mass flow are shown in Table 3.5 and figures 3-33 and 3-36. Figures 3-34 and 3-37 show the efficiency and corrected mass as a function of pressure ratio for the design corrected speed. Figures 3-35 and 3-38 show the efficiency and corrected mass as a function corrected speed for the design pressure ratio. At the design point the stage efficiency has been reduced by approximately 1.7% due to film-cooling. As seen in figures 3-34 and 3-35 the film-cooled efficiency measurements are less repeatable than for the baseline tests. Based on the standard deviation of the film-cooled quadratic curve fit of the data the estimated uncertainty for back-to-back measurements is 0.45%.

Figure 3-39 shows the variation of stage efficiency with coolant-to-mainstream mass flow ratio for the two coolant temperature ratios tested. At the design coolant mass flow, the stage efficiency is reduced by 0.5% for each additional 1.0% of coolant added. The film-cooled design point efficiency is reduced by 1.75% with a cooling flow of 10%, which corresponds to an overall sensitivity of 0.175% per percent of cooling flow. The sensitivity increases at increased cooling flows. The sensitivity to cooling flow increases for the low coolant temperature (low density ratio) ratio tests.

Figures 3-37 and 3-38 show how the stage corrected mass flow varies with operating point for the film-cooled turbine. The trends are significantly different than the baseline tests; the corrected mass flow does not plateau as the pressure ratio is increased, or as the corrected speed is reduced. At reduced corrected speeds and higher pressure ratios, the baseline vane throat Mach number approached unity, which limits the corrected mass flow. For the film-cooled stage the vane throat Mach number is reduced and this plateau is not observed. Figure 3-40 shows the variation of stage corrected mass flow with coolant-to-mainstream mass flow ratio for the two coolant temperature ratios tested. For each additional 1% of coolant the stage corrected mass flow [7] increases by 0.5%. The corrected mass flow for the low coolant-to-mainstream temperature ratio is reduced by approximately 1%.

Table 3.5: Film-Cooled Turbine Performance Map

Parameter	Test Condition	A_1	B_1	B_2	C_1	C_2
η	Design Coolant	-0.017	-4.229e-002	-1.554e-001	1.353e-003 -	4.51e -006
W_c	Design Coolant	103.22	5.978e+000	0.0	-6.137e-002	0.0

[7] Based on inlet total pressure and temperature and exit mass flow.

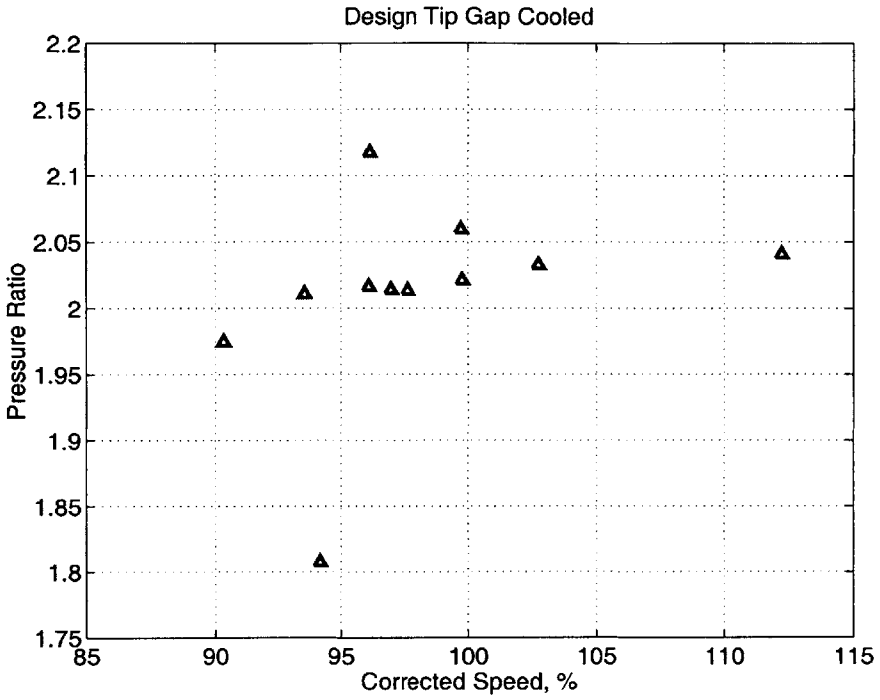

Figure 3-32: Film-Cooled Operating Points

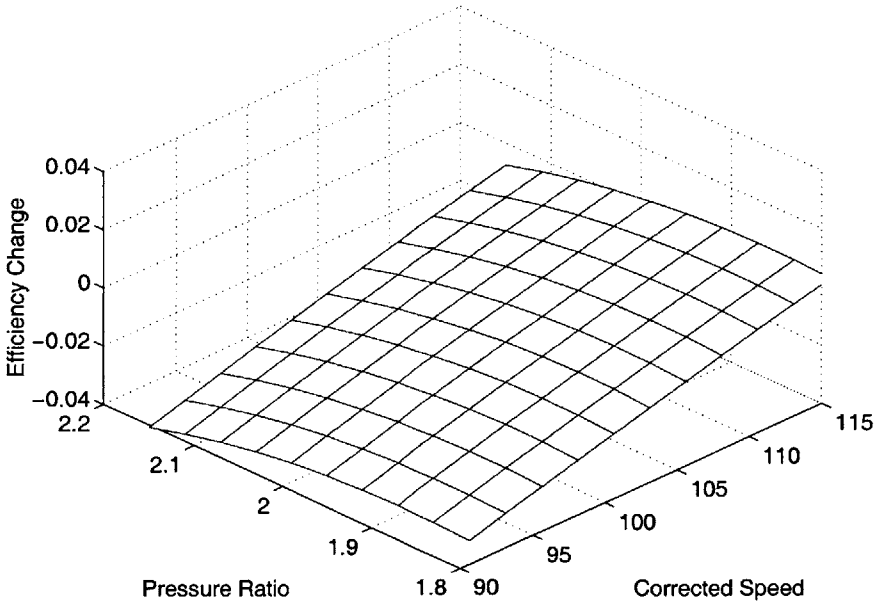

Figure 3-33: Isentropic Efficiency vs. Operating Point

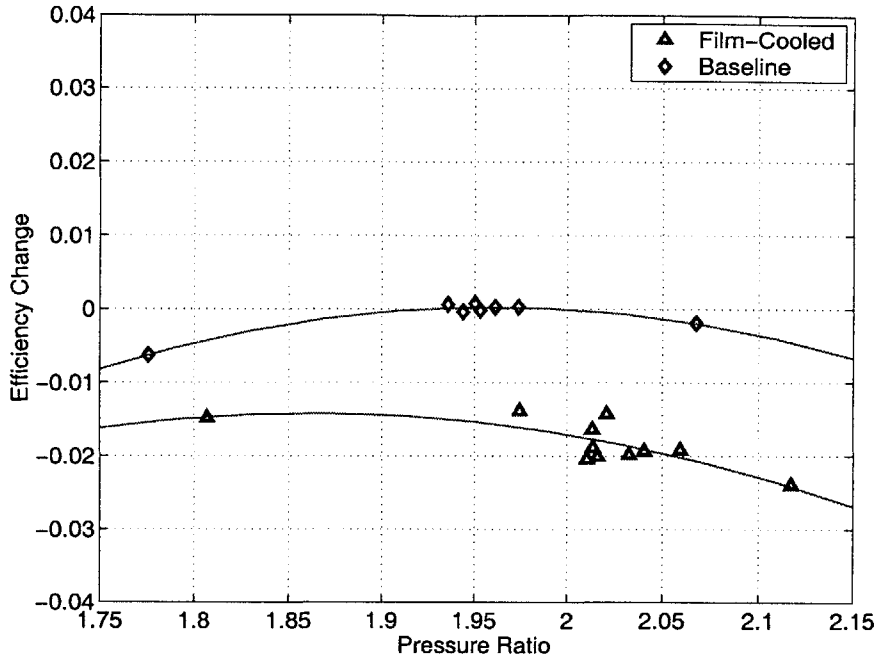

Figure 3-34: Isentropic Efficiency vs. Pressure Ratio

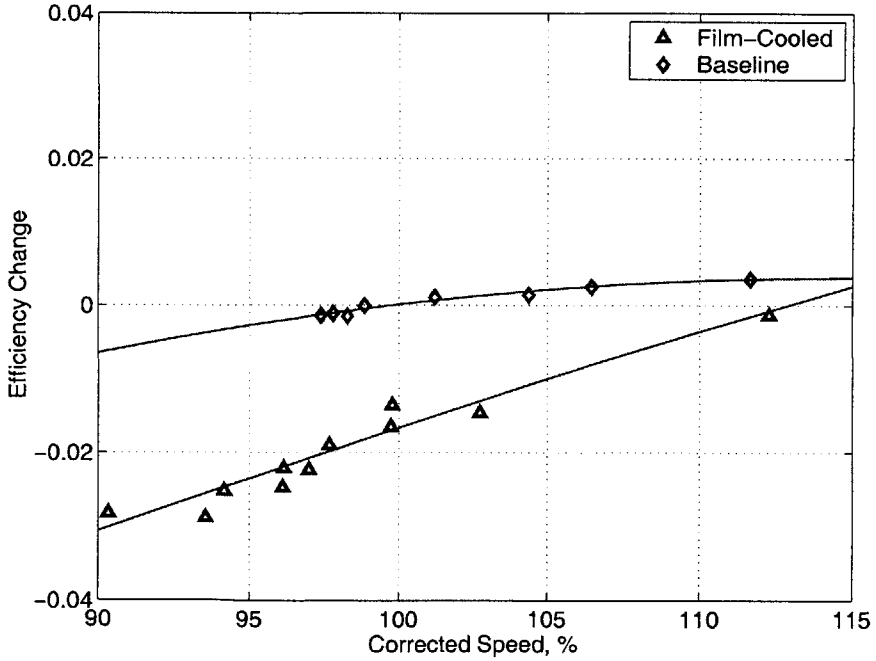

Figure 3-35: Isentropic Efficiency vs. Corrected Speed

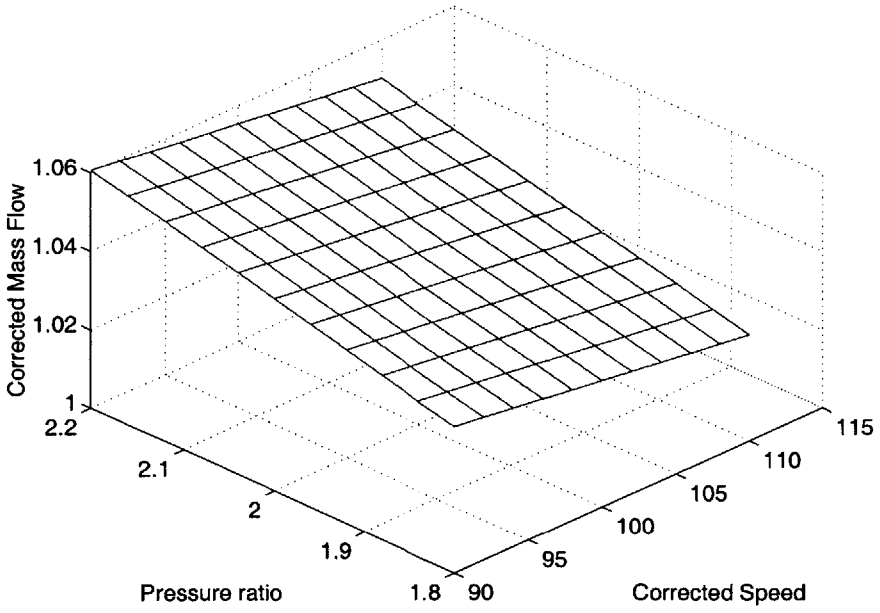

Figure 3-36: Corrected Mass Flow vs. Operating Point

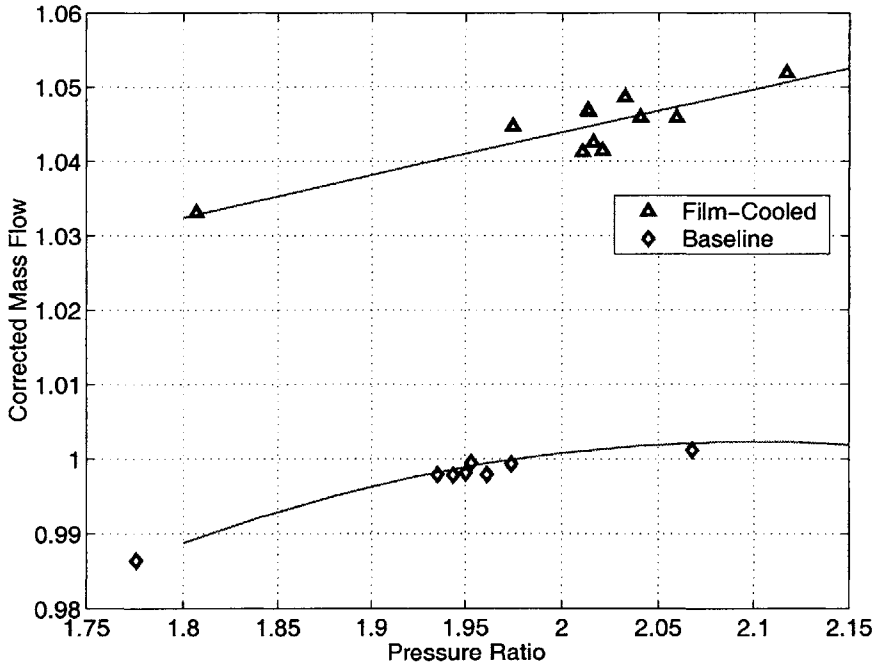

Figure 3-37: Corrected Mass Flow vs. Pressure Ratio

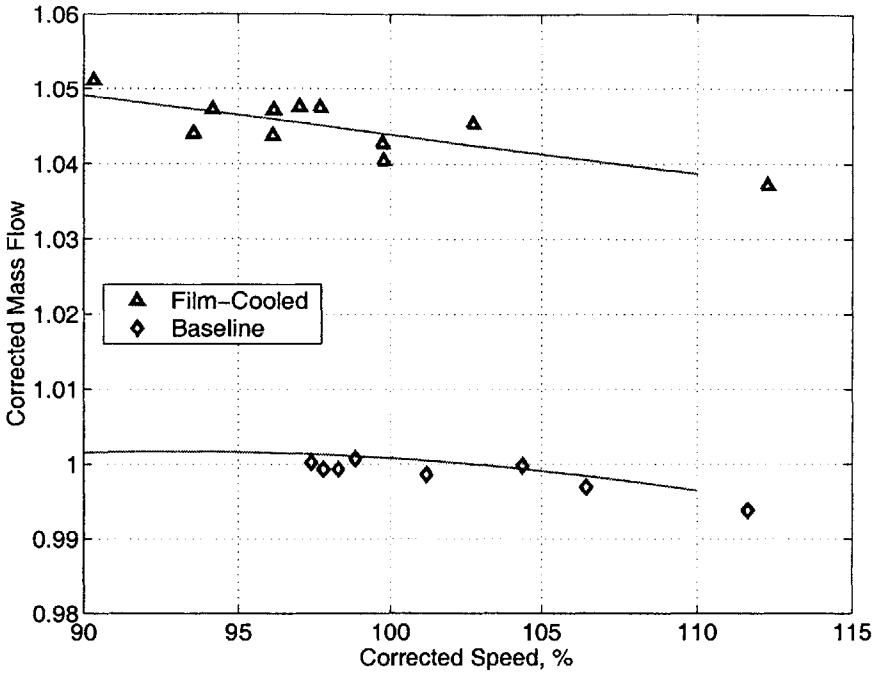

Figure 3-38: Corrected Mass Flow vs. Corrected Speed

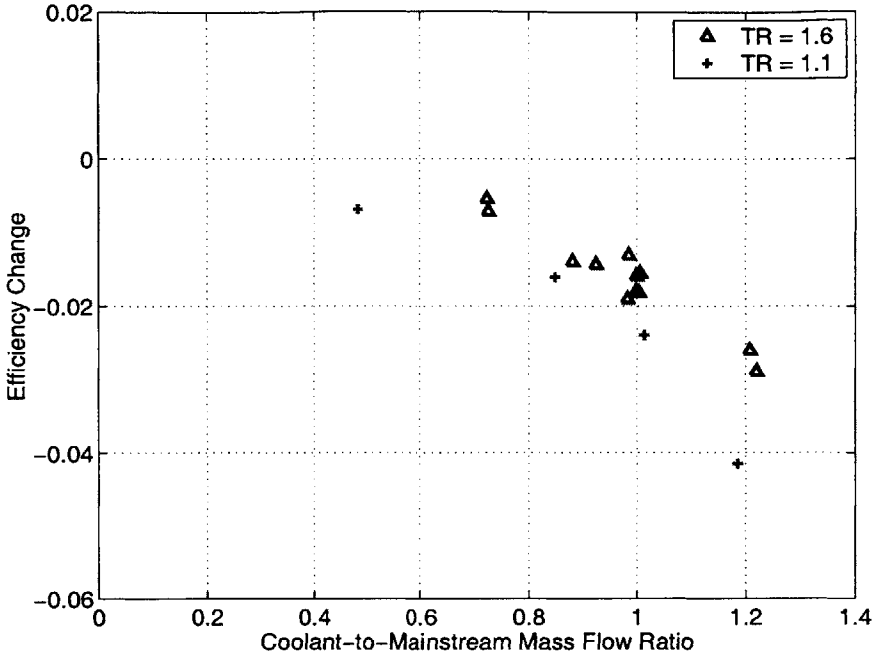

Figure 3-39: Isentropic Efficiency vs. Coolant Mass Flow Ratio

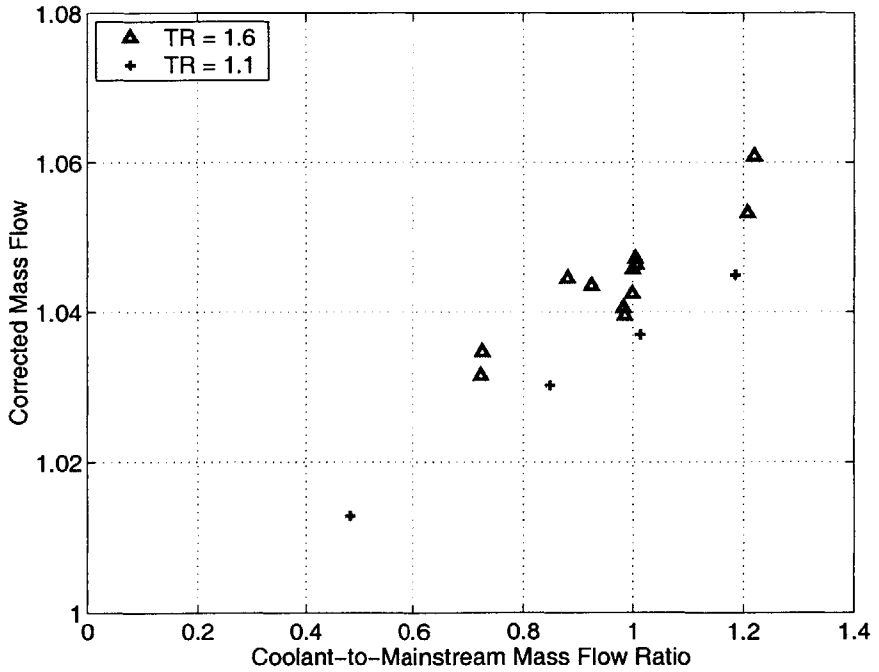

Figure 3-40: Corrected Mass Flow vs. Coolant Mass Flow Ratio

3.3.3 Inlet Temperature Test Matrix

Figure 3-42 shows the results of a series of tests to examine the influence of turbine inlet temperature, or heat load, on the isentropic efficiency of the film-cooled stage. For these tests the inlet Reynolds number and the vane coolant-to-mainstream momentum flux ratio were held constant as the inlet temperature was varied. The momentum flux ratio is defined as:

$$I = \left(\frac{MFR}{MFR_{design}}\right)^2 \frac{TR_{design}}{TR} \tag{3.19}$$

Figure 3-41 shows the measured efficiencies for the two temperature ratios tested as a function of momentum flux ratio. This comparison shows that change in efficiency scales with momentum flux ratio near the design point. the design point Within the uncertainty of the measurements, no variation in efficiency is observed as the heat load is varied.

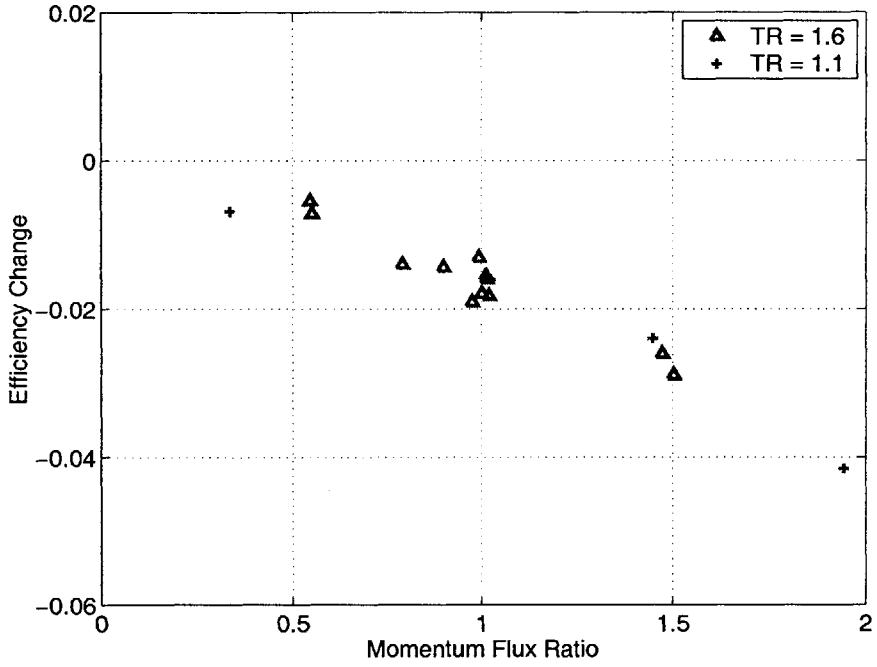

Figure 3-41: Isentropic Efficiency vs. Turbine Inlet Temperature

3.4 Summary

The data reduction procedures for the newly developed measurement techniques have been presented and discussed. The performance of the baseline stage has been characterized and the influence of the rotor tip gap measured for this stage. The stage efficiency is reduced 1.7% for each percent increase in rotor tip gap. The efficiency sensitivity to tip gap increases with corrected speed. The nozzle guide vane heat load was reduced by approximately 40% and no change in stage efficiency was observed. The estimated uncertainty

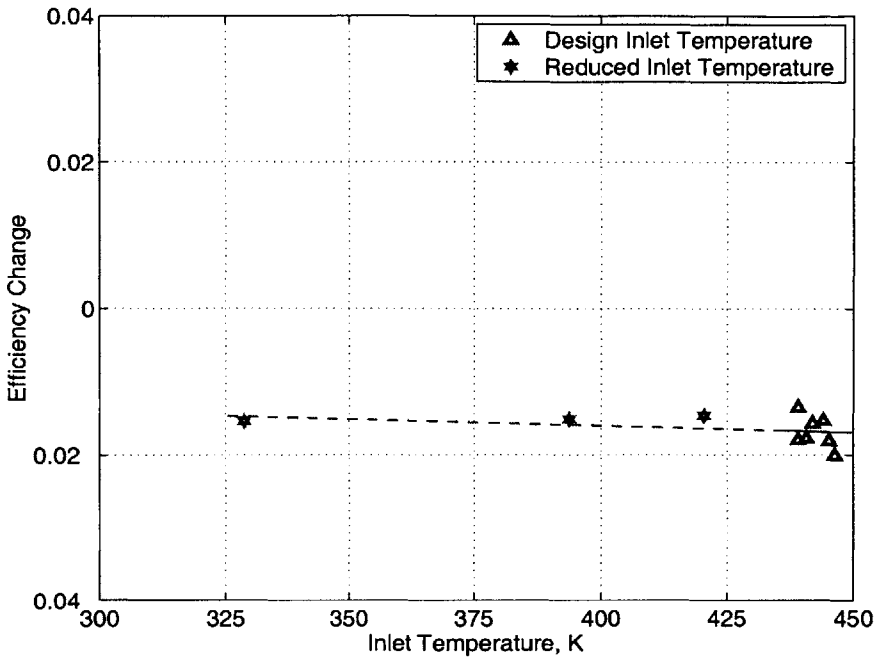

Figure 3-42: Isentropic Efficiency vs. Turbine Inlet Temperature

(U_{95}) for the baseline stage efficiency is 0.40%, and for back-to-back measurements the uncertainty is 0.14%.

The performance of the film-cooled stage has been characterized. At the design coolant mass flow and temperature ratio the stage efficiency was reduced by 1.75% when compared to the baseline stage. At the design operating point each additional percent of cooling flow reduces the stage efficiency by 0.5%. Also at the design operating point each additional percent of cooling flow increases corrected mass flow by 0.5%. Within the measurement uncertainty of the data, the increasing loss with coolant mass flow scaled with coolant-to-mainstream momentum flux ratio. Also, no change in stage efficiency was observed as the when the mainstream-to-metal temperature ratio (or turbine heat load) was varied. The estimated uncertainty (U_{95}) for the film-cooled stage efficiency is 0.53%, and for back-to-back measurements the uncertainty is 0.38%.

Chapter 4 will present an analytical definition of the film-cooled turbine efficiency that can be used to model the performance of the turbine. Chapter 5 presents a meanline velocity triangle model of the stage and that was used predict the performance of an ideal turbine with the same airfoil Mach number distributions and velocit triangles. The experimental results for the film-cooled stage are compared with the model to estimate the loss due to film-cooling.

Chapter 4

Dissection of Film-Cooled Turbine Isentropic Efficiency

For the experimental results presented in this thesis, the isentropic efficiency of the turbine is defined as the ratio of the measured turbine power to the power that would be extracted if each of the inlet streams were isentropically expanded to a common exit total pressure. This chapter presents the analytic equivalent of this definition of turbine efficiency. This analytic definition of turbine efficiency will be used in Chapters 5 and 6 to compare the experimental and analytical results. The efficiency definition proposed in this chapter will be verified in Chapter 6 where an analytical model of the turbine stage is compared with the experimentally measured results.

4.1 Background

The isentropic efficiency of a turbine stage is defined as the ratio of actual work output to work output that would be obtained in a corresponding reversible process. Equation 4.1 is commonly used to determine the experimentally measured turbine isentropic efficiency:

$$\eta_{is} = \frac{\mathcal{T}\Omega}{\sum_{j=1}^{n} \dot{m}_j c_p T_{t\,j} \left(1 - \pi_j^{\frac{\gamma-1}{\gamma}}\right)} \tag{4.1}$$

The denominator of this expression reveals that, for streams from a common pressure source, the temperature of thermodynamic significance is the mass averaged total temperature, regardless of the distribution

between streams. It also shows that all streams flowing through the turbine are capable of doing work. [1]

All of the losses must be considered to model a film-cooled turbine stage, specifically - for all of the inlet streams from the inlet measurement plane to the turbine exit. Dring and Heiser (1980) [2] proposed the following definition of efficiency for a multi-flow cooled turbine:

$$\eta_{is} = \frac{\sum_{j=1}^{n} \dot{m}_j T_{t\,j} \left(1 - e^{\frac{\Delta s}{c_p}} \pi_j^{\frac{\gamma-1}{\gamma}}\right)}{\sum_{j=1}^{n} \dot{m}_j T_{t\,j} \left(1 - \pi_j^{\frac{\gamma-1}{\gamma}}\right)} \tag{4.2}$$

The following discussion (Figure4.1 also) is quoted directly from Dring and Heiser: 'Even though the turbine appears to have both steady and unsteady flow processes taking place, when viewed from any single reference frame, the path traversed by each particle of fluid passing through the machine can be thought of as consisting of a series of steady flow processes viewed from appropriate frames of reference. Each of these sequential steady flow processes, viewed from its appropriate frame of reference (alternatively stationary or rotating), will be referred to as a unit process. The special advantage of this approach is that the total entropy change for any particle of fluid is equal to the sum of all the unit processes, for entropy is a state process and does not depend upon frames of reference.'. The following discussion will expand on this definition.

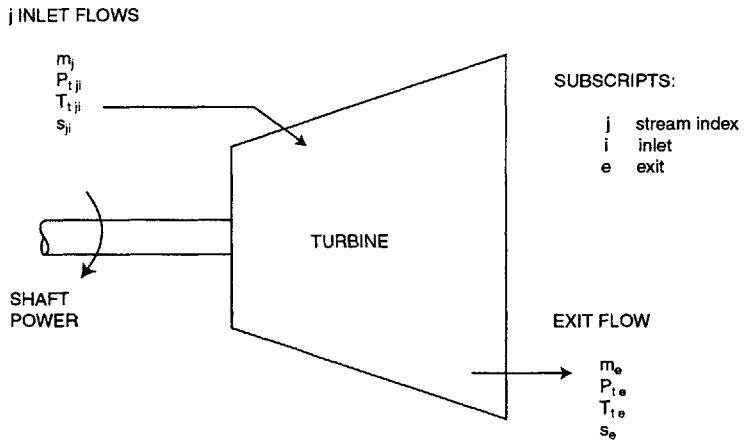

Figure 4-1: Schematic Representation of a Multi-Flow Cooled Turbine.

[1] In practice real gas effects are also accounted for, and for a short duration test the deceleration of the rotor is also considered.

[2] Also Anderson and Heiser (1968)

4.2 Discussion

The ideal work as each of the streams expand isentropically to a common exit pressure is represented by the denominator of Equation 4.1. The ideal outlet temperature of the streams is not necessarily the same for all streams. Hence, to avoid confusion, the denominator in Equation 4.1 should be referred to as the *unmixed isentropic work* for the stage. Ideally, further work could be extracted from the streams as they are brought to a common isentropic exit temperature. This is depicted in Figure 4.2 with a Carnot cycle operating between the exit streams. The common isentropic outlet temperature can be calculated by matching the entropy transfer from the mainstream to the coolant stream. For the Carnot cycle the flow is assumed to be at a low Mach number and the exit total pressure is constant:

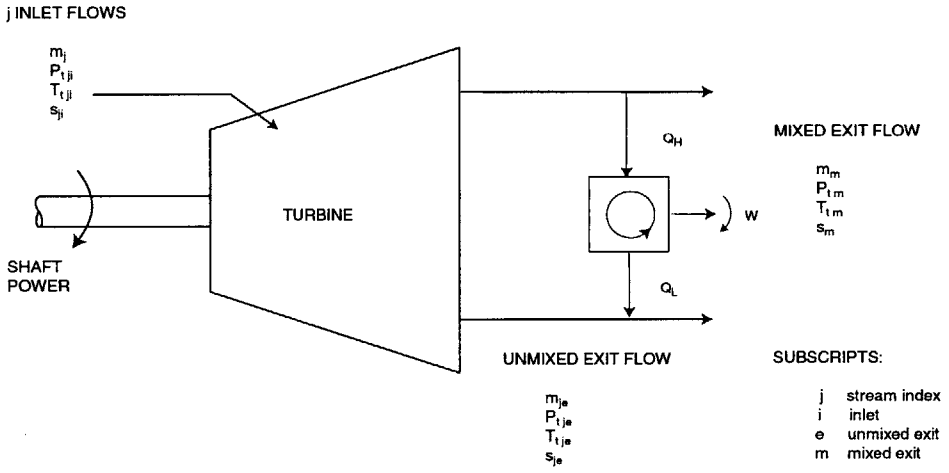

Figure 4-2: Schematic Representation of a Multi-Flow Cooled Turbine with a Carnot Cycle.

$$\frac{s_m - s_j}{c_p} = ln\left(\frac{T_{m\,is}}{T_{is\,j}}\right)$$

For an isentropic process, the sum of the mass weighted entropy change of the streams is zero [3]:

$$\sum_{j=1}^{n} \dot{m}_j\, ln\left(\frac{T_{m\,is}}{T_{is\,j}}\right) = 0$$

From this expression a single ideal mixed outlet temperature can be derived:

$$T_{m\,is} = \prod_{j=1}^{n} \left(T_{t\,j}\pi_j^{\frac{\gamma-1}{\gamma}}\right)^{\frac{\dot{m}_j}{\sum_{j=1}^{n}\dot{m}_j}}$$

[3]More detail is given in Appendix A

Based on this common isentropic exit temperature the multi-inflow *mixed isentropic efficiency* can be defined:

$$\eta_{is} = \frac{\sum_{j=1}^{n} \dot{m}_j T_{t\,j} \left(1 - e^{\frac{\Delta s}{c_p}} \pi_j^{\frac{\gamma-1}{\gamma}}\right)}{\sum_{j=1}^{n} \dot{m}_j T_{t\,j} - \sum_{j=1}^{n} \dot{m}_j \underbrace{\prod_{j=1}^{n} \left(T_{t\,j}\, \pi_j^{\frac{\gamma-1}{\gamma}}\right)^{\frac{\dot{m}_j}{\sum_{j=1}^{n} \dot{m}_j}}}_{T_{m\,is}}} \tag{4.3}$$

The unit process entropy change for each of the j setarate streams is given by:

$$\frac{\Delta s}{c_p} = ln\left(1 + \frac{\Delta T_t}{T_{t\,j}}\right) - \frac{\gamma - 1}{\gamma} ln\left(1 + \frac{\Delta P_t}{P_{t\,j}}\right) \tag{4.4}$$

Comparing the denominator of Equation 4.3 with Dring and Heiser's original formulation, it is clear that the ideal work in Equation 4.2 should be referred to as the *unmixed isentropic work*. The difference between the *mixed* and *unmixed isentropic work* represents an additional source of work. The inability to extract this additional source of work from the flows is reflected in the entropy generation due to the thermal mixing of the streams. In order to correctly define an efficiency based on *unmixed isentropic work*, the entropy generation due to the thermal mixing of the streams must *not* be included in the definition of the real work. In other words, to correctly define the isentropic efficiency in Dring and Heiser's unmixed sense (equation 4.2), the total entropy change must be replaced with the entropy change due to pressure loss only. This yields the definition of unmixed isentropic efficiency:

$$\eta_{is} = \frac{\sum_{j=1}^{n} \dot{m}_j T_{t\,j} \left(1 - e^{\left(\frac{\Delta s_{pr}}{c_p}\right)} \pi_j^{\frac{\gamma-1}{\gamma}}\right)}{\sum_{j=1}^{n} \dot{m}_j T_{t\,j} \left(1 - \pi_j^{\frac{\gamma-1}{\gamma}}\right)} \tag{4.5}$$

The relevant unit process entropy change for the *unmixed isentropic efficiency* is defined as:

$$\frac{\Delta s_{pr}}{c_p} = -\frac{\gamma - 1}{\gamma} ln\left(1 + \frac{\Delta P_t}{P_{t\,j}}\right) \tag{4.6}$$

The following example is considered to better appreciate the source of the lost work due to thermal mixing and to elucidate the difference between these two interpretations. Consider the system shown in Figure 4.2 which is representative of a combustor and multi-flow turbine. A portion of the inflow bypasses the heat addition process and enters the turbine. The ratio of the mixed to unmixed isentropic work for

this system is expressed in equation 4.6:

$$\frac{W_{is\ mixed}}{W_{is\ unmixed}} = \frac{\sum_{j=1}^{n} \dot{m}_j T_{t\,j} - \sum_{j=1}^{n} \dot{m}_j \prod_{j=1}^{n} \left(T_{t\,j}\, \pi_j^{\frac{\gamma-1}{\gamma}} \right)^{\frac{\dot{m}_j}{\sum_{j=1}^{n} \dot{m}_j}}}{\sum_{j=1}^{n} \dot{m}_j T_{t\,j} \left(1 - \pi_j^{\frac{\gamma-1}{\gamma}} \right)} \tag{4.7}$$

Figure 4.2 shows the effect of changing the magnitude of the bypass flow on the lost work due to thermal

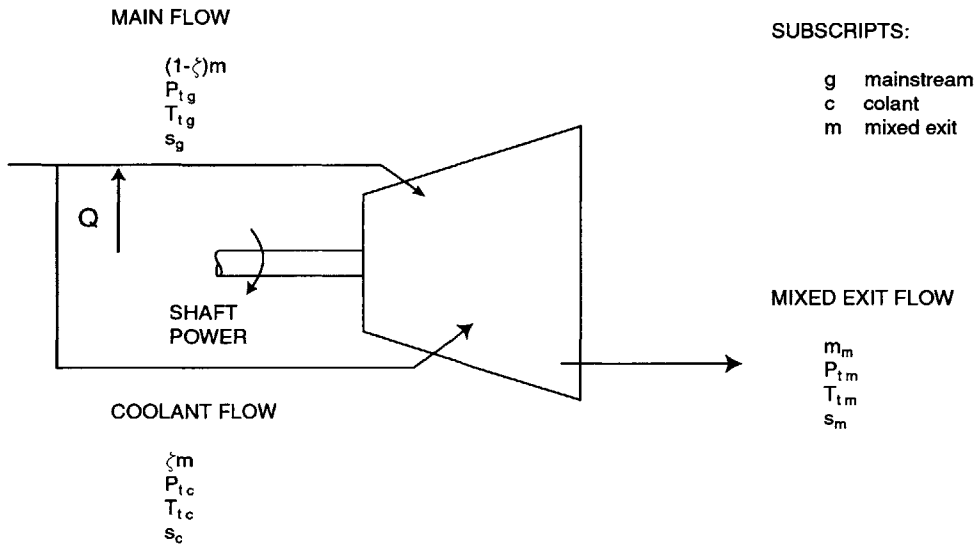

Figure 4-3: Schematic Representation of a Film-Cooled Turbine.

mixing. The mainstream-to-coolant total temperature ratio for zero bypass flow is 2.0 and the total-to-total pressure ratio across the system is 2.0. For a bypass flow of 10% the lost work due to thermal mixing is approximately 15% of the unmixed isentropic work. Denton (1993) suggested that entropy generation due to thermal mixing should not be included as a source of loss for film-cooled turbines. He asserted that the irreversiblities are based solely on viscous effects and not differences in temperature. However, in contradiction to Denton's reasoning, the thermal mixing of the mainstream and coolant flow is irreversible, and does result in entropy generation. The lost work due to thermal mixing should not be regarded as a 'real' loss because it is merely a result of the way in which heat is introduced into the system. The same process occurs in the combustor where the fuel is initially burned in a high temperature fuel rich zone and then quenched using dilution jets. In this case the lost work due to the thermal mixing of the streams is not counted as a 'real' loss. Therefore the *mixed isentropic efficiency*, although technically correct, is *not* recommended for use in multi-flow turbines. It is introduced to illustrate that the entropy generation due to thermal mixing should *not* be included in the definition of the *unmixed isentropic efficiency*. As can be judged from Figure 4.2, this assumption is critical in predicting the performance of a film-cooled turbine stage. The *unmixed isentropic efficiency*, as presented in this chapter, will be used to model the

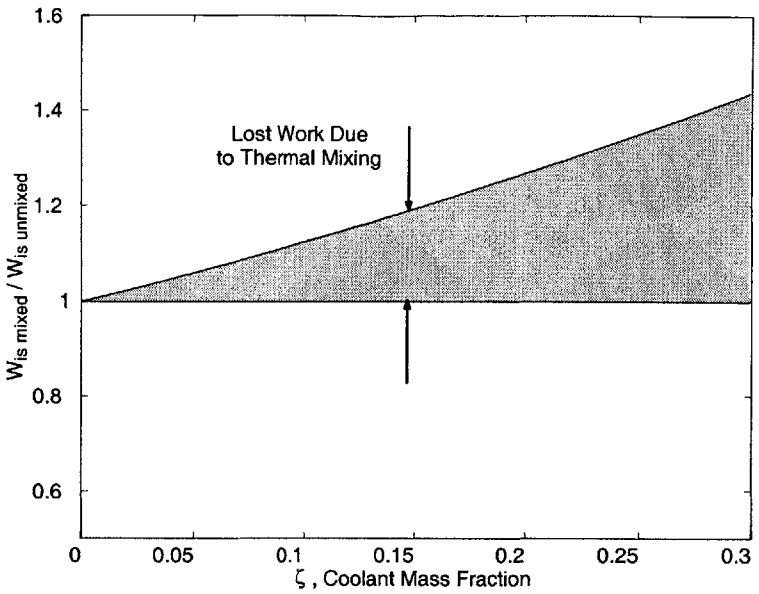

Figure 4-4: Lost Work Due to Thermal Mixing in a Cooled Turbine.

performance of the turbine stage in Chapter 5.

4.3 Summary

The definition of turbine efficiency, presented by Dring and Heiser (1980), defined the ideal turbine work as the sum isentropic work for each of the inlet streams as they are expanded to a common exit total pressure. This definition does not include the additional work that could be extracted by bringing the ideal exit flows to a common isentropic temperature. However, their definition of the real work does include the loss associated with not extracting this source of additional work. The definition of turbine efficiency presented by Dring and Heiser (1980) is not a suitable measure of turbine performance because it is not based on consistent definitions of the real and ideal turbine work.

Two valid measures of turbine performance are presented, the *mixed isentropic* efficiency and the *unmixed isentropic* efficiency. The *mixed isentropic* efficiency was presented to illustrate the role of entropy generation due to thermal mixing of the mainstream and coolant flows. Although valid, this is not a useful measure of turbine performance as the ideal turbine work varies with coolant mass fraction.

The *unmixed isentropic* efficiency, on the other hand is both valid and useful. In Chapter 6 the measured turbine efficiency will be compared to a model of the turbine stage in which each unit process for each stream is considered. The analysis presented in chapter concludes that the entropy generation due to the thermal mixing of the mainstream and coolant flows is not relevant to the performance of a film-cooled turbine stage.

Chapter 5

Performance of an Ideal Uncooled Turbine Stage

5.1 Introduction

An appropriate baseline to compare the film-cooled turbine against is an ideal turbine, without any temperature limitations or cooling, for the same work output. It is difficult to identify the loss caused by film-cooling from the overall performance measurement. To extract the loss due to film-cooling, the experimental results should be compared with an ideal stage that has the same velocity triangles and airfoil Mach number distributions, but without coolant injection. However, the film-cooling flow is an integral part of stage design and it is required to maintain the airfoil Mach number distributions and stage reaction. If the stage is tested without coolant, the reaction rate will decease and the resulting efficiency will be lower than that of the ideal stage. If the blockage caused by film-cooling was known, the airfoil profile and endwall contours could be redesigned to account for the coolant deficit, and thereby maintain Mach number distributions and boundary layer parameters, similar to the ideal stage. However, this would result in larger airfoil trailing edge thicknesses, an increased trailing edge loss and a change in the trailing edge deviation angle. As the trailing edge loss is one of the most poorly understood turbine loss mechanisms, a change in the trailing edge thickness is not desirable. Also the blockage caused by coolant injection cannot be precisely predicted. There is no uncooled turbine geometry that would give the same Mach number distributions and stage velocity triangles as the film-cooled stage. Consequently, there is no experimental baseline that can be tested to directly determine the loss due to film-cooling.

Alternatively, an analytical model of the stage meanline velocity triangles can be used to predict the performance of the ideal stage, and thereby estimate the loss due to film-cooling. In the current study, the uncooled geometry was tested, and these results were used to calibrate a meanline velocity triangle model of the stage. This model was then used to estimate the performance of the ideal stage and the losses due to

film-cooling. This model was subsequently used to provide a detailed breakdown of the cooling losses and also to identify the cooling system losses that are unique to the MIT blowdown turbine facility.

The turbine stage model successfully predicted the measured efficiency trends for the baseline turbine tests. This model also successfully predicted the measured trends for the stage corrected mass flow with and without film-cooling for a range of corrected speeds, pressure ratios and coolant-to-mainstream mass flow and temperature ratios. The efficiency for an ideal turbine stage without any temperature limitations was estimated to be 3.0% higher than the film-cooled turbine stage at the design operating point.

5.2 Analytical Approach

A meanline velocity triangle model is used to predict the aerodynamic performance of the turbine stage. This model relates the independent parameters that describe the aerodynamic performance of the vane and blade to the independent parameters used to control the test conditions. Thereby, the vane and blade loss characteristics are used to predict the stage performance.

The independent parameters used to set the turbine operating point for the baseline turbine tests are; the total-to-total pressure ratio across the stage, the rotor corrected speed [1] and the inlet Reynolds number. For the film-cooled tests additional independent parameters include: the coolant-to-mainstream mass flow ratio and temperature ratio. The experimental results for the baseline and film-cooled turbine tests are presented in terms of these independent parameters in Chapter 3. The independent parameters used to characterize the vane and blade loss characteristics are: the blade row isentropic exit Mach numbers[2], inlet incidence angle and Reynolds number. The following methods were used to estimate the vane and blade loss characteristics:

- The vane and blade profile loss characteristics are calculated using MISES [24], a fully coupled viscous/inviscid solver. An additional loss to account for von Karman type vortex shedding off the airfoil blunt trailing edges is added to the MISES generated loss. This superposition approach is verifed using a test example of Stewart's (1955) trailing edge loss model.

- The endwall losses are estimated using a semi-analytic correlation by Sharma and Butler (1987).

- The rotor tip gap loss is estimated experimentally.

- The vane and blade surface pressure distributions are used to estimate the distribution of cooling flows within the vane and blade. Using the coolant distributions, one-dimensional mixing models which utilize the conservation of mass, momentum, and energy are used to estimate the loss and the increased mainstream Mach number associated with the injection of coolant into the mainstream

[1] The rotor speed nondimensionalized by the stage inlet flow stagnation speed of sound (or critical velocity).

[2] This is a function of the ratio of inlet total pressure to exit static pressure for the blade row and the specific heat ratio of the test gas.

flow path. Harstel's (1972) mixing-layer model, which assumes that the film-cooling flow mixes with a small[3] portion of the mainstream flow under the assumption of constant static pressure mixing, is used to estimate the mainstream loss associated with film-cooling. A modified version of Stewart's (1955) trailing edge loss model is used to model the injection of trailing-edge cooling into the mainstream flow.

These analytical techniques are used to characterize the stage loss and to estimate the influence of film-cooling and trailing-edge injection on vane exit Mach number. For a specified turbine corrected speed, coolant-to-mainstream mass flow ratio and temperature ratio the velocity triangle model iterates the vane throat Mach number until the desired operating point pressure ratio is achieved.

5.2.1 Boundary Layer Calculations

MISES[4], a fully coupled viscous/inviscid solver developed for three dimensional cascade design, was used to perform the boundary layer calculations. The inviscid flow is modeled using the steady Euler equations and a Newton-Raphson technique is used to solve the integral boundary layer equations. The three-dimensional flow through the stage is treated as an axisymmetric meridional flow. The axisymmetric stream surfaces (Figure 5-1) are defined in terms of the radius $r(z)$ and a streamtube thickness $b(z)$, where z is the axial coordinate. The meridional streamlines are determined using a through-flow method to solve the axial and radial equilibrium relations for mass, momentum, and energy given the basic stage inflow and outflow parameters and the hub and tip endwall contors. The flow over the complete span is approximated as a set of quasi-3D blade-to-blade problems for stream surfaces at several radial stations. As illustrated in Figure 5-2, the quasi-3D blade-to-blade flow is solved on the stream surface in an $m' - \theta$ coordinate system with a radius and stream tube thickness determined from the through-flow calculation (Youngren [24]).

The through-flow analysis of the turbine stage was performed by the program sponsor for the design point flow conditions. Figures 5-3(a) and 5-3(a) show the grids $(m' - \theta)$ used to perform the calculations. Figures 5-4(a) and 5-4(b) show the computed freestream isentropic Mach distributions. Osnaghi[18] experimentally studied the aerodynamic performance of the NGV design used in this turbine stage using a transonic linear cascade. Figure 5-8 presents a comparison of the computed NGV surface isentropic Mach number distributions and the measured distributions from Osnaghi's study.

The measured corrected mass flow for the baseline and film-cooled tests are used to verify the model of the turbine stage. The one-dimensional analysis used to model these tests must account for the reduced NGV throat flow area caused by film-cooling induced leading-edge boundary layer transition. Köllen [13] studied the influence of six film-cooling configurations of on performance of a isolated blade row using a transonic annular cascade. He also compared the measured losses with a boundary layer analysis with the

[3]The mixing-layer was emperically estimated to be approximately 5% of the mainstream flow for each blade surface.
[4]Multiple blade Interacting Streamtube Euler Solver.

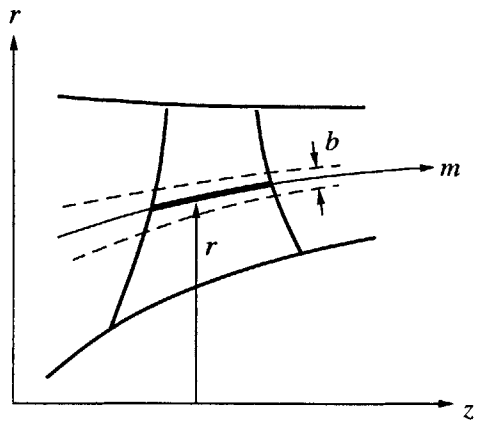

Figure 5-1: Stream Surface Defintion

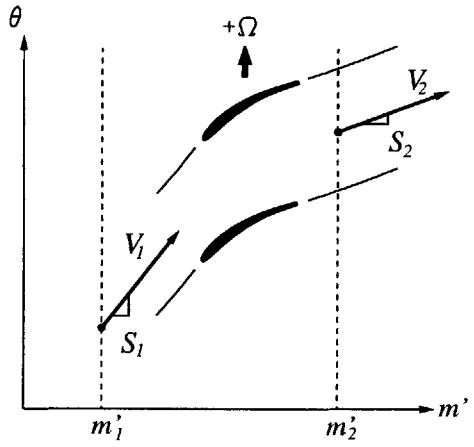

Figure 5-2: m' - θ coordinate systen

coolant mixing losses superimposed. The results compared most favorably when he forced the boundary layers to transition at the coolant injection location. Based on this result it is assumed that the vane leading-edge film-cooling will cause the airfoil boundary layers to transition from laminar to turbulent at the vane leading edge. MISES was used to estimate the reduction of turbine mass flow caused by film-cooling induced leading-edge boundary layer transition. Boundary layer transition can be either forced using transition trips, or, free using the Orr-Sommerfield criteria, or bypass as determined using the modified version of the Abu-Ghannam-Shaw bypass transition model. The turbulence characteristics of the MIT blowdown turbine facility were examined by D'Hoop [5], who measured turbulence intensity levels of 7 to 10 %. By forcing the boundary layer to transition at the airfoil leading edge, the film-cooled nozzle guide vane mass flow was reduced by 0.4% at the design point. This change in corrected mass flow is considered when comparing the results of baseline and film-cooled experiments.

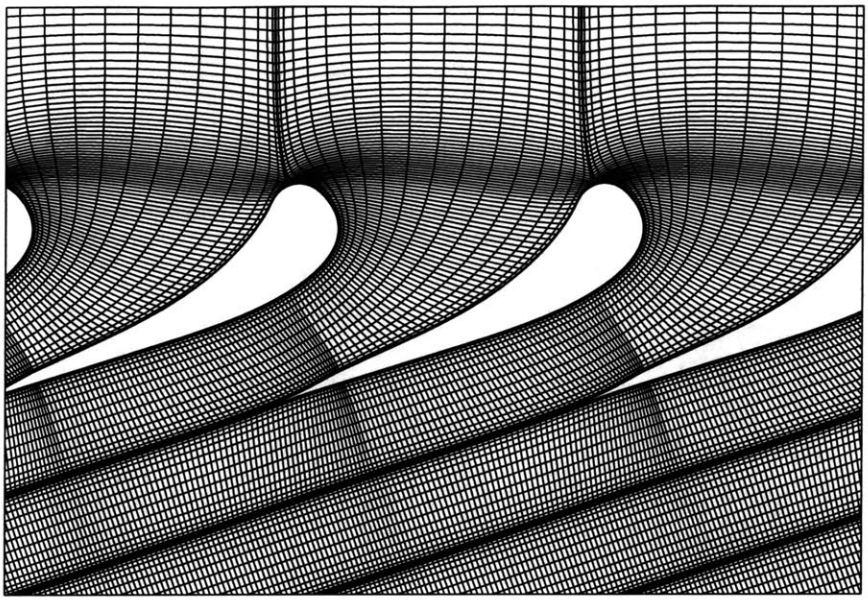

(a) Nozzle Guide Vane $m' - \theta$ Grid

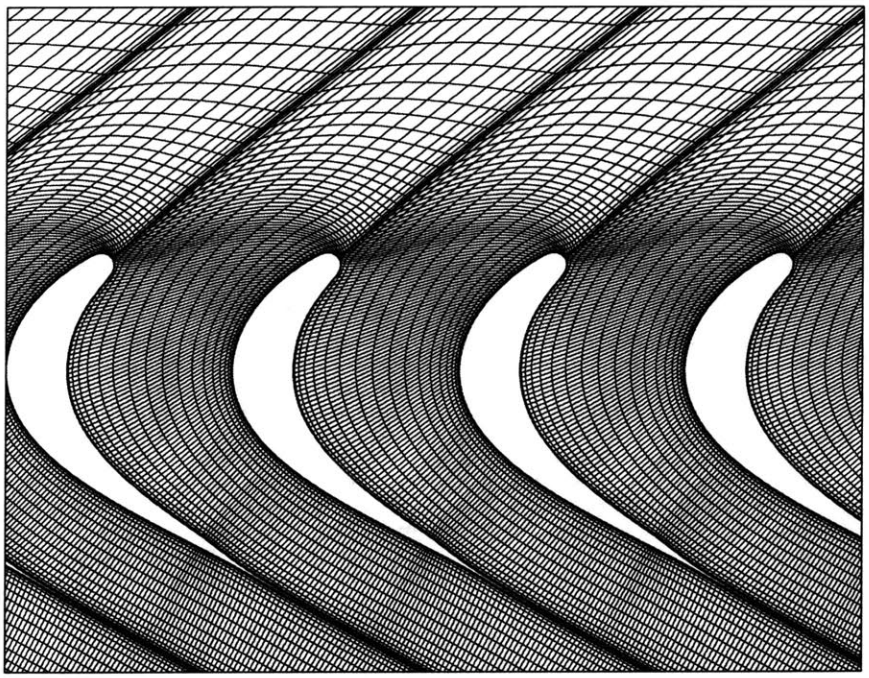

(b) Rotor Passage $m' - \theta$ Grid

Figure 5-3: MISES Computational Grids

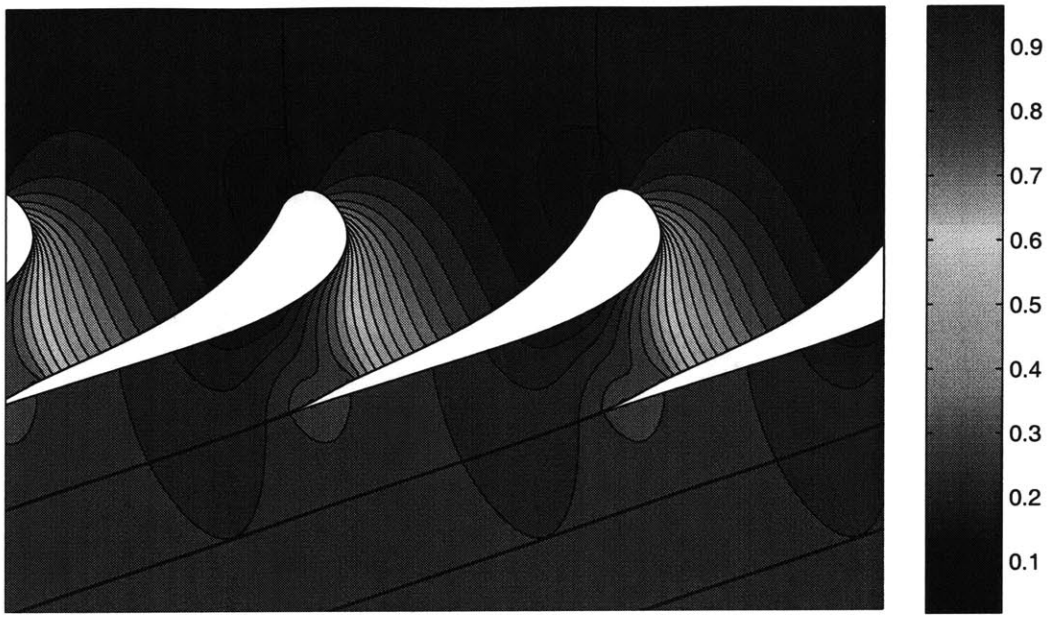

(a) Nozzle Guide Vane Freestream Mach Number Distribution

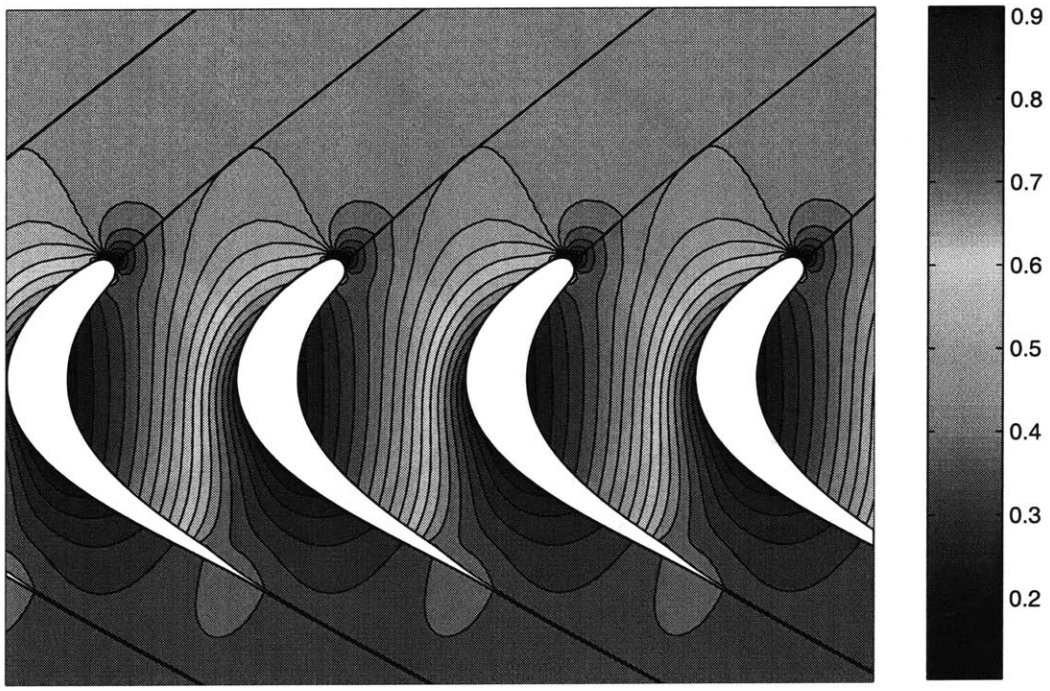

(b) Rotor Passage Freestream Mach Number Distribution

Figure 5-4: Freestream Mach Number Distributions

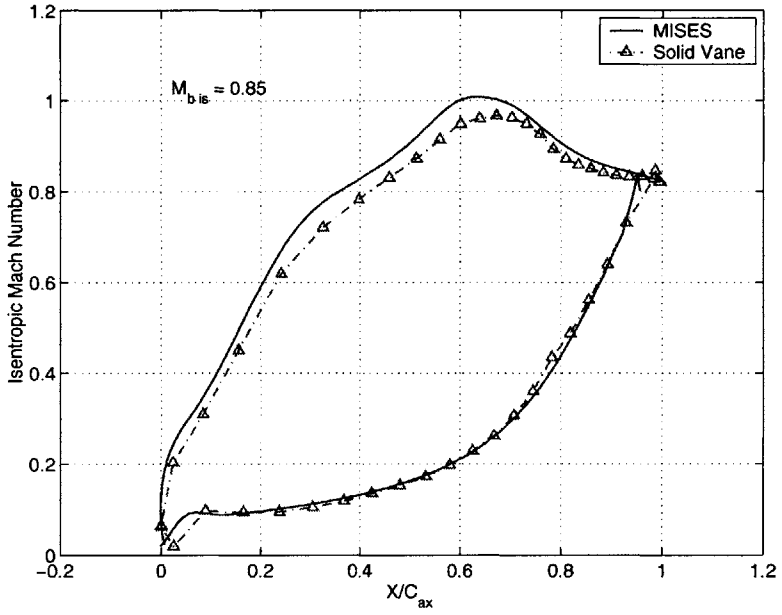

Figure 5-5: Measured Profile Isentropic Mach Number (Osnaghi) vs. CFD Prediction.

5.2.2 Coolant Injection Loss - Mixing Model Analysis

The loss associated with injecting coolant into the mainstream flow path is determined using a one-dimensional mixing model which utilize the conservation of mass, momentum, and energy. Methods such as Shapiro's [20] 'influence coefficients' can be used to gain insight into the relative importance of parameters such as mainstream Mach number, coolant mass fraction, injection angle, and the ratios of coolant-to-mainstream temperature and velocity. Equation (5.1) can be derived using the influence coefficient method:

$$\frac{\Delta P_{t_g}}{P_{t_g}} = -\frac{\gamma}{2} M_g^2 \zeta \left[1 + \frac{T_{t_c}}{T_{t_g}} - 2\frac{V_c}{V_g} \cos\alpha \right] \tag{5.1}$$

ζ is the coolant-to-mainstream mass fraction, and α is the injection angle measured from a tangent to the blade surface. The subscripts c and g represent the coolant and freestream conditions upstream of the injection location. The variation of mainstream and coolant conditions limits the usefulness of this approach. The variation of freestream Mach number across the passage prevents the mainstream from being characterized in a simple manner as required by the method of influence coefficients.

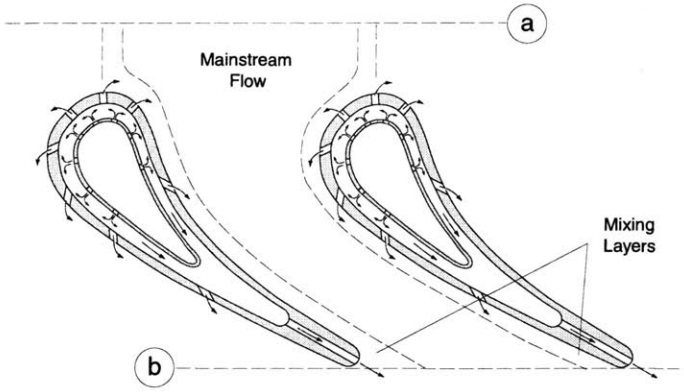

Figure 5-6: Vane Mixing Layers.

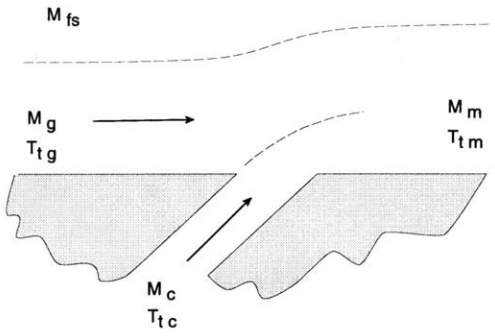

Figure 5-7: Constant Pressure Coolant Injection.

In order to overcome this limitation, Harstel (1972) developed the concept of a 'mixing layer' where the coolant is assumed to mix with a small portion of the freestream flow under constant pressure conditions. Each film-cooling row is treated as a node in a simple one-dimensional network. The overall blade pressure distribution and boundary layer parameters are assumed unchanged by coolant addition. Figure 5-8 shows the isentropic Mach number distribution for the solid vane and for three vane cooling mass flow rates. This plot shows that the Mach number distribution is not significantly influenced by film-cooling at the

design point cooling flow rates[5]. If the upper boundary of the flow shown in Figure 5-7 is assumed to be

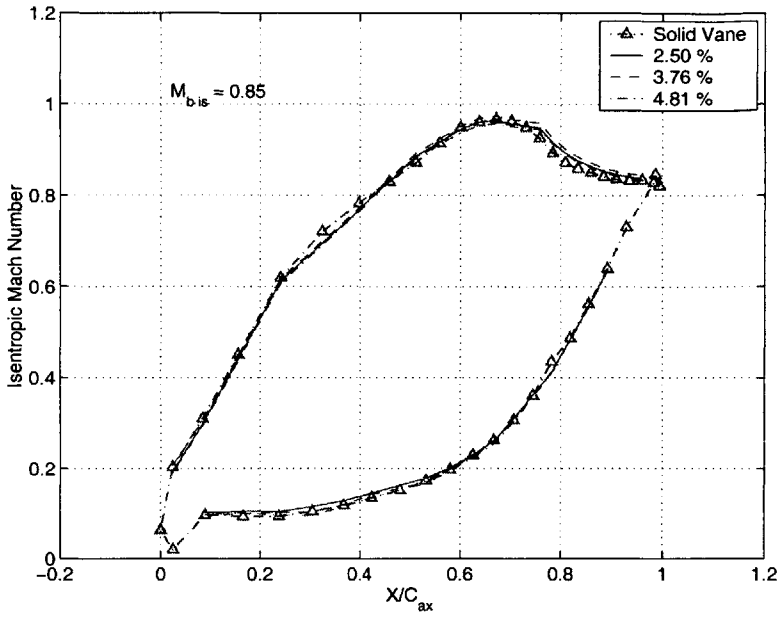

Figure 5-8: Measured Profile Isentropic Mach Numbers for Deferent NGV Coolant Flow Rates (Osnaghi).

flexible, the coolant and mainstream will mix under the assumption of constant static pressure. Applying conservation of mass, streamwise momentum and energy, and assuming a calorically perfect gas for both coolant and mainstream, the mixing layer mixed out Mach number downstream of the injection location can be calculated:

$$M_{m_j} = \left[\frac{(1+\zeta_j)\left(1+\zeta_j\left(\frac{T_{tc_j}}{T_{tg_j}}\right)\right)\left(1+\frac{\gamma-1}{2}M_{g_j}^2\right)}{\left(\left(\zeta_j \frac{M_{c_j}}{M_{g_j}}\left(\frac{T_{sc_j}}{T_{sg_j}}\right)^{\frac{1}{2}}\cos\alpha_j + 1\right)M_{g_j}\right)^2 - \frac{\gamma-1}{2}} \right]^{-\frac{1}{2}} \tag{5.2}$$

ζ_j is the coolant-to-mixing layer mass flux ratio for node j:

$$\zeta_j = \frac{\dot{m}_{c_j}}{\dot{m}_{g_j}} \tag{5.3}$$

The coolant-to-mainstream static temperature can be calculated:

$$\frac{T_{sc_j}}{T_{sg_j}} = \frac{T_{tc_j}}{T_{tg_j}}\left(\frac{1+\frac{\gamma-1}{2}M_{g_j}^2}{1+\frac{\gamma-1}{2}M_{c_j}^2}\right) \tag{5.4}$$

The mixing layer mixed out total temperature can be calculated from the conservation of energy assuming

[5]For a fixed isentropic exit Mach number.

a calorically perfect gas for both coolant and mainstream:

$$T_{m_j} = \frac{T_{tc_j}\zeta_j + T_{tg_j}}{\zeta_j + 1} \tag{5.5}$$

The upstream mixing-layer Mach number for the following node can then be calculated from the mixed out Mach number (Equation (5.2)) and the blade static pressure distribution:

$$M_{g_{j+1}} = \left[\left(\left(\frac{P_{s_j}}{P_{s_{j+1}}}\right)^{\frac{\gamma-1}{\gamma}}\left(1 + \frac{\gamma-1}{2}M_{g_j}^2\right) - 1\right)\frac{2}{\gamma-1}\right]^{\frac{1}{2}} \tag{5.6}$$

The mixing-layer mass flux is increased at each successive mode by the amount of cooling added:

$$\dot{m}_{m_j} = \dot{m}_{g_j} + \dot{m}_{c_j} \tag{5.7}$$

The mixing layer Mach number for each successive cooling row can be calculated from the total pressure loss and the blade pressure distribution. The mainstream, mixing layers, boundary layers, and trailing edge injection all mix out at the trailing edge plane. The details of the trailing edge mixing model are outlined in Appendix C.

5.2.3 Meanline Velocity Triangle Model

As discussed in Chapter 2 the turbine operating point is controlled by setting the turbine corrected speed and the total-to-total pressure ratio across the turbine. For a given stage geometry, the vane performance is generally characterized by vane exit isentropic Mach number, and Reynolds number. The blade performance is characterized by its incidence angle, exit isentropic Mach number, and Reynolds number. In order to build a model of the turbine performance it is necessary to relate the turbine pressure ratio and corrected speed to the vane and blade exit Mach numbers and incidence angle. This can be accomplished using a one-dimensional model based on the meanline stage velocity triangles as depicted in Figure 5-9. The subscripts

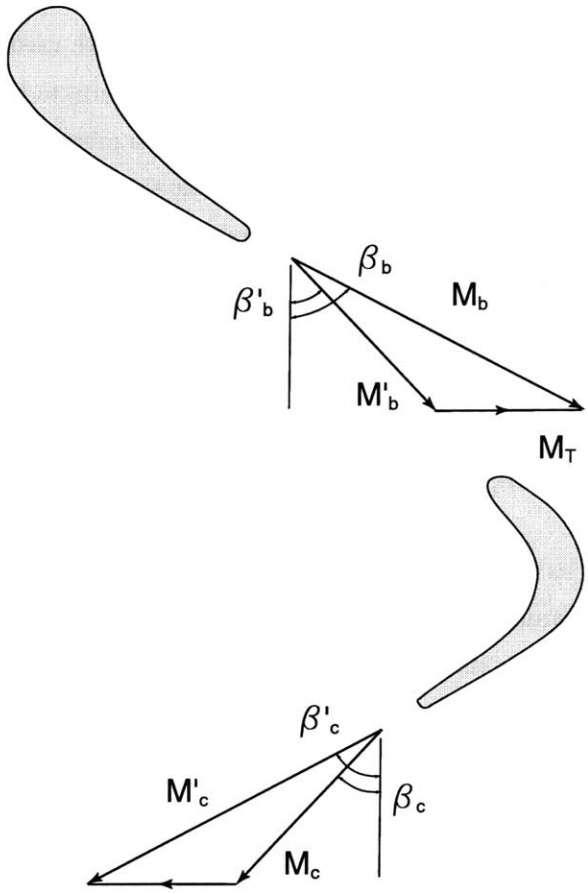

Figure 5-9: Film-Cooled Velocity Triangles.

a, b, and c denote the vane inlet, vane exit, and rotor exit quantities, b' and c' denote the rotor relative rotor inlet and outlet quantities, n and r denote NGV and rotor quantities. To calculate the stage velocity triangles, the rotor corrected speed is specified and a vane isentropic exit Mach number is assumed. The vane cooling mass flow distribution is then calculated using the vane surface static pressure distributions from MISES. The vane exit Mach number and total temperature are then calculated using the mixing-layer

model and trailing edge loss models described in Section 5.2.2. The rotor corrected speed and tangential Mach number are:

$$N_c = \frac{\Omega L_{ref}}{\sqrt{\gamma R T_{t_a}}}$$

$$M_T = N_c \left(\frac{r_b}{L_{ref}}\right) \left(\frac{1+\tilde{m}_n \tilde{T}_{tn}}{1+\tilde{m}_n}\right)^{-\frac{1}{2}} \left(1+\frac{\gamma-1}{2}M_b^2\right)^{\frac{1}{2}} \tag{5.8}$$

The corrected speed is normalized by the inlet critical velocity, whereas the M_T is the rotor velocity normalized by the rotor inlet speed of sound. $\tilde{m}_n$ is the ratio of vane coolant mass flow to the stage inlet mass flow and $\tilde{T}_{tn}$ is the ratio of vane total inlet temperature to the stage total inlet temperature. The second term in Equation 5.8 relates meanline radius to reference length used to define the corrected speed of the turbine. The third term relates mixed out vane exit temperature to the stage inlet temperature, on which the corrected speed is based. The vane coolant reduces the mixed out vane exit temperature. The final term converts the vane exit total temperature to the static temperature, on which the rotor tangential Mach number is based. The rotor relative inlet Mach number, and flow angle are then calculated:

$$\beta_b = \tan^{-1}\left(\frac{sin\,(\beta_b) - \frac{M_T}{M_b}}{cos\,(\beta_b)}\right)$$

$$M_b' = \sqrt{(M_b cos\beta_b)^2 + (M_b cos\beta_b - M_T)^2}$$

The rotor relative isentropic exit Mach number is estimated from the change in relative flow areas and the coolant mass flow and temperature added in the rotor. As an approximation, it is assumed that the coolant total pressure after injection equals the freestream total pressure. Using this approximation the isentropic exit Mach number can be calculated by using the corrected mass flow relation to match the rotor inlet and exit total pressures:

$$\frac{\dot{m}_b\sqrt{RT'_{t_b}}}{A_b F\,(M_b)} = P_{t_b} = \frac{\dot{m}_c\sqrt{RT'_{t_c}}}{A_c F\,(M_b)}$$

$$\frac{F\,(M_c)}{F\,(M_b)} = \frac{\dot{m}_c}{\dot{m}_b}\sqrt{\frac{T'_{t_c}}{T'_{t_b}}}\frac{A_b}{A_c} = \frac{\dot{m}_c}{\dot{m}_b}\sqrt{\frac{T'_{t_c}}{T'_{t_b}}}\frac{\cos\beta'_b}{\cos\beta'_c} \tag{5.9}$$

$$M'_c = M'_b\frac{\dot{m}_c}{\dot{m}_b}\sqrt{\frac{T'_{t_c}}{T'_{t_b}}}\frac{\cos\beta'_b}{\cos\beta'_c}\left(\frac{1+\frac{\gamma-1}{2}M'^2_c}{1+\frac{\gamma-1}{2}M'^2_b}\right)^{\frac{\gamma+1}{2(\gamma-1)}}$$

Equation (5.9) can be solved iteratively to find M'_c. The ratio of rotor inlet mass flow to exit mass flow can be expressed in terms of the vane and blade mass flow ratios:

$$\frac{\dot{m}_c}{\dot{m}_b} = \left(\frac{1+\tilde{m}_n+\tilde{m}_r}{1+\tilde{m}_n}\right)$$

The blade exit temperature is estimated from the inlet flows:

$$(\dot{m}_a + \dot{m}_n + \dot{m}_r)\, T'_{t_c} = \dot{m}_a T'_{t_a} + \dot{m}_n T'_{t_n} + \dot{m}_r T'_{t_r}$$

This expression can be manipulated to yield:

$$\frac{T'_{t_c}}{T'_{t_b}} = \frac{1+\tilde{m}_n}{1+\tilde{m}_n+\tilde{m}_r}\left(\frac{1+\tilde{m}_n\tilde{T}'_{t_n}+\tilde{m}_r\tilde{T}'_{t_r}}{1+\tilde{m}_n\tilde{T}'_{t_n}}\right)$$

$\tilde{T}'_{t_n}$ is the rotor relative vane coolant temperature normalized by the stage rotor relative inlet temperature, (which equals $\tilde{T}_{t_n}$). $\tilde{T}'_{t_r}$ is the rotor relative blade coolant temperature normalized by the stage rotor relative inlet temperature. The blade coolant temperature approximately equals the metal temperature because of the high internal heat transfer rates in the blade cooling plenum.

$$\tilde{T}'_{t_r} \approx \frac{T_m}{T'_{t_a}} = \frac{T_m}{T_{t_a}}\left(\frac{1+\frac{\gamma-1}{2}M_b^2}{1+\frac{\gamma-1}{2}M_b'^2}\right)$$

The blade exit Mach number then be calculated.

The Euler turbine equation, which relates the change in total temperature to the change in angular momentum across the rotor, is then used to calculate isentropic temperature drop across the rotor.

$$\tau_{is} = 1 - \frac{\gamma-1}{1+\frac{\gamma-1}{2}M_{b1}^2}M_T^2\left(\frac{M_{b1}}{M_T}sin\beta_b + \left(\frac{r_c}{r_b}\frac{M_c}{M_T}\left(\frac{1+\frac{\gamma-1}{2}M_c^2}{1+\frac{\gamma-1}{2}M_b^2}\right)^{\frac{1}{2}}sin\beta_c - \left(\frac{r_c}{r_b}\right)^2\right)\right)$$

The rotor pressure ratio can be calculated from the isentropic relation:

$$\pi_{is} = \tau_{is}^{\frac{\gamma}{\gamma-1}}$$

The overall stage pressure ratio is then calculated by including the vane pressure loss.

$$\pi = \pi_{is}\left(1-\zeta_n\frac{\gamma}{2}M_b^2\right)^{-1}$$

The vane isentropic exit Mach number is then iterated to find the velocity triangles for the desired stage pressure ratio. The stage isentropic efficiency can then be calculated from the vane and blade loss coefficients.

The stage isentropic efficiency is defined as the ratio of the actual to ideal enthalpy drop across the turbine stage:

$$\eta_{is} = \frac{\sum_{j=1}^{n} \dot{m}_j T_{t\,j} \left(1 - e^{\left(\frac{\Delta s_{pr}}{c_p}\right)} \pi_j^{\frac{\gamma-1}{\gamma}}\right)}{\sum_{j=1}^{n} \dot{m}_j T_{t\,j} \left(1 - \pi_j^{\frac{\gamma-1}{\gamma}}\right)}$$

The relevant unit process entropy change for the *unmixed isentropic efficiency* is defined as:

$$\frac{\Delta s_{pr}}{c_p} = -\frac{\gamma - 1}{\gamma} ln\left(1 + \frac{\Delta P_t}{P_{t\,j}}\right)$$

The entropy generated can be estimated from the vane and blade entropy loss coefficents:

$$\zeta_n = \frac{T_{s\,b} \Delta s_{pr\,n}}{h_{t\,b} - h_b} = \frac{T_{s\,b} \Delta s_{pr\,n}}{\frac{1}{2} V_b^2}$$

$$\begin{aligned} \Delta s_{pr\,n} &= \frac{\zeta_n \frac{1}{2} V_b^2}{T_{s_b}} = \frac{\zeta_n \frac{1}{2} M_b^2 \gamma R T_{s_b}}{T_{s_b}} \\ &= \zeta_n \frac{\gamma}{2} M_b^2 R \end{aligned}$$

The total entropy generation for the mainstream flowpath is the sum of the vane and blade entropy generation rates:

$$\frac{\Delta s_{pr}}{c_p} = \frac{\gamma - 1}{2} \left(\zeta_n M_b^2 + \zeta_r M_c'^2\right)$$

If the vane and blade loss characteristics are known, the meanline velocity triangle can be used to analytically estimate the turbine stage efficiency. Section presents the characterization of the vane and blade loss.

5.3 Loss Predictions

This Section describes how a combination of MISES and published loss correlations were used to estimate the loss characteristics for the nozzle guide vane and rotor blade rows. An additional base pressure loss was added to the airfoil boundary layer and shock losses calculated using MISES to account for von Karman type vortex shedding off the blunt trailing edges that is not modeled by MISES. An endwall loss correlation proposed by Sharma and Butler(1987) uses the profile boundary layers to estimate the loss due to the endwall boundary layers and secondary flow.

5.3.1 Profile Losses

The vane and blade profile losses were calculated using MISES over a range of exit Mach numbers and incidence angles. The computed vane surface isentropic Mach number distributions are compared with those measurements by Osnaghi[18] in Figure 5-5. Given the close agreement between the computed and measured pressure distributions it can be assumed that the boundary layer losses are accurately predicted. The vane and blade profile loss characteristics as a function of exit Mach number are shown in Figures 5-10 and 5-11. The blade loss characteristics as a function of incidence angle are shown in Figure 5-12.

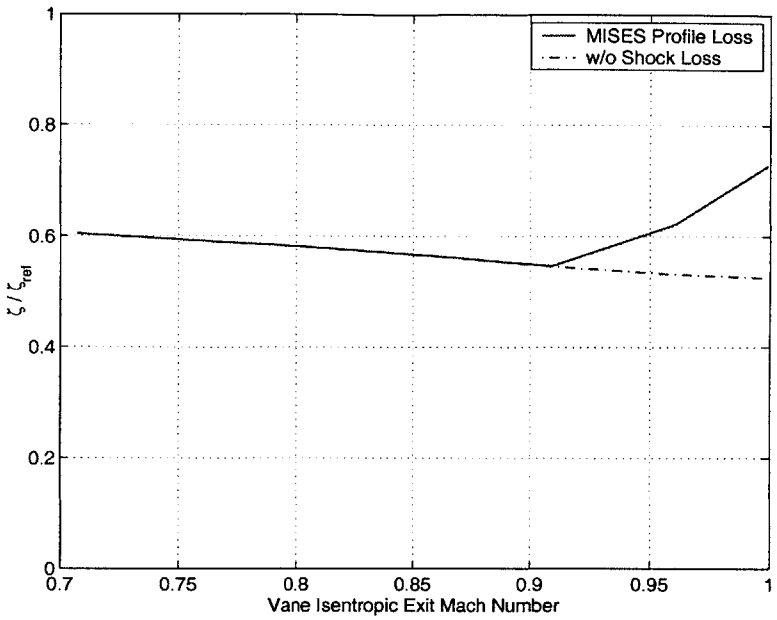

Figure 5-10: Vane Entropy Loss Coefficent vs. Isentropic Exit Mach Number

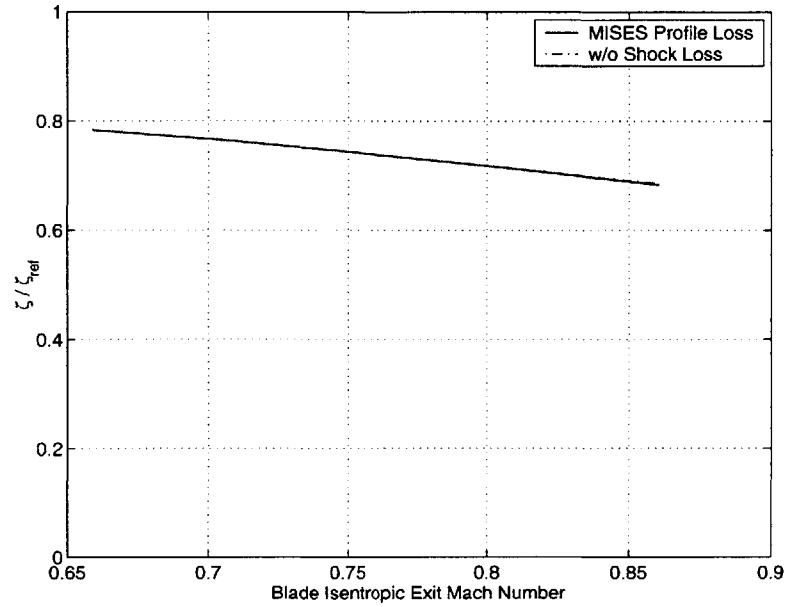

Figure 5-11: Blade Entropy Loss Coefficent vs. Isentropic Exit Mach Number

The loss characteristics shown in Figures 5-10 to 5-12 include boundary layer loss, shock loss, and the loss due to the blockage caused by the blunt trailing edges of the vane and blade. MISES uses a blunt trailing edge correlation as described by Drela [6] to estimate the loss associated with the additional blockage. However, because of vortex shedding (not modeled by MISES) the pressure acting on the blunt trailing edge is usually below the free-stream pressure by an amount that may be defined in terms of the base pressure coefficient, C_{pb}:

$$C_{pb} = (P_b - P_{ref}) \,/\, \left(\frac{1}{2}\rho V_{ref}^2\right) \tag{5.10}$$

P_{ref} and V_{ref} are generally defined as pressure and velocity immediately before the trailing edge, and P_b is the base pressure. Typical values for C_{pb} are in the range -0.1 to -0.2, although the value varies greatly with the state of the boundary layer, shape of the trailing edge, and the ratio of trailing edge thickness to boundary layer thickness Denton [4].

Denton used a simplified incompressible trailing edge loss model to derive the following expression for the profile entropy loss coefficient [6]:

$$\zeta = -\frac{C_{pb}t}{w} + \frac{2\theta}{w} + \left(\frac{\delta^* + t}{w}\right)^2 \tag{5.11}$$

Equation (5.11) shows the contribution of the base pressure coefficient term relative to momentum thickness

[6]To derive this expression Denton assumed that the deviation angle downstream of the trailing edge was zero. This reduces the problem to a 1D analysis. For thick trailing edges the predicted loss is significantly higher than of a 2D analysis (Stewart).

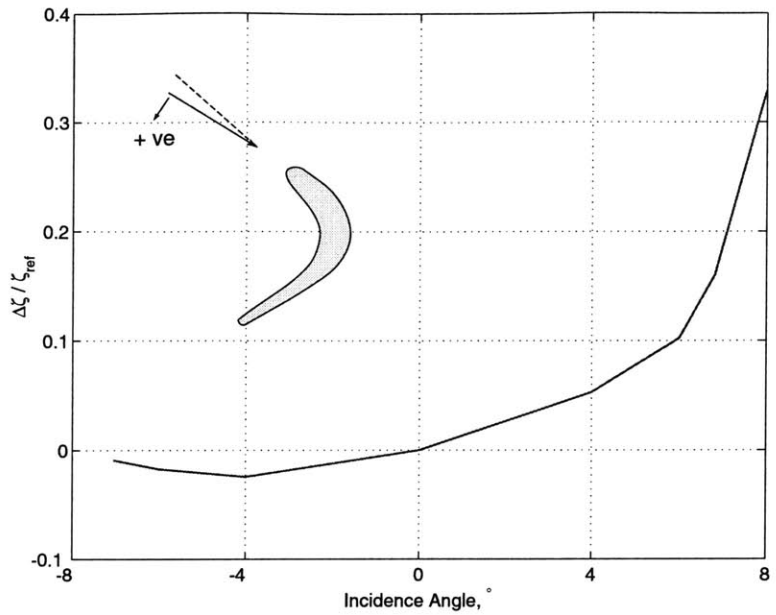

Figure 5-12: Blade Entropy Loss Coefficent vs. Incidence Angle

and the trailing edge thickness. For trailing edge thicknesses ($\frac{t}{w}$) of 10% a typical value for C_{pb} of -0.15 will result in a loss contribution that is of the same order as the entire profile loss shown in Figure 5-10. Equation (5.11) indicated that for incompressible flows the additional loss due to the base pressure coefficient can be superimposed onto the MISES losses to estimate the overall profile loss. It is important to verify that additional base pressure loss can be superimposed in a range when the flow cannot be considered to be incompressible. Figure 5-13 shows the total profile losses for three values of base pressure coefficient (-.10, -.15 and -.20) from Stewart's (1955) trailing edge loss model. The results show that the additional loss due to the additonal base pressure term is independent of vane exit Mach number and verify that the loss can be superimposed on the other profile losses. Also, Figure 5-13 serves to illustrate the range of uncertainty associated with the additional base pressure loss.

Figures 5-14 and 5-15 show the vane and blade profile loss coefficients as a function of isentropic exit Mach number, assuming a typical value for C_{pb} of -0.15. Figure 5-14 also shows the measured midspan loss for this vane as measured by Osnaghi[18]. The measured and estimated vane loss characteristics are similar for isentropic exit Mach numbers in the range 0.84 to 0.95.

5.3.2 Endwall Losses

Endwall losses cannot generally be estimated with the same level of confidence as profile losses. After reviewing the various correlations for endwall flows, Horlock [9] concluded that there was little agreement between them. More recently, Sharma and Butler[21] presented a simple physical model of the endwall boundary layers. The effect of cross flow-induced three dimensionality of the boundary layer is modeled as an extra rate of strain that modifies the boundary layer skin friction relationship. The magnitude of the

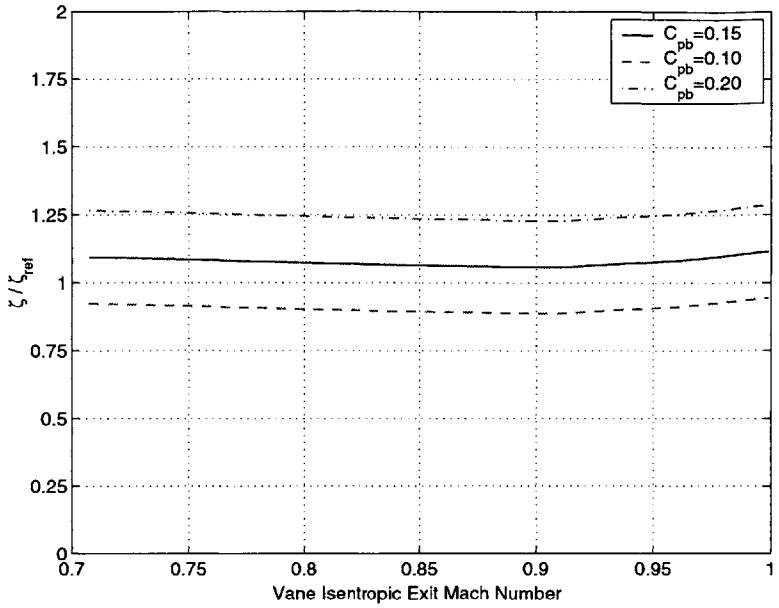

Figure 5-13: Effect of C_{pb} on Blade Entropy Loss Coefficient

extra rate of strain was selected to correlate the results from eight experimental data sets. In their study, the predicted and measured total losses matched within ± 10 % using their semi-analytic correlation. The resulting expression for endwall loss energy loss coefficient is:

$$\zeta_{ew} = \zeta_{2D} \frac{S cos\beta - t}{h} \left(1 + 4 \frac{\epsilon}{\sqrt{CR}}\right) \tag{5.12}$$

S, t, and h are the pitch, trailing edge thickness, and blade height, ϵ and CR are the total blade turning, and convergence ratio ($= \rho_2 U_2 / \rho_1 U_1$). β is the gas exit angle measured from the axial and ζ_{2D} is the two dimensional energy loss coefficient. The correlation nomenclature was changed to be consistent with the conventions used in this thesis.

Figure 5-14 presents a summary of the vane loss characterization. The total profile loss is the sum of the profile loss predicted using MISES and the additional loss to model the reduced base pressure due to vortex shedding behind the blunt trailing edge of the vane. The total profile loss can be compared to the midspan loss measured by Osnaghi for this vane geometry. For vane isentropic exit Mach numbers between 0.85 and 1.0 the total profile and the measured midspan loss agree. Figure 5-14 also shows the combined profile and endwall loss.

Figure 5-15 presents a summary of the blade loss characterization. The total profile loss prediction is compared with the measured midspan loss (supplied by the program sponsor). The measured midspan loss is significantly higher than the calculated total profile loss at low blade exit Mach numbers, but agrees well at high blade exit Mach numbers. The MISES results predicted a pressure surface separation near

the leading edge. It is believed that the increased midspan loss results from increased mixing due to the unsteady shear layer that results from this pressure surface separation. This increased loss is not modeled by MISES. Two total loss characteristics are presented in Figure 5-15. The first is based on the measured midspan loss and the calculated endwall loss. The second is based on the calculated profile and endwall loss. As shown in the following section, the first of these two loss characteristics was found to be more consistent with the measured baseline data.

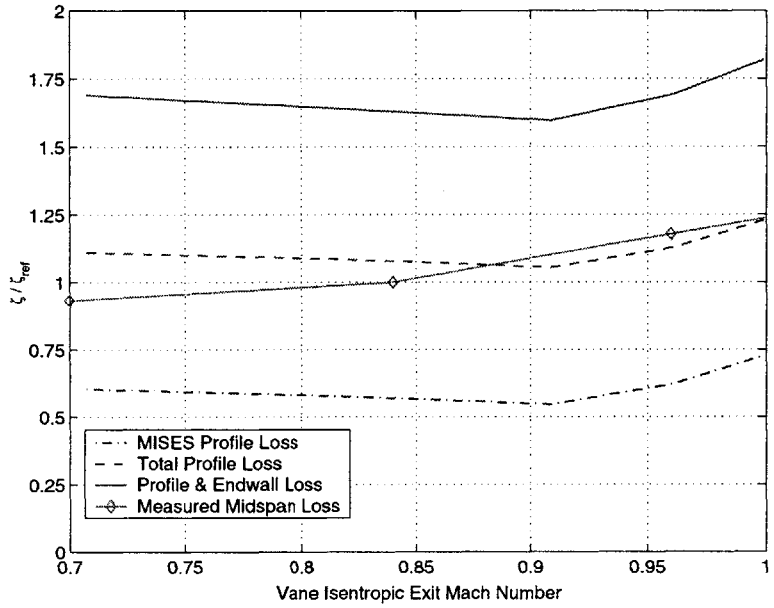

Figure 5-14: Vane Entropy Loss Coefficent - Profile and Endwall

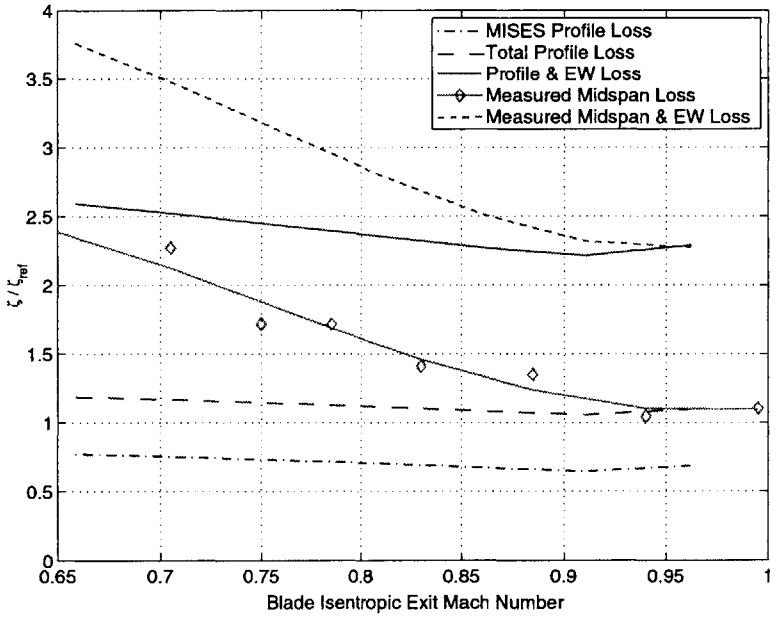

Figure 5-15: Blade Entropy Loss Coefficent - Profile and Endwall

5.4 Results

The purpose of the mixing models outlined in Section 5.2.2 is to estimate loss and the increased mainstream Mach number associated with the injection of coolant into the mainstream flow path. This model can be used to estimate the change in the turbine stage mass flow as a function of operating point, coolant mass flow and temperature. The results obtained using this model will be compared with the corrected mass flow measured for baseline and film-cooled tests. Predictions using the turbine loss model (described in Section 5.3) will be compared with the baseline turbine stage isentropic efficiency measurements from Chapter 3. These two comparisons will serve as a calibration of the meanline velocity triangle model. The mixing model used to estimate the stage mass flow will be re-examined to emphasize assumptions required to predict the experimental results. The model will then be used to estimate the change in vane and blade profile and endwall losses that result from film-cooling and trailing-edge enjection.

5.4.1 Corrected Mass Flow

The mass flow measurements, from the baseline and film-cooled experiments, are presented as a normalized corrected mass flow per unit area. For these tests the corrected mass flow per unit area is defined as:

$$Wc = \frac{\dot{m}_c \sqrt{RT_{t\,a}}}{P_{t\,a} A_{ref}} \tag{5.13}$$

Unless otherwise specified, the $\dot{m}$ is the turbine stage exit mass flow. $T_{t\,a}$ and $P_{t\,a}$ are the total inlet temperature and pressure, and R is the gas constant of the test gas. The corrected mass flow data presented in Chapter 3 is normalized by the design point value for the baseline turbine stage. Although technically a normalized corrected mass flow per unit area, it is referred to as the corrected mass flow in this thesis.

For the turbine stage model the corrected mass flow per unit area is defined in terms of the throat Mach number:

$$Wc = \frac{M\sqrt{\gamma}}{\left(1 + \frac{\gamma-1}{2} M^2\right)^{\frac{\gamma+1}{2(\gamma-1)}}} \tag{5.14}$$

The ratio of corrected mass flow per unit area to the baseline design point corrected mass flow per unit area is:

$$Wc^* = Wc \frac{A_{th}{}'}{A_{th}} \left(1 - \Delta\delta_{ps} - \Delta\delta_{ss}\right)\left(1 + \tilde{m}\right) \tag{5.15}$$

$\frac{A_{th}{}'}{A_{th}}$ is the ratio of film-cooled to baseline flow area, which accounts for the reduction in flow area due

to film-cooling induced leading-edge transiton. $\Delta\delta_{ps}$ and $\Delta\delta_{ss}$ represent the displacement of the freestream due to changes in the mixing layer thickness at the throat. $\tilde{m}$ is the ratio of coolant flow to stage inlet mass flow. For the turbine stage model Equation 5.15 is the equivalent of the measured quantity defined by Equation 5.13.

Figures 5-16(a) and 5-16(b) show the measured trends for corrected mass flow for the baseline turbine stage and the trends predicted by the velocity triangle model. Both of these Figures show that the model captures the measured trends for corrected mass flow. The measured corrected mass flow is normalized by the design operating point corrected mass flow. [7]: As the model and experimental results are normalized by different values the close agreement between the measured and predicted does not indicate an ability to accurately predict the corrected mass flow. The comparison does indicate that the model captures the measured trend for the variation of corrected mass flow with both corrected speed and pressure ratio. The close agreement between the predicted and measured data trends suggests that the stage velocity triangle model provides a reasonable estimate of the stage meanline Mach numbers for the baseline experiment.

Figure 5-17 shows a comparison of the predicted and measured corrected mass flows for a range of coolant flows for the film-cooled experiment. The results for the two coolant-to-mainstream temperature ratios are shown. For coolant mass flows close to the design point, the model predicts the increase of overall stage corrected mass flow with coolant-to-mainstream mass flow ratio within the repeatability of the measurements. The the model also predicts the reduction in the stage corrected mass flow for the low coolant-to-mainstream temperature ratio tests within the repeatability of the measurements. Figures 5-18(a) and 5-18(b) compare the measured and predicted trends for the variation of corrected mass flow with corrected speed and pressure ratio. The model captures the measured trend for the variation of corrected mass flow with both corrected speed and pressure ratio within the repeatability of the measurements.

[7]Pressure ratio 2.0 and 100% corrected speed.

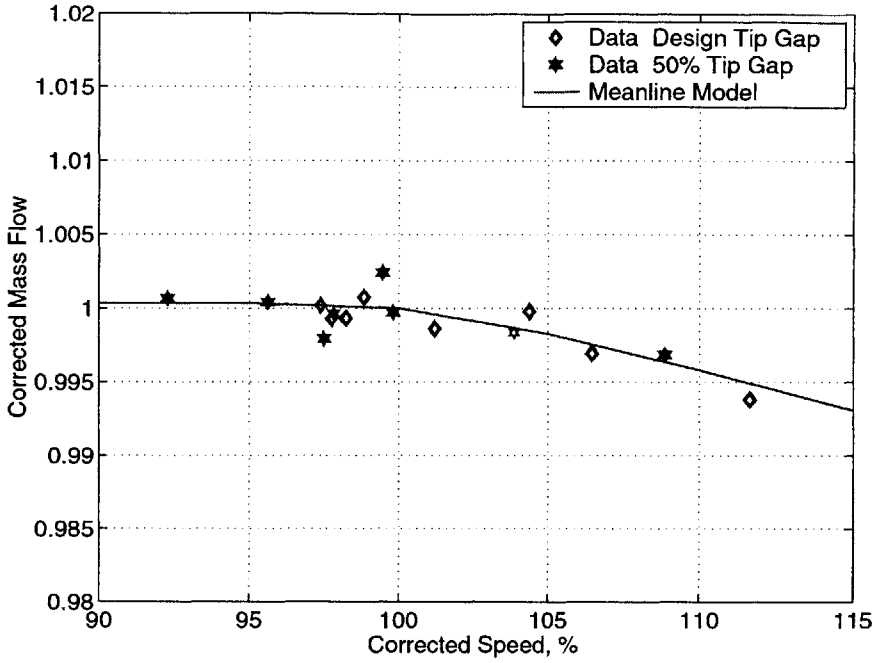

(a) Measured and Turbine Stage Model Wc vs. N_c

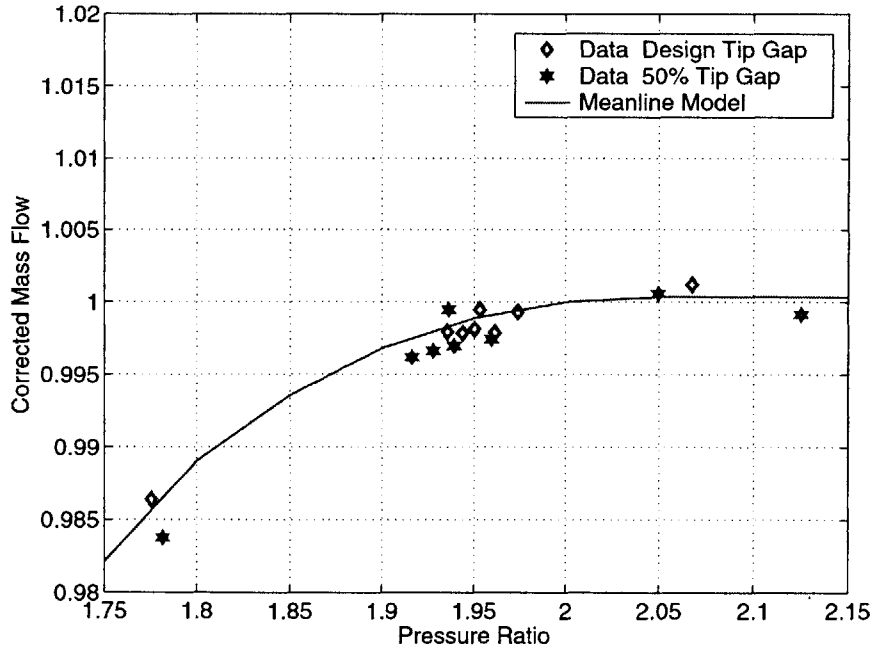

(b) Measured and Turbine Stage Model Wc vs. π

Figure 5-16: Baseline Corrected Mass Flow vs. Turbine Stage Model

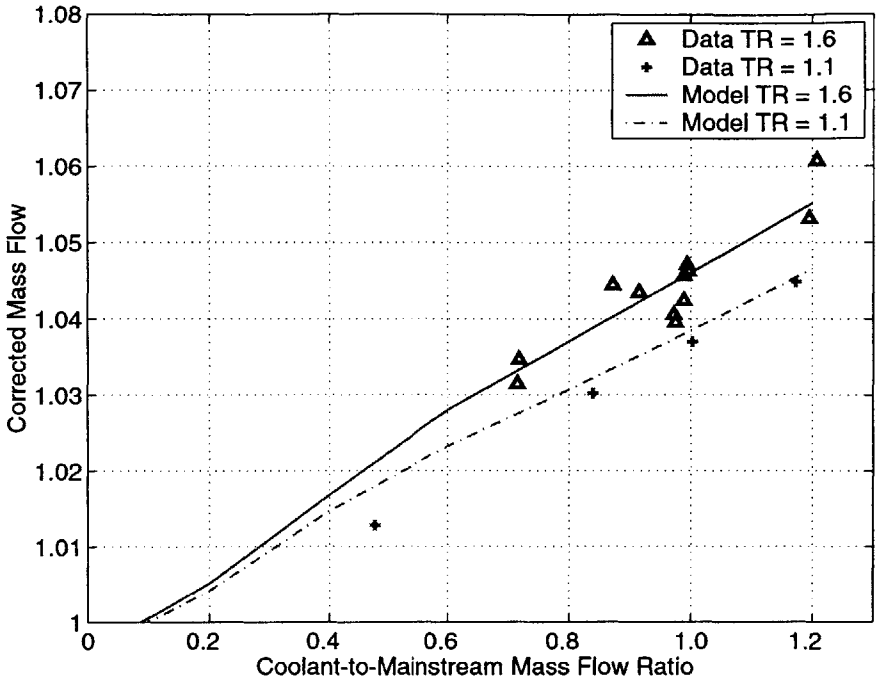

Figure 5-17: Measured and Turbine Stage Model Corrected Mass Flow vs. Coolant MFR

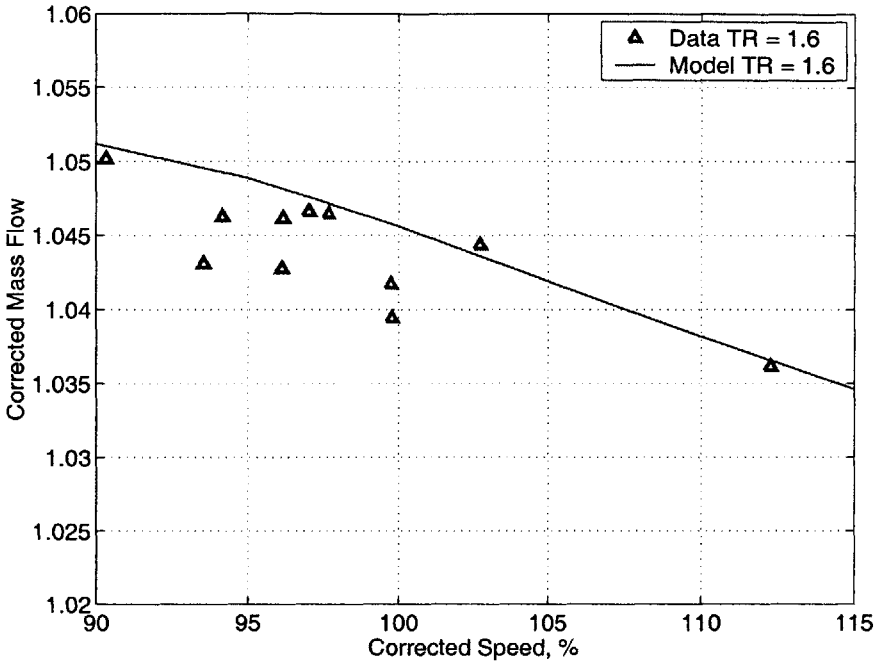

(a) Measured and Turbine Stage Model Corrected Mass Flow vs. N_c

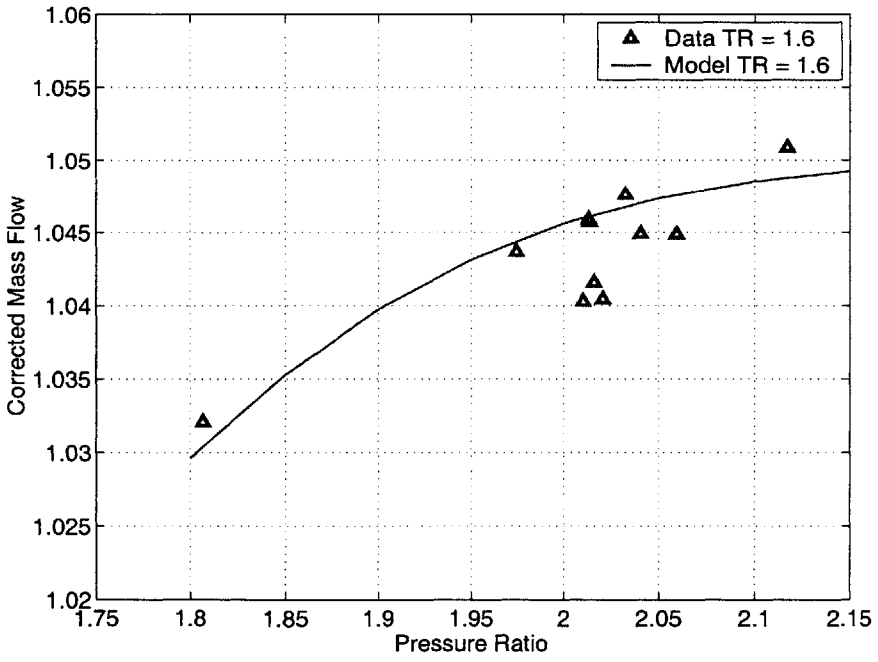

(b) Measured and Turbine Stage Model Corrected Mass Flow vs. π

Figure 5-18: Film-Cooled Corrected Mass Flow vs. Turbine Stage Model

To better appreciate the results and design implications of the coolant flow injection models presented in Section 5.2.2 it is worthwhile taking a step back and to use a simper approach to gain a better insight into the mixing process. It is particularly important to elucidate the impact of coolant injection on the vane exit Mach number. The model presented in Section 5.2.2 for the injection of coolant from the suction surface downstream of the throat is a constant area mixing model. Shapiro's [20] 'influence coefficient' method gives insight into the role of the various parameters in determining the effect of injection on the vane exit Mach number:

$$\frac{dM^2}{M^2} = \left(\frac{dw}{w} - \frac{dA}{A}\right) \frac{2\left(1+(1-y)\gamma M^2\right)\left(1+\frac{\gamma-1}{2}M^2\right)}{1-M^2} + \frac{dT_t}{T_t}\left(1+\frac{\gamma-1}{2}M^2\right)\left(1+\gamma M^2\right) \tag{5.16}$$

This approach conserves mass, streamwise momentum and energy for the mainstream and coolant streams. The trailing edge injection model presented in Section 5.2.2 is significantly different as it conserves mass, axial momentum, tangential momentum and energy. The axisymmetric swirling flow method developed by Heiser [2] gives insight into this process:

$$\begin{aligned}\frac{dM^2}{M^2}\left(1-M^2\sin^2\alpha\right) = &\left(\frac{dw}{w} - \frac{dA}{A}\right) 2\left(1+\frac{\gamma-1}{2}M^2\right)\sin^2\alpha \\ &+ \frac{dT_t}{T_t}\left(1+\frac{\gamma-1}{2}M^2\right)\left(\left(1+\gamma M^2\right)\sin^2\alpha - \cos^2\alpha\right) \\ &+ \frac{dw}{w}(1-y)\,2\left(1+\frac{\gamma-1}{2}M^2\right)\left(\gamma M^2\sin^4\alpha - \cos^2\alpha\left(1-\gamma M^2\sin^2\alpha\right)\right)\end{aligned} \tag{5.17}$$

$$d\alpha\left(1-M^2\sin^2\alpha\right) = \frac{1}{2}\sin 2\alpha \tag{5.18}$$

where, y is the coolant-to-mainstream velocity ratio and dw is the injected mass flow. Equations 5.16 shows that for one-dimensional injection, the denominator $1-M^2$, causes a large sensitivity to area changes and coolant injection for freestream Mach numbers close to unity. The equivalent Mach dependence in Equation 5.17 is $1-M^2\sin\alpha^2$, which at low values of α (high swirl) results in much lower sensitivity to freestream Mach mumber. Figure 5-20(a) shows the calculated downstream Mach number for a range of injection rates. Figure 5-20(b) shows the change in tangential Mach number for the same range of coolant flows. This simple example shows the profound difference between the two different types of mixing that occur downstream of the NGV throat. To examime the limits of these two mixing scenarios on the turbine stage performance two additional cases were examined. Case 1 refers to the film-cooled results shown in Figure 5-17. In Case 2 all of the cooling downstream of the throat is injected on the suction surface where the 1-D mixing model is used. In Case 3 all of the cooling downstream of the throat is injected at the trailing

edge where the trailing edge loss model is used (similar to the axisymmetric model). Figure 5-19 compares all three cases with the measured corrected mass flow. The procedure outlined in Section 5.2.2 that uses a combination of constant area mixing and axisymmetric mixing is most consistent with the measured data.

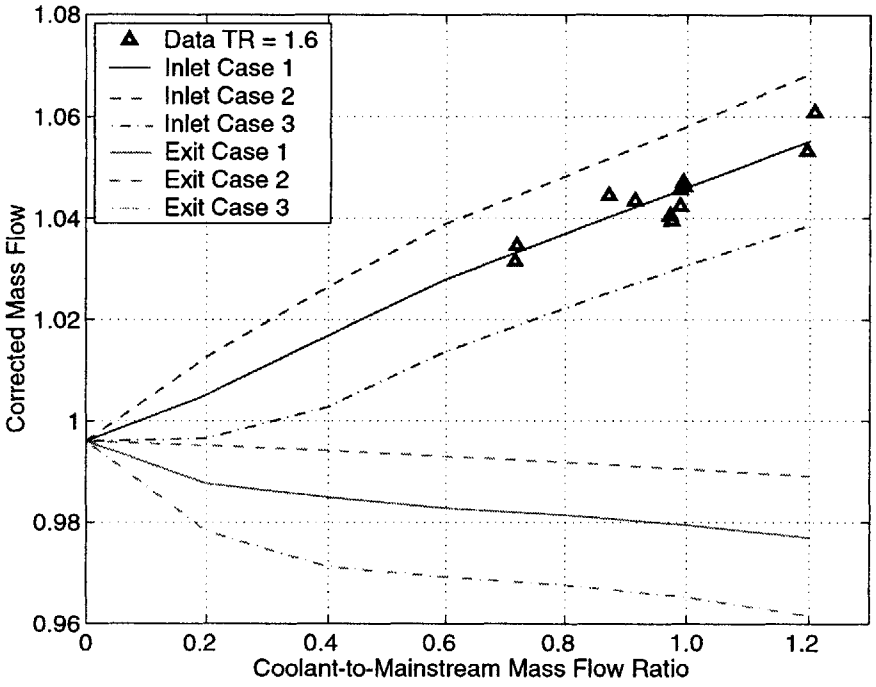

Figure 5-19: Turbine corrected mass flow with different mixing model assumptions

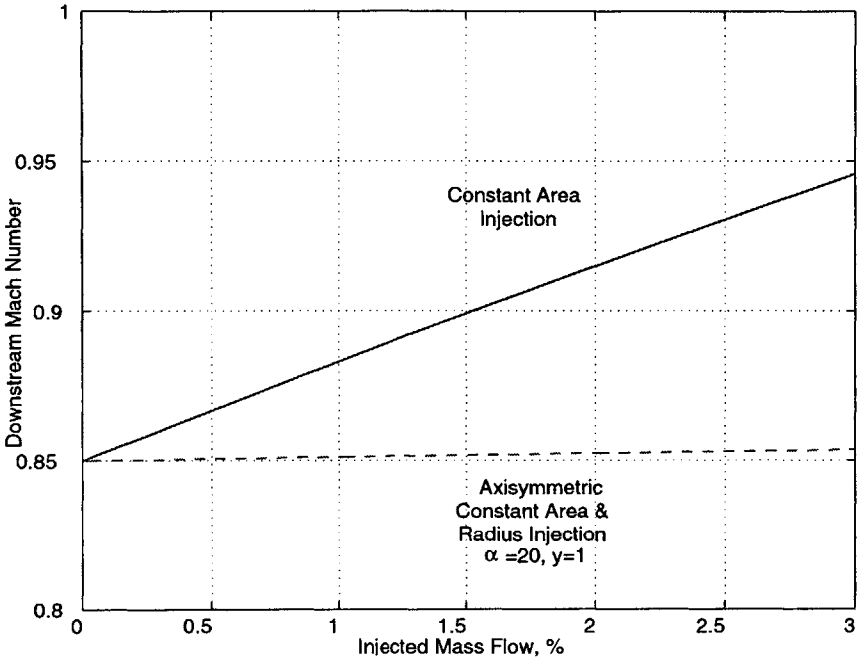

(a) Downstream Mach Number vs. Injected Mass Flow

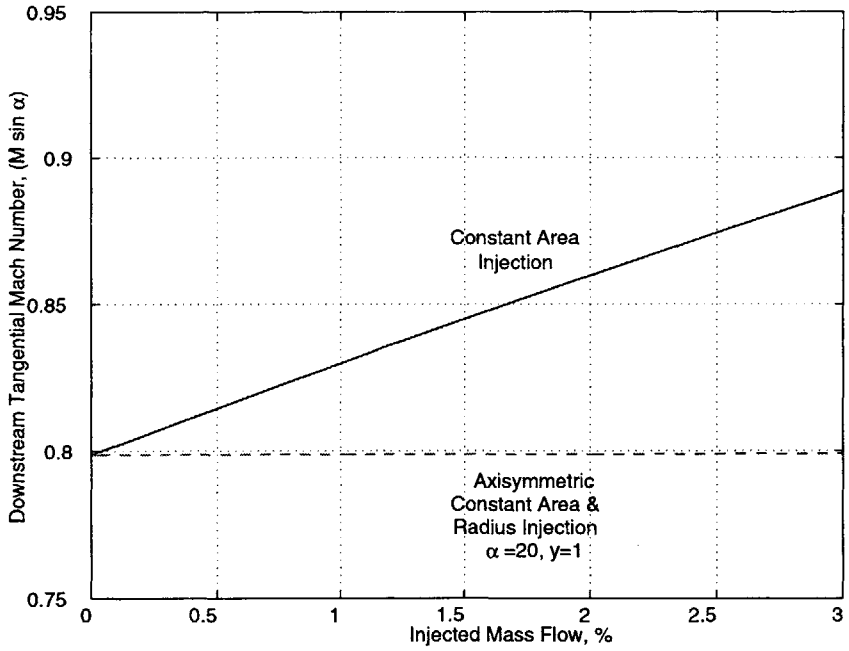

(b) Downstream Tangential Mach Number vs. Injected Mass Flow

Figure 5-20: Comparison of Axisymmetric vs. 1D Injection

5.4.2 Isentropic Efficiency

Figures 5-21(a) and 5-21(b) compare the model stage efficiency prediction with the measured data for a range of corrected speed and pressure ratio respectively. Figure 5-21(a) shows the extrapolated zero tip gap isentropic efficiency versus corrected speed. For corrected speeds in the range 95-110% the model shows a good agreement with the extrapolated trends based on the two tip gaps measured. Comparison of the model and data outside this range of corrected speed is suspect because the measured data for the two tip gaps do not overlap for the entire range of corrected speeds shown in the plot. The zero tip gap estimate is based on a linear extrapolation from the two measured tip gaps. This assumes that the tip gap loss is directly proportional to tip gap. The tip gap loss model developed by Martinez-Sanchez [14] predicts that the loss sensitivity increases as the tip gap is reduced. Increased sensitivity as the gap is reduced would bring the extrapolated data closer to the turbine stage model predicted efficiency. However, the goal of this comparison is to capture the measured trends in order to better understand the film-cooled results. Figure 5-21(a) shows the extrapolated zero tip gap isentropic efficiency versus pressure ratio. In this case the design tip gap measured trend is based on a more limited amount of data.

Figure 5-22 compares the measured change in efficiency for the film-cooled turbine stage (versus the coolant-to-mainstream mass flow ratio normalized by its design point value) and the change in efficiency of the turbine stage based on and profile and endwall losses alone. The difference between these represents the loss due to film-cooling for the film-cooled turbine stage. As the coolant-to-mainstream mass flow ratio is increased the stage reaction is also increased and the stage profile and endwall are reduced. Using the meanline velocity triangle model it was estimated that the efficiency of an uncooled turbine stage with the same velocity triangles and airfoil Mach number distributions as the film-cooled turbine would be 1.25% higher than that of the identical stage geometry tested without coolant. The primary mechanism for the reduction in loss is a lowering of the vane exit Mach number, which corresponds to an increase in the stage reaction.

5.5 Summary

The goal of this Chapter was to estimate the performance of a hypothetical ideal turbine stage that is capable of operating without cooling, in the same environment as the film-cooled turbine stage. In this way the change in turbine efficiency due to film-cooling can be estimated.

The nozzle guide vane and rotor blade row loss characteristics were estimated using a combination MISES and semi-empirical loss correlations. One-dimensional mixing models were used to estimate the effect of coolant injection on the mainstream Mach number and loss. A meanline velocity triangle model of the turbine stage was then used to relate the independent variables that specify the turbine operating point to the independent parameters used to characterize the vane and blade loss. These models were then calibrated against the baseline stage isentropic efficiency measurements and the measured mass flow for the

baseline and film-cooled tests.

The efficiency for an ideal turbine stage without any temperature limitations was estimated to be 3.0% higher than the film-cooled turbine stage at the design operating point. This results is a sensitivity to cooling flow rate of approximately 0.3% per 1% of coolant flow rate. The sensitivity to coolant flow rate increases as the coolant flow rate is increased. At the design point each additional 1% of coolant mass flow decreases the stage efficiency by 0.5%.

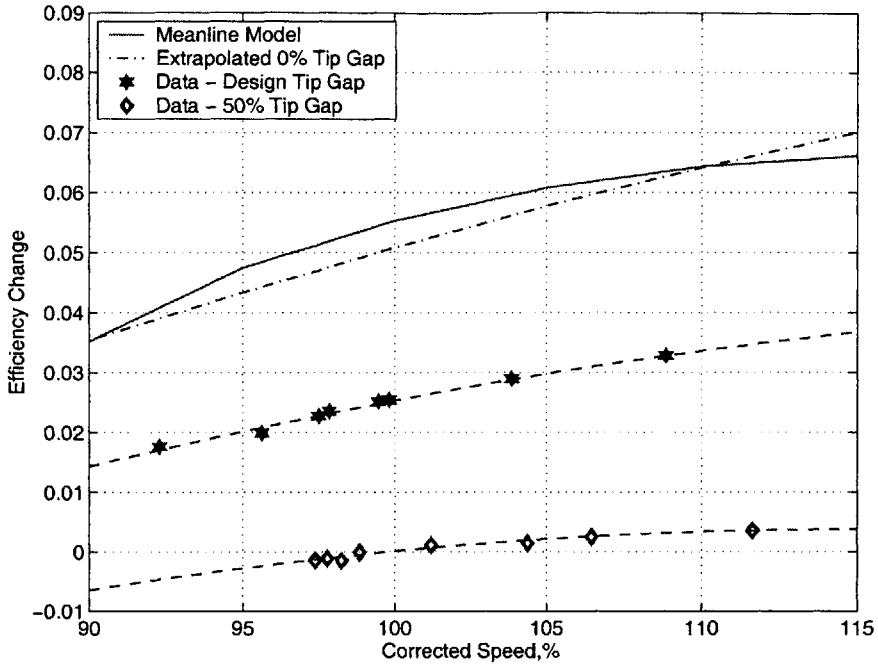

(a) Isentropic Efficiency vs. Corrected Speed

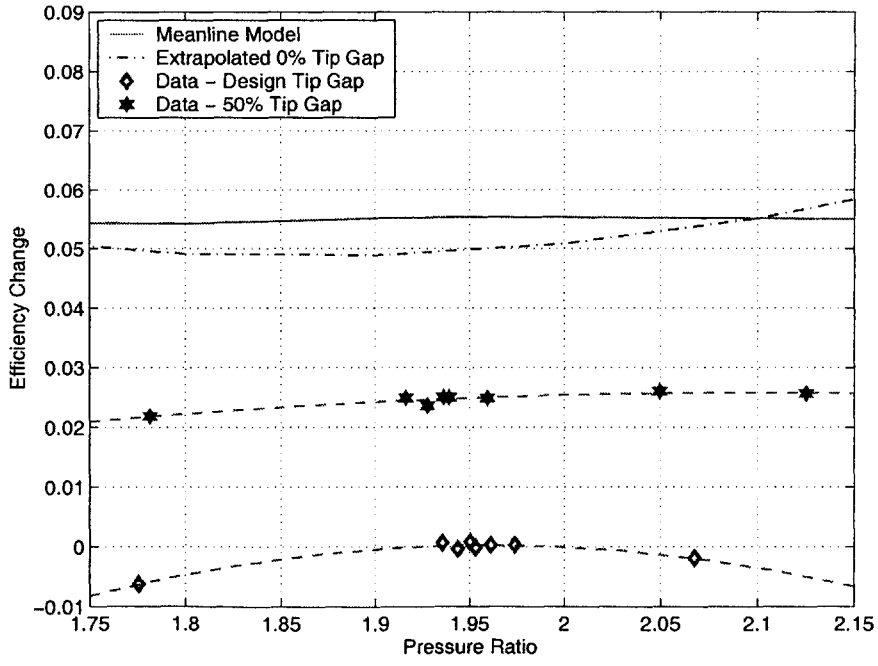

(b) Isentropic Efficiency vs. Pressure Ratio

Figure 5-21: Comparison of Turbine Stage Model and Measured Efficiency

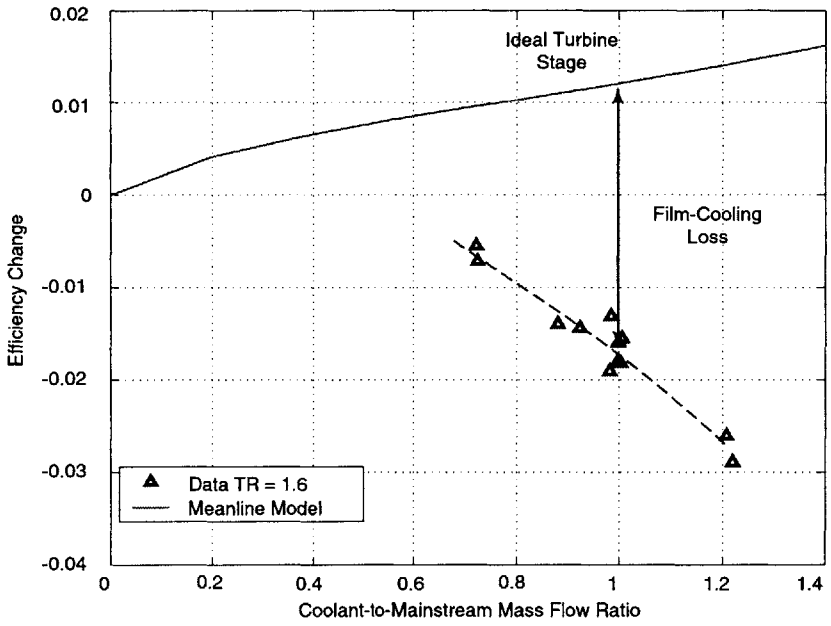

Figure 5-22: Comparison of Turbine Stage Model and Measured Efficiency

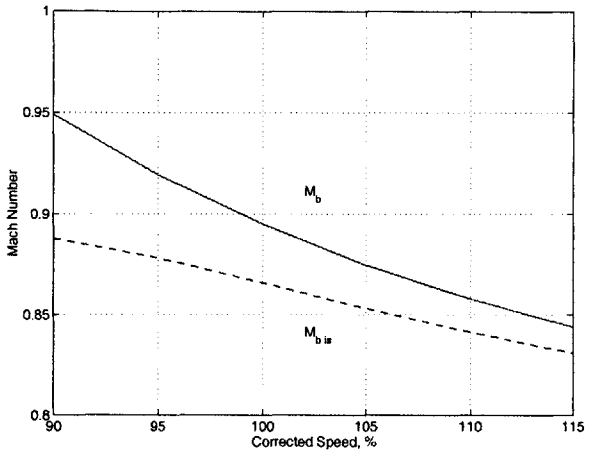

(a) Vane Exit Mach Number vs. N_c

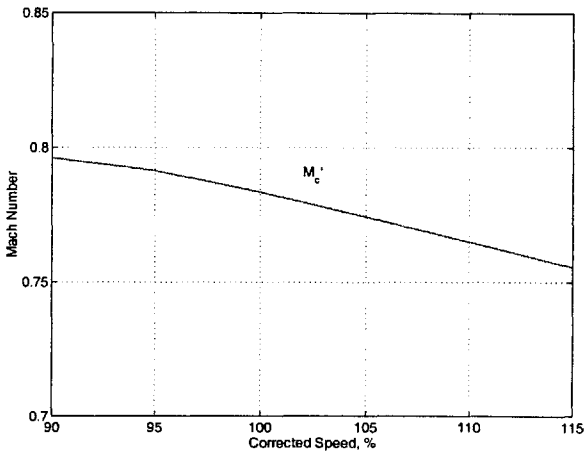

(b) Rotor Exit Mach Number vs. N_c

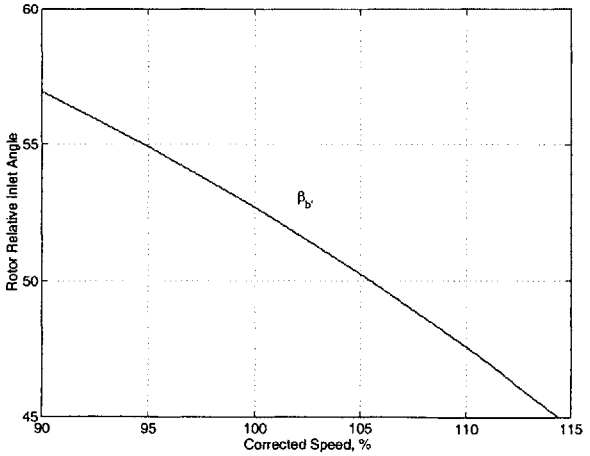

(c) β_b' vs. N_c

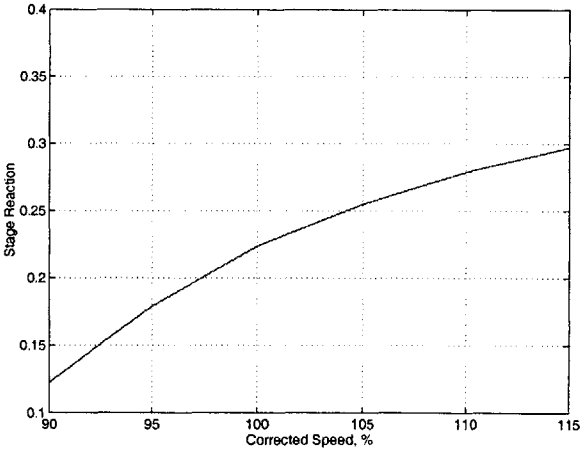

(d) Stage Reaction vs. N_c

Figure 5-23: Model Summary - Baseline Corrected Speed

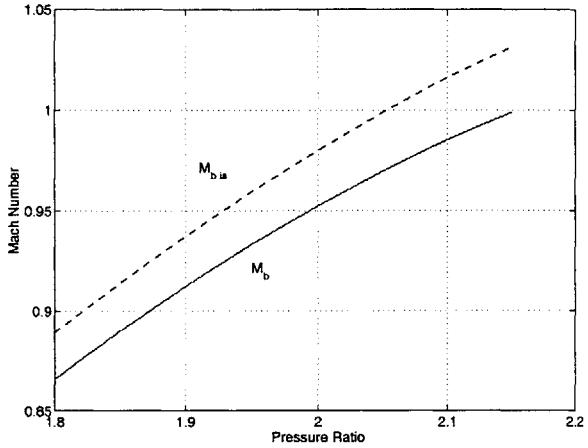

(a) Vane Exit Mach Number vs. π

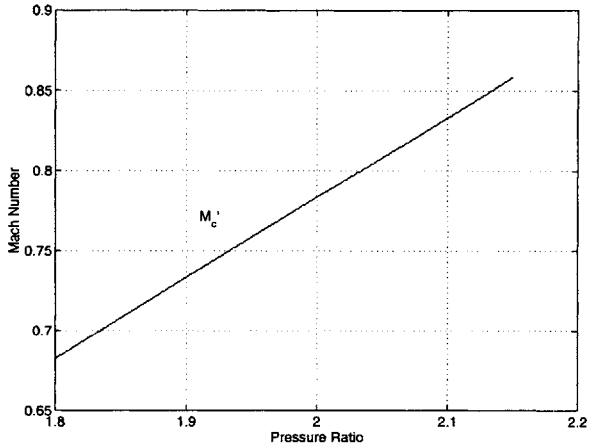

(b) Rotor Exit Mach Number vs. π

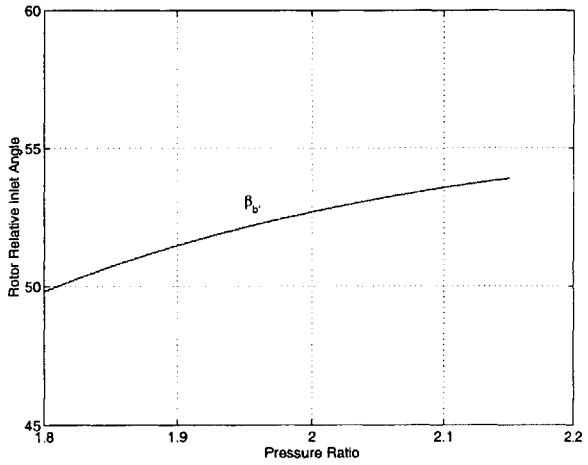

(c) β_b' vs. π

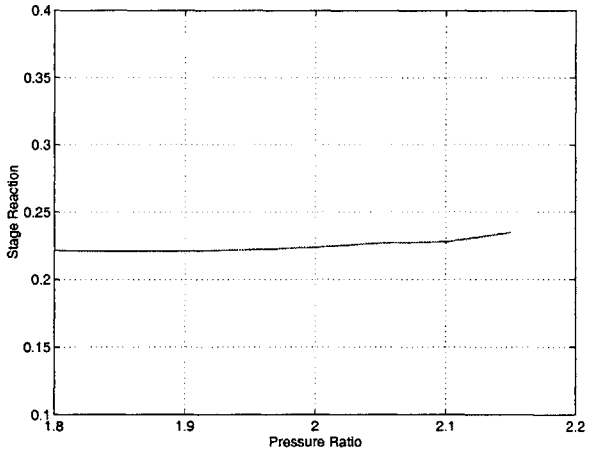

(d) Stage Reaction vs. π

Figure 5-24: Model Summary - Baseline Pressure Ratio

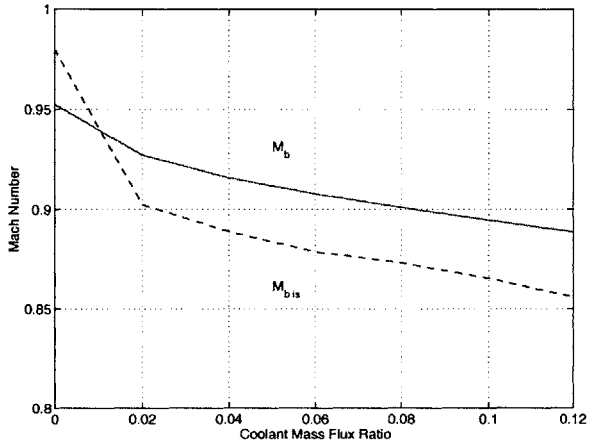

(a) Vane Exit Mach Number vs. Coolant MFR

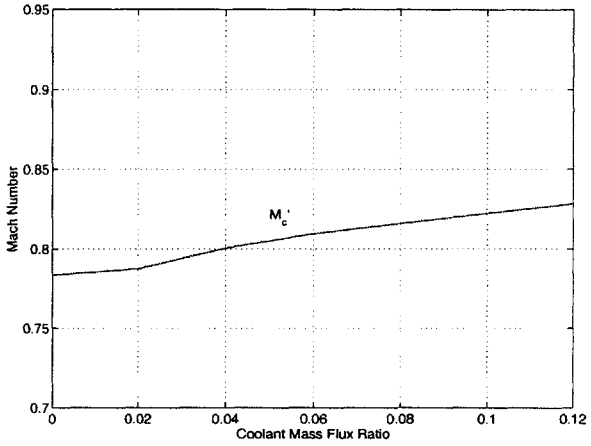

(b) Rotor Exit Mach Number vs. Coolant MFR

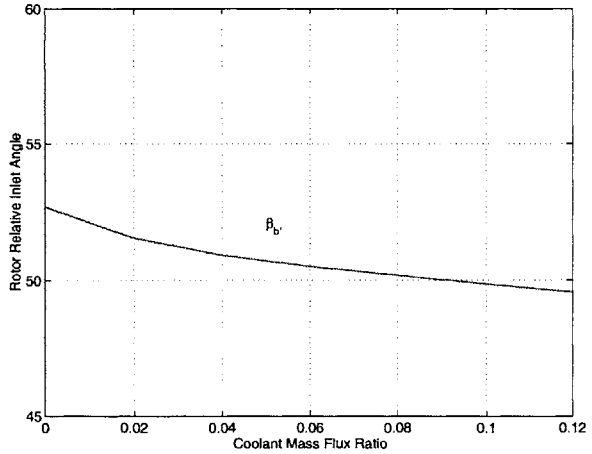

(c) β_b' vs. Coolant MFR

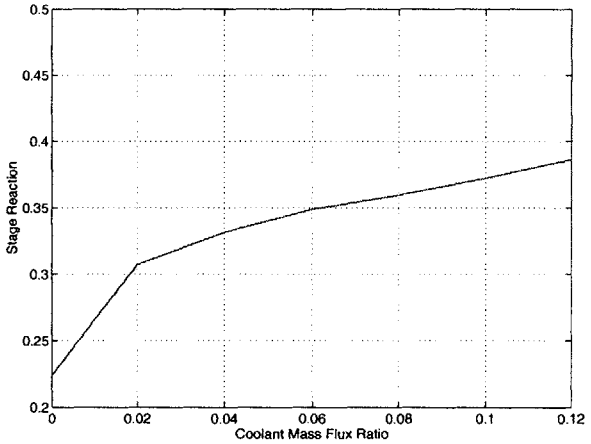

(d) Stage Reaction vs. Coolant MFR

Figure 5-25: Model Summary - Coolant

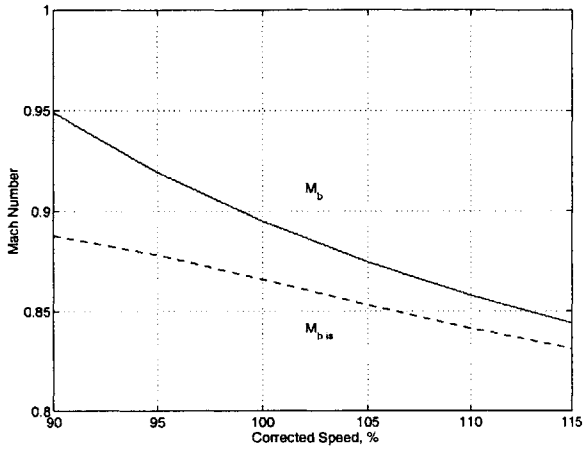

(a) Vane Exit Mach Number vs. N_c

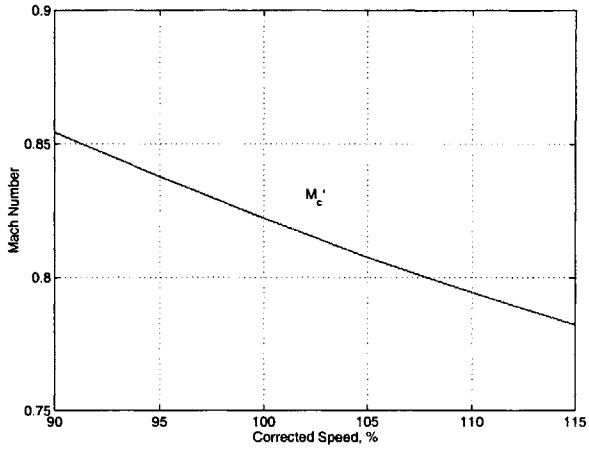

(b) Rotor Exit Mach Number vs. N_c

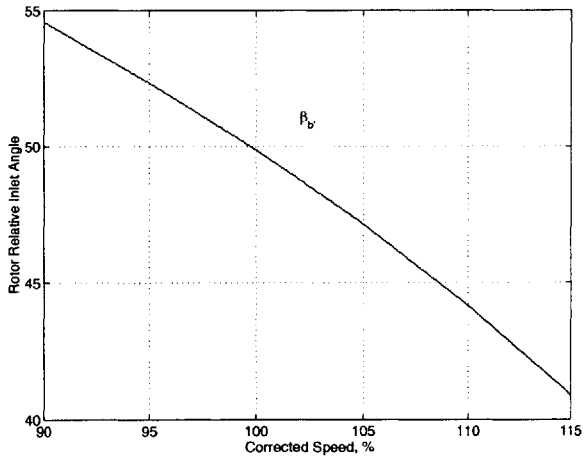

(c) β_b' vs. N_c

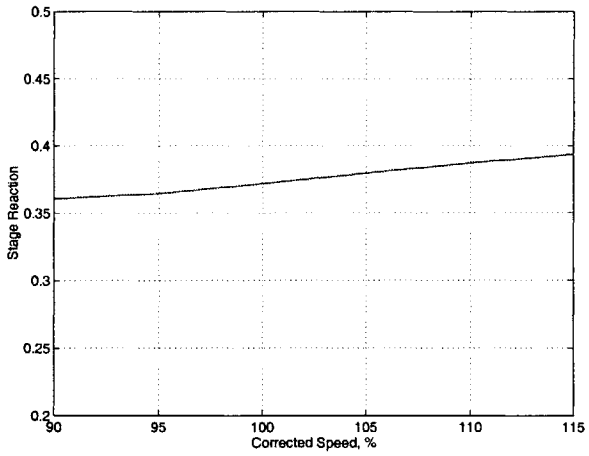

(d) Stage Reaction vs. N_c

Figure 5-26: Model Summary - Film-Cooled Corrected Speed

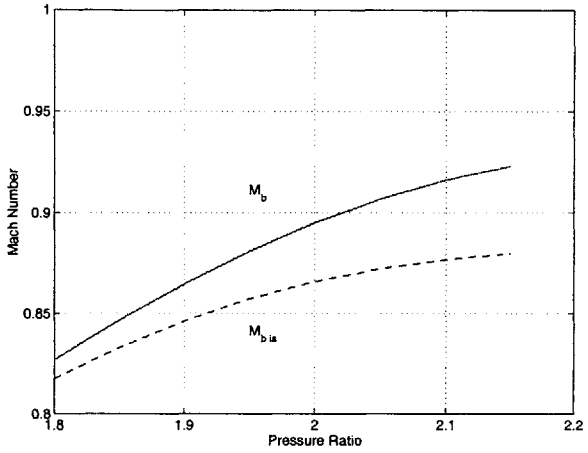

(a) Vane Exit Mach Number vs. π

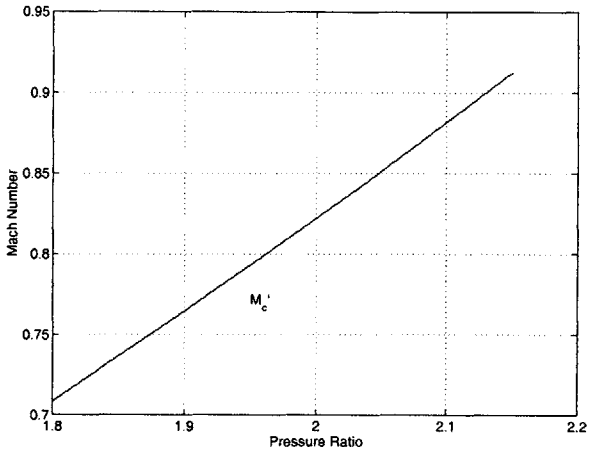

(b) Rotor Exit Mach Number vs. π

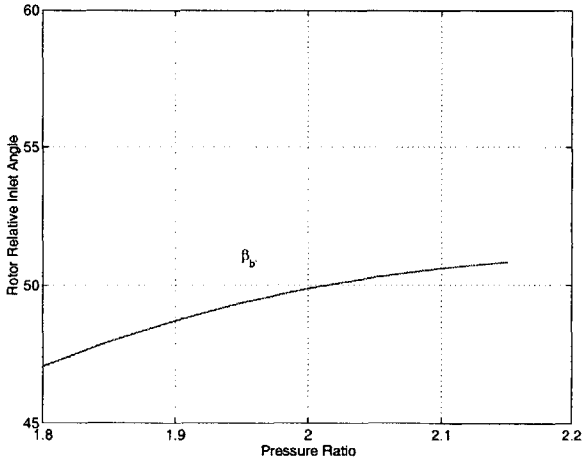

(c) β_b' vs. π

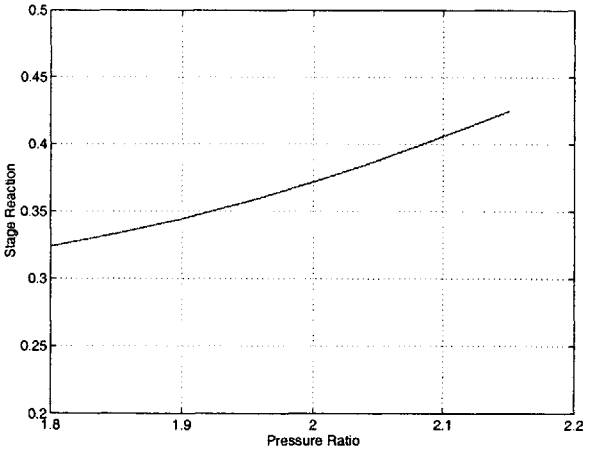

(d) Stage Reaction vs. π

Figure 5-27: Model Summary - Film-Cooled Pressure Ratio

Chapter 6

Film-Cooling Loss Breakdown

6.1 Introduction

This chapter provides a detailed breakdown of the losses associated with film-cooling for the fully-scaled turbine stage that was tested. A detailed breakdown of the film-cooling losses is critical to the design of a high efficiency film-cooled turbine stage. In this thesis film-cooling losses are classified as follows:

- **Mainstream mixing loss:** This loss is caused by the change in mainstream total pressure that results from the mixing of the mainstream and coolant streams.
- **Coolant pumping loss:** This loss is caused by the change in coolant total pressure that results from the mixing of the mainstream and coolant streams.
- **Cooling system losses:** This is the loss within the cooling system between the inlet measurement plane and the coolant plenums.

Of these it is particularly important to quantify the cooling system losses as these losses are generally unique to each turbine configuration[1]. The goal of this chapter is to provide a complete breakdown of these three sources of loss for the vane, blade and heatshield cooling systems.

The mixing losses are estimated using Harstel's mixing layer model, as outlined in Chapter 5, for the vane and blade airfoil film-cooling. The vane inner and outer endwall cooling loss was approximated by redistributing the platform cooling hole area to the vane airfoil surface. The mixing loss associated with the rotor seal leakage was estimated using Shapiro's influence coefficient method. The coolant plenum pressures were estimated using the coolant hole discharge coefficients and the MISES generated airfoil surface pressure distributions. The predicted manifold pressures were calibrated against the experimentally measured manifold pressures. The cooling system losses were estimated using a one dimensional lumped parameter approach.

[1]Test configuration or intended application.

The overall predicted trends for efficiency versus coolant mass flow matched the experimental data. The estimated design point drop in efficiency also closely matched the the measured value, however it is emphasized that it is not possible to accurately predict the absolute loss due to film-cooling because of the uncertainty associated with some of the modeling assumptions. A detailed breakdown of the film cooling losses is presented.

6.2 Approach

Harstel's mixing layer approach was used to estimate the mainstream mixing loss due to film-cooling injection. The method is outlined in detail in Chapter 5, only the loss definition will be reemphasized here. The definition of coolant pumping loss will be presented and the model will be calibrated against the measured manifold pressures for the vane, blade and heatshield. The cooling system losses will be quantified and particular attention is given to loss generated by the rotor coolant on-board injection nozzles.

6.2.1 Mainstream Coolant Mixing Loss

The dimensionless entropy generation for each stream is given by the expression:

$$\frac{s_{ref} - s}{c_p} = \ln\left(\frac{T_t}{T_{t\,ref}}\right) - \frac{\gamma - 1}{\gamma}\ln\left(\frac{P_t}{P_{t\,ref}}\right) \tag{6.1}$$

For the vane the loss is defined in the absolute reference frame and for the blade the loss is defined in the rotor relative reference frame. $P_{t\,ref}$ is a hypothetical mixed out total pressure for the mixing layers and trailing edge injection downstream of each blade row. As the unmixed isentropic efficiency definition is used, each stream is assumed to have a common exit total pressure but independent unmixed total temperatures. In this way the loss does not include entropy generation due to thermal mixing of the streams. For the vane coolant stream there is no change in total temperature from the coolant plenum to the vane mixed out plane. There is no change in the rotor relative total temperatures for the blade coolant stream.

For the mainstream mixing loss Equation 6.1 can be reduced to:

$$\frac{\Delta s_b}{c_p} = -\frac{\gamma - 1}{\gamma}\frac{\Delta P_{t\,n}}{P_{t\,b}} \tag{6.2}$$

$$\frac{\Delta s_c}{c_p} = -\frac{\gamma - 1}{\gamma}\frac{\Delta P'_{t\,r}}{P'_{t\,c}} \tag{6.3}$$

ΔP_t is the drop in mainstream total pressure, and Δs is the increase in mainstream specific entropy. The subscripts n and r denote the nozzle and rotor respectively, and the subscripts b and c denote ideal

mixed out planes downstream of the nozzle guide vane blade row and the rotor blade row. The change in mainstream total pressure is estimated using Harstel's mixing layer method as outlined in Chapter 5.

6.2.2 Coolant Pumping Loss

The coolant pumping loss is defined as the entropy generated from the coolant plenum to a mixed out state downstream of each blade row. As the coolant has a relatively small impact on the mixed out total pressure, the coolant pumping loss is primarily determined by the plenum pressure required to pump the coolant mass flow into the mainstream flow path. This section outlines the procedure used to calculate the vane plenum pressure, the heathield plenum pressure is calculated in a similar manner. The procedure used to calculate the blade plenum pressure is considered in the following section, as coolant undergoes additional pumping work. Figure 6-1 schematically shows the turbine coolant feed system.

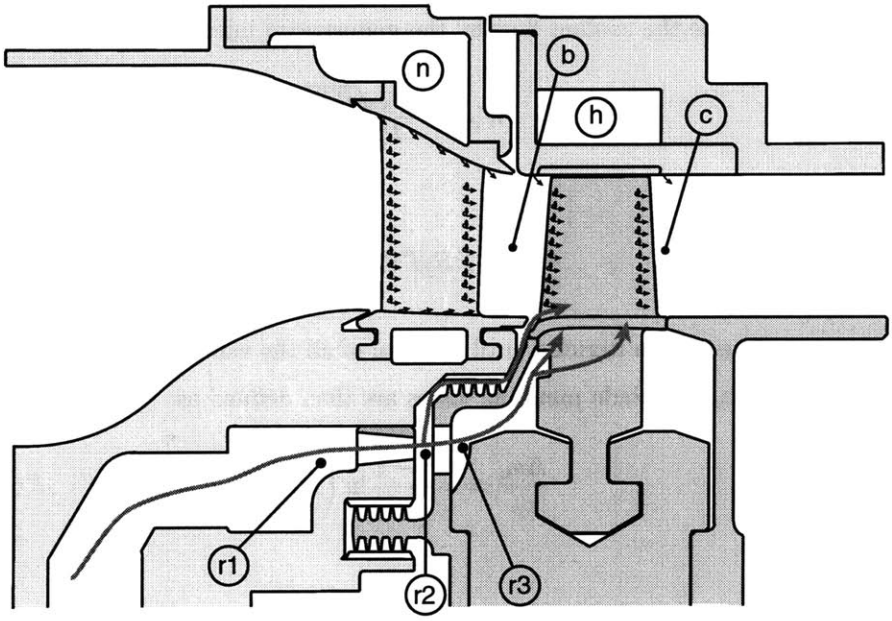

Figure 6-1: Schematic of the Coolant Feed System.

Initially, the vane plenum pressure is specified and the total to static pressure ratio across each cooling hole is calculated. The hole exit static pressure is assumed to be equal to the local static pressure calculated using MISES.

$$PR_j = \frac{P_{t\,n}}{P_{s\,j}} \tag{6.4}$$

The isentropic Mach number across the hole is then estimated from the hole pressure ratio:

$$M_{is\,j} = \left(\left(PR_j^{\frac{\gamma-1}{\gamma}} - 1\right)\frac{2}{\gamma-1}\right)^{\frac{1}{2}} \tag{6.5}$$

The cooling hole throat Mach number is limited to 1.0.

$$M_j = \min\left(1.0, M_{is\,j}\right) \tag{6.6}$$

The hole corrected mass flow is then defined:

$$W_{c\,j} = \frac{M_j\sqrt{\gamma}}{\left(1+\frac{\gamma-1}{2}M_j^2\right)^{\frac{\gamma+1}{2(\gamma-1)}}} \tag{6.7}$$

The hole corrected mass flow can also be defined in terms of the dimensional mass flow, total temperature and pressure and hole area:

$$W_{c\,j} = \frac{\dot{m}_j\sqrt{RT_{t\,n}}}{P_{t\,n}A'_j} \tag{6.8}$$

It is convenient to normalize the coolant flow by the mainstream inlet:

$$W_{c\,a} = \frac{\dot{m}_a\sqrt{RT_{t\,a}}}{P_{t\,a}A_{ref}} \tag{6.9}$$

$$\frac{\dot{m}_j}{\dot{m}_{in}} = PR_jTR_n^{-\frac{1}{2}}\frac{W_cA_jC_d}{W_{c\,a}A_{ref}} \tag{6.10}$$

The vane plenum pressure is then iterated until the sum of all the vane coolant streams equals the specified vane mass flow. The vane, and blade pumping losses are then defined as:

$$\frac{\Delta s_n}{c_p} = -\frac{\gamma-1}{\gamma}\ln\left(\frac{P_{t\,n}}{P_{t\,b}}\right) \tag{6.11}$$

$$\frac{\Delta s_r}{c_p} = -\frac{\gamma-1}{\gamma}\ln\left(\frac{P'_{t\,r}}{P'_{t\,c}}\right) \tag{6.12}$$

$P_{t\,b}$ and $P_{t\,c}$ are the mixed out total pressures at stations b and c. For the coolant stream, the fractional pressure drop is large and the logarithmic form of Equation 6.1 is used:

6.2.3 Coolant System Loss

As the vane and heatshield manifold pressures are measured directly no additional system losses are incurred for these two streams. However, the blade coolant pressure is measured in the stationary reference frame and the coolant flow undergoes significant loss and pumping work en route to the blade plenums. Also, a significant portion of the rotor coolant flow leaks past the rotor seal into the mainstream flow path. The rotor coolant flow path is shown schematically in Figure 6-1. Figure 6-2 shows the velocity triangles for the

coolant flow from Station r1 to Station r3. Commonly tangential on-board injection nozzles (TOBI) are used to reduce the loss associated with bringing the coolant on-board the rotor. For this test normal rather than tangential injection was used and the additional loss incurred must be estimated. The total pressure loss from Station r2 to Station r3 is modeled as a sudden expansion assuming one dimensional compressible flow. The resulting loss is then calculated:

$$\frac{\Delta s_{r2}}{c_p} = -\frac{\gamma - 1}{\gamma} \ln\left(\frac{P_{t\,r1}}{P_{t\,r2}}\right) \tag{6.13}$$

The rotor tangential Mach number can be defined in terms of the corrected speed based on the stage inlet temperature and the rotor coolant temperature ratio and Mach number at Station r2.

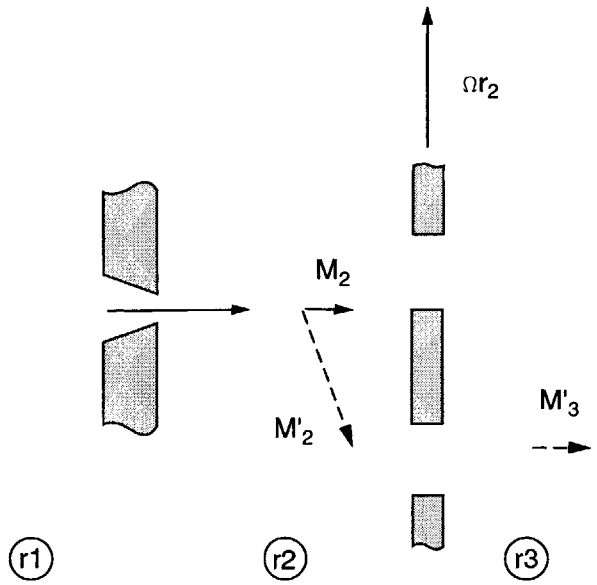

Figure 6-2: Rotor Coolant On-Board Injection Velocity Triangles.

$$M_T = N_c \left(\frac{r_{r2}}{L_{ref}}\right) TR_r^{-\frac{1}{2}} \left(1 + \frac{\gamma - 1}{2} M_{r2}^2\right)^{\frac{1}{2}}$$

The rotor relative coolant Mach number at Station r2 is then calculated:

$$M'_{r2} = \sqrt{M_{r2}^2 + M_T^2}$$

The rotor relative total pressure can then be defined:

$$\frac{P'_{t\,r2}}{P_{t\,r3}} = \left(\frac{1+\frac{\gamma-1}{2}M'^2_{r2}}{1+\frac{\gamma-1}{2}M^2_{r3}}\right)^{\frac{\gamma}{\gamma-1}}$$

It is then assumed that the rotor relative Mach number at Station r3 approximately equals the relative axial Mach number at Station r2. It is assumed that relative tangential momentum is dissipated and there is negligible loss of axial momentum.

$$M'_{r3} = M_{r2}$$

The rotor relative total pressure ratio across the rotor seal plate is:

$$\frac{P'_{t\,r2}}{P'_{t\,r3}} = \left(\frac{1+\frac{\gamma-1}{2}M'^2_{r2}}{1+\frac{\gamma-1}{2}M'^2_{r3}}\right)^{\frac{\gamma}{\gamma-1}}$$

The loss generated across the seal plate can then be quantified:

$$\frac{\Delta s_{r3}}{c_p} = -\frac{\gamma-1}{\gamma}\ln\left(\frac{P'_{t\,r2}}{P'_{t\,r3}}\right) \tag{6.14}$$

Equations 6.13 and 6.14 quantify the major sources of loss in the rotor cooling system upstream of the blade plenums. Elsewhere in the system the coolant flow Mach number is low and the losses generated will be minor. The rotor coolant is then pumped radially from Station r3 through the blade cooling channels. The blade span was segmented into 5 radial nodes and the blade plenum pressure was solved at each node. As the coolant channel Mach number is low the pressure rise along the channel can be defined as:

$$\frac{\Delta P_j}{P_{t\,j}} = \gamma M^2_{T\,j}\frac{\Delta r_j}{r_j}$$

The tangential Mach number is:

$$M_{T\,j} = M_{T\,r2}\left(\frac{r_j}{r_{r2}}\right)$$

The rotor coolant to inlet pressure ratio is solved in the same manner as described for the the vane coolant manifold pressure ratio, except that the spanwise pressure varies. The rotor coolant seal leakage

is modeled as an additional node in the network. The blade plenum pressure, which is used to define the blade pumping loss, is defined as the mass averaged total pressure for five spanwise nodes.

$$P'_{t\,r} = \frac{\sum_{j=1}^{5} \dot{m}_j P'_{t\,j}}{\sum_{j=1}^{5} \dot{m}_j}$$

The mainstream mixing losses are defined by Equation 6.2, the coolant pumping losses are defined by Equation 6.12 and the coolant system losses are defined by equations 6.13 and 6.14. Equation 6.15 relates the entropy generation to overall stage efficiency:

$$\eta = \frac{\sum_{j=1}^{n} \left(1 - e^{\frac{\Delta s_j}{c_p}} \pi_j^{\frac{\gamma-1}{\gamma}}\right) \dot{m}_j}{\sum_{j=1}^{n} \left(1 - \pi_j^{\frac{\gamma-1}{\gamma}}\right) \dot{m}_j} \tag{6.15}$$

π_j is the ratio of exit total pressure to inlet total pressure for each stream.

6.3 Results

The models used to determine the detailed breakdown of the losses due to film-cooling will be calibrated against the measured experimental data. A major source of film-cooling related loss for this turbine stage is coolant pumping loss. The model used to determine the coolant plenum pressures will be calibrated against the measured plenum pressures over a range of coolant mass flows and temperatures. The overall reduction in stage efficiency due to mixing, pumping and cooling system losses will then be compared with the measured reduction in stage efficiency due to film-cooling. A detailed breakdown of the losses due to film-cooling will be presented.

6.3.1 Coolant Manifold Calibrations

Figures 6-3 to 6-5 show a comparison of the model versus the measured plenum pressures for the vane, rotor and heatshield. In each case the model is tuned to match the experimental results. For the blade, the discharge coefficient of rotor seal was adjusted to match the model with the data. The resulting discharge coefficient of 0.40 is reasonable for this geometry. The discharge coefficient of each cooling row was calibrated using the test setup described by Spadaccini [23].

The vane cooling hole discharge coefficients were not calibrated in isolation as were the blade cooling hole rows. It proved too difficult to seal the vane platform edges in order to perform the calibration. Instead, the leading edge calibration curve from the blade calibration test was assumed to be representative of the vane cooling holes. The hole area in the model was adjusted until the results matched the experimentally measured vane plenum pressures. The same procedure was used to calibrate the model of the heatshield plenum.

Figures 6-3 to 6-5 show the vane, rotor and heatshield inlet coolant pressures normalized by the stage inlet total pressure. The data is plotted as a function of coolant-to-mainstream momentum flux ratio normalized by the design point value. In this way the data for different coolant-to-mainstream temperature ratios can be more easily compared. A normalized momentum flux ratio is easily defined despite the fact that would be difficult to define the actual momentum flux ratio. The normalized momentum flux ratio is defined in Chapter 3.

Figures 6-3 and 6-4 show that the model can be used to accurately predict both the vane and rotor coolant supply pressures. Figure 6-5 illustrates a problem with the design of the heatshield manifold. The knee in the model curve occurs when the heatshield plenum pressure fall below upstream freestream static pressure. For the experimental data, coolant momentum flux ratios below the value at the knee will result in reverse flow into heatshield manifold, whereas the model assumes zero flow. This explains the discrepancy between the model and the data at low momentum flux ratios. Fortunately the heatshield flow constitutes a very small portion of the overall coolant ideal enthalpy drop across the stage and the shortcoming of the model has a negligible impact on the overall analysis. The problem with the heatshield design arose

because additional baffling required to balance the heatshield cooling flow was not incorporated. The losses associated with the heatshield cooling flow were not modeled. At the design point, 90% of the heatshield coolant is injected downstream of the rotor in the streamwise direction. This will result a small additional loss.

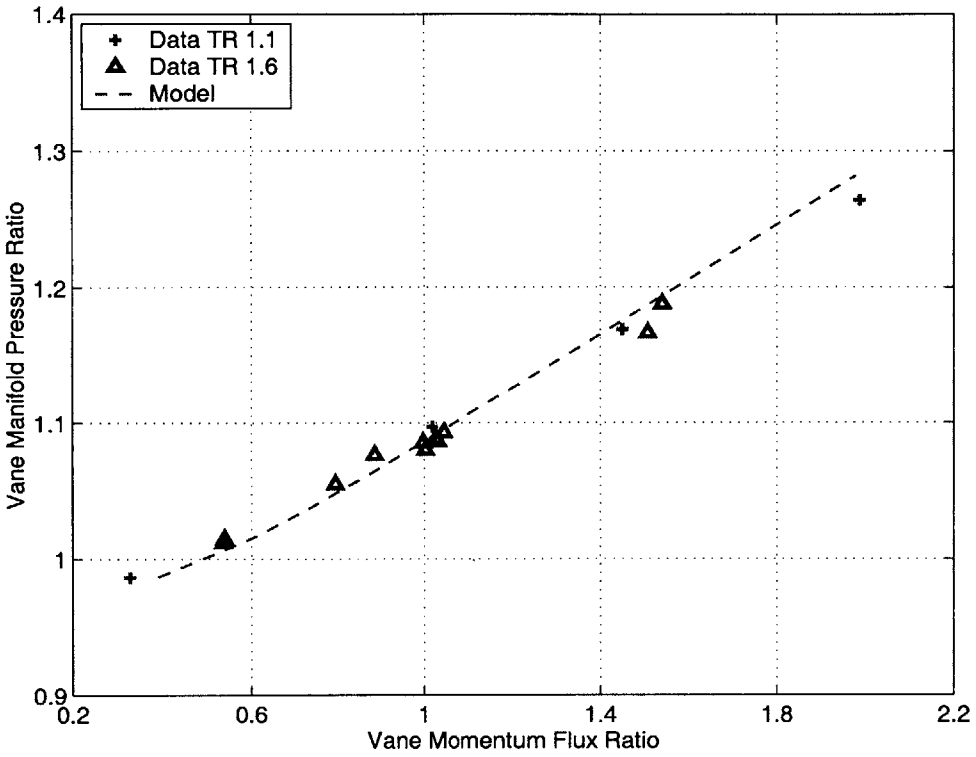

Figure 6-3: Vane manifold model calibration results.

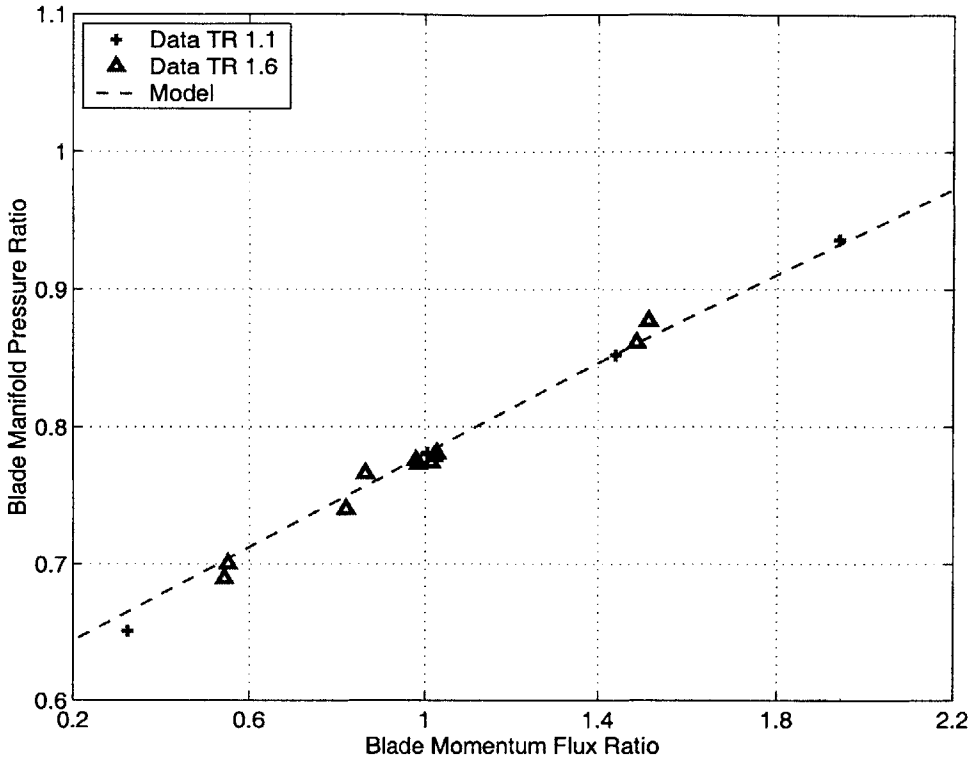

Figure 6-4: Blade manifold model calibration results.

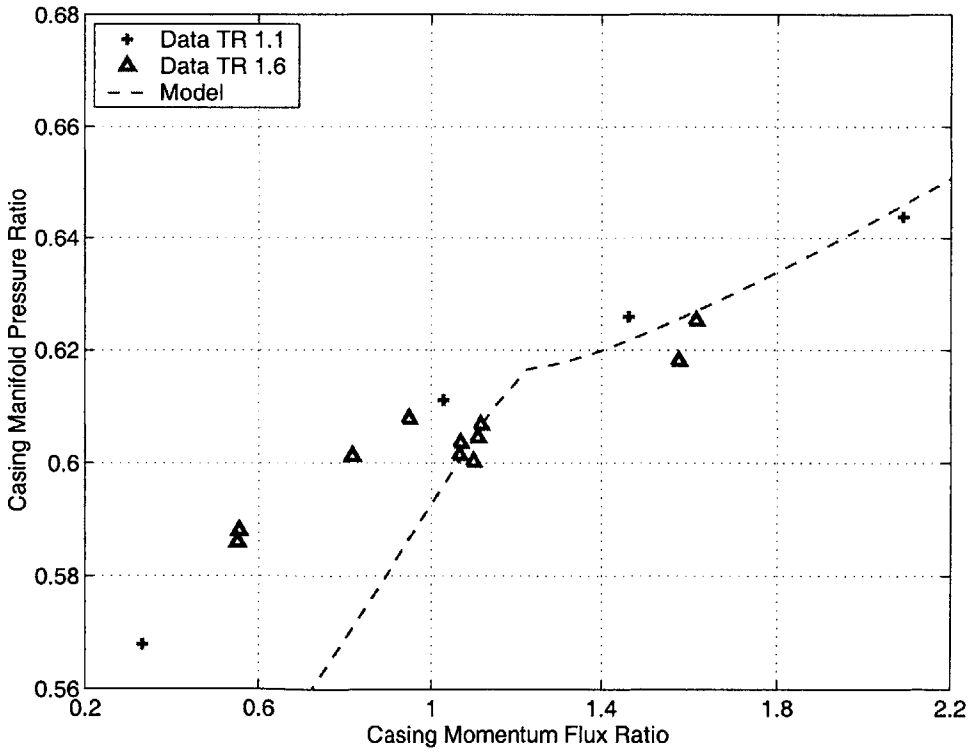

Figure 6-5: Casing manifold model calibration results.

6.3.2 Comparison of Overall Results

Figure 6-6 shows a comparison of the measured stage efficiency for the two coolant-to-mainstream temperature ratios tested with the model over a range of coolant-to-mainstream momentum flux ratios. The 'efficiency change' in Figure 6-6 is difference between the film-cooled turbine measurements and baseline test of the uncooled turbine geometry. This does not represent the loss due to film-cooling. The design point efficiency change is predicted reasonably well. The measured trend for the variation of efficiency change with coolant momentum flux ratio differs some what. At high momentum flux ratios (≈ 2) the heatshield coolant loss should be modeled. A higher portion of the heatshield coolant flow will be injected upstream of the rotor, normal to the mainstream flow, which will result in higher mainstream mixing losses.

At low coolant-to-mainstream momentum flux ratios, the loss due to coolant injection is over predicted. This difference could possibly be explained by the Differential Work Extraction model proposed by Rose and Harvey[19]. The meanline velocity triangle model used in this thesis assumes that the NGV wake is fully mixed out upstream of the rotor. Given the short gap between the stator and rotor this may not be an accurate assumption. The model proposed by Rose and Harvey assumes that the NGV wake mixes out downstream of the rotor. Using this model they showed that the wake mixing loss is reduced by the presence of the rotor. The discrepancy between the meanline model and the measured trend is consistent with their suggestion that the wake mixing loss is reduced (as low coolant momentum flux rates will increase the NGV wake momentum deficit).

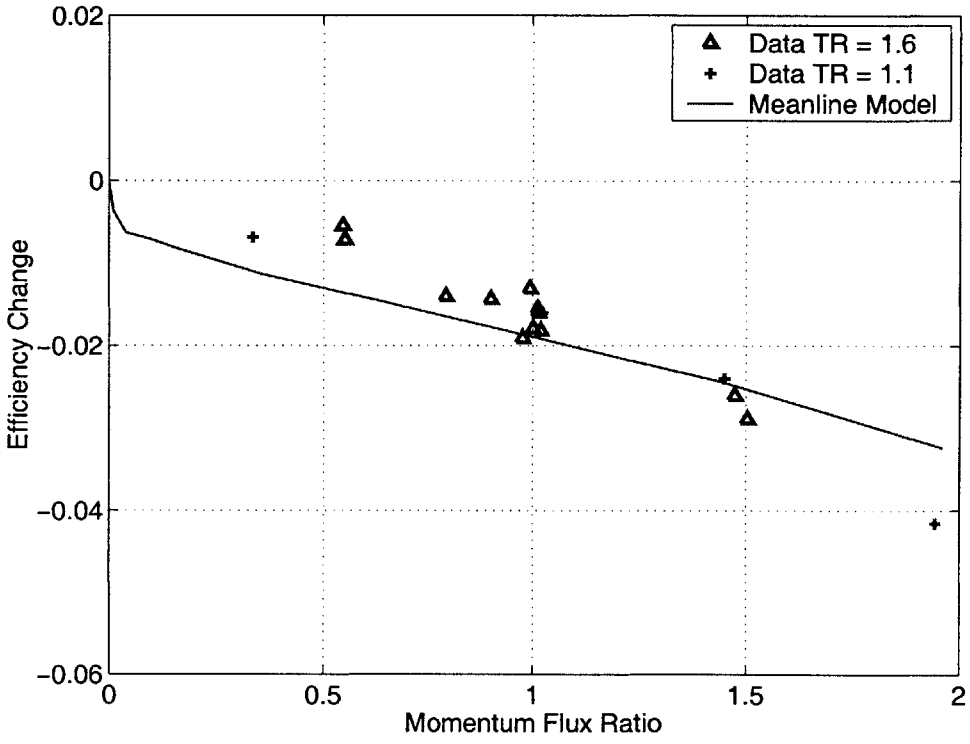

Figure 6-6: Isentropic Change Efficiency vs. Coolant Momentum Flux Ratio

6.3.3 Film-Cooling Loss Breakdown

Figure 6-7 presents an overall summary of the film-cooling losses for the stage. The profile and endwall losses (non-cooling losses) are reduced as the coolant flow rate is increased because of the increased stage reaction. This figure shows the relative magnitude of the vane and blade coolant losses. Both the vane and blade coolant losses increase significantly with increased coolant mass flow. Figures 6-8 and 6-9 show a breakdown of the vane and blade losses respectively. It is interesting to note the differences between the vane and blade loss breakdowns. As the rotor coolant mass flow is approximately half that of the vane, the efficiency drop per unit mass flow is significantly higher for the rotor cooling than for the nozzle guide vane. For the vane, the mainstream mixing loss is significantly reduced at high coolant mass flows. The increased pumping loss at high coolant flow rates is offset significantly by the reduced mixing loss. However, as shown in Figure 6-9 this is not the case with the rotor cooling. A primary reasons for the difference between the vane and rotor loss characteristic is due to basic geometric differences of the cooling schemes and the stage velocity triangles. Generally, the vane has large leading edge radius which allows it's cooling holes to be angled in the streamwise direction, significantly reducing the mainstream mixing loss. The blade leading edge radius small [2] which prevents the cooling holes form being oriented in the streamwise direction. Consequently, the blade leading edge coolant, which comprised a significant portion of the rotor coolant mass flow, is injected normal to the streamwise direction producing significant loss. The high pumping loss at high coolant flow rates is not offset by reduced mixing loss as it is for the vane.

The local Mach number at the leading edge of the blade where the coolant is injected is significantly higher for the blade than it is for the vane. The difference in local Mach number is related to the stage reaction. A comparison of figures 6-8 and 6-9 suggests that the influence of the stage reaction on the coolant mixing loss due to leading edge injection is an important consideration.

Table 6.1: Design Point Coolant Loss Summary

Coolant Stream	Coolant %	Mixing Loss $\Delta\eta$	Pumping Loss $\Delta\eta$	System Loss $\Delta\eta$	Total Loss $\Delta\eta$
Vane	65	0.57	0.40	-	0.97
Blade	28	1.23	0.31	0.35	1.89
Heatsield	7	-	-	-	-
Total	100	1.80	0.71	0.35	2.86

[2] Relative to the cooling hole diameter.

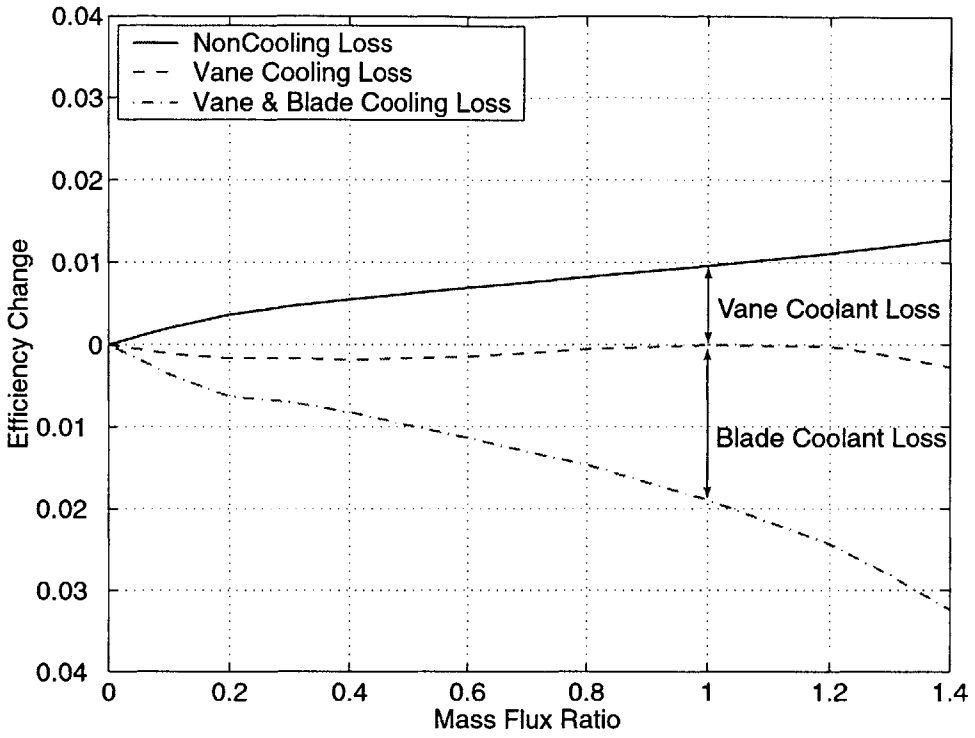

Figure 6-7: Overall loss breakdown.

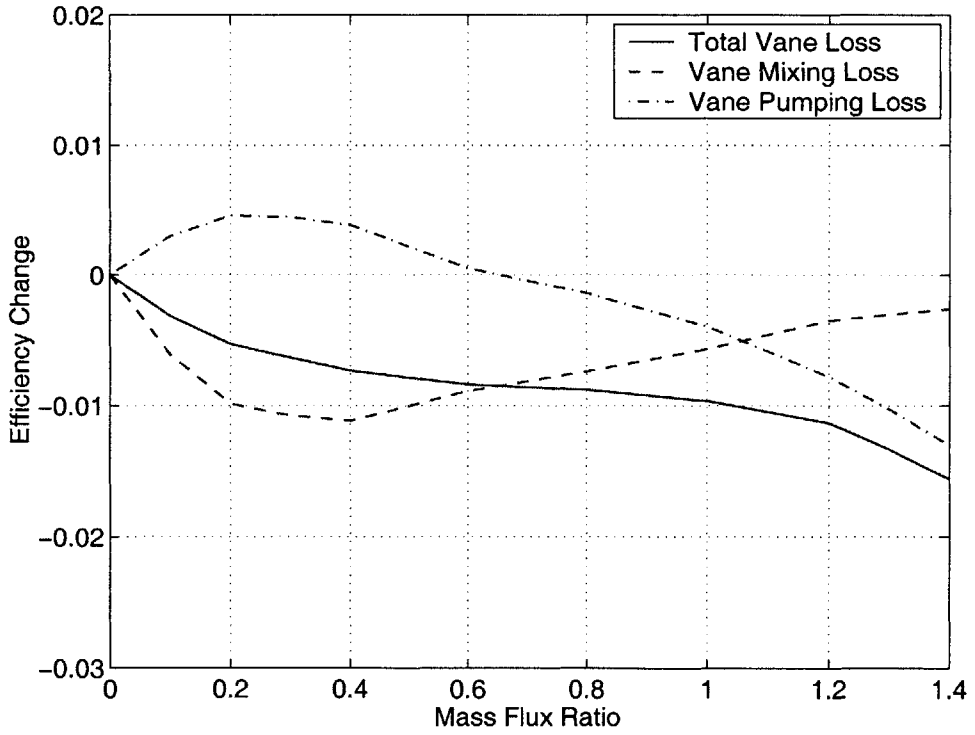

Figure 6-8: Vane loss breakdown.

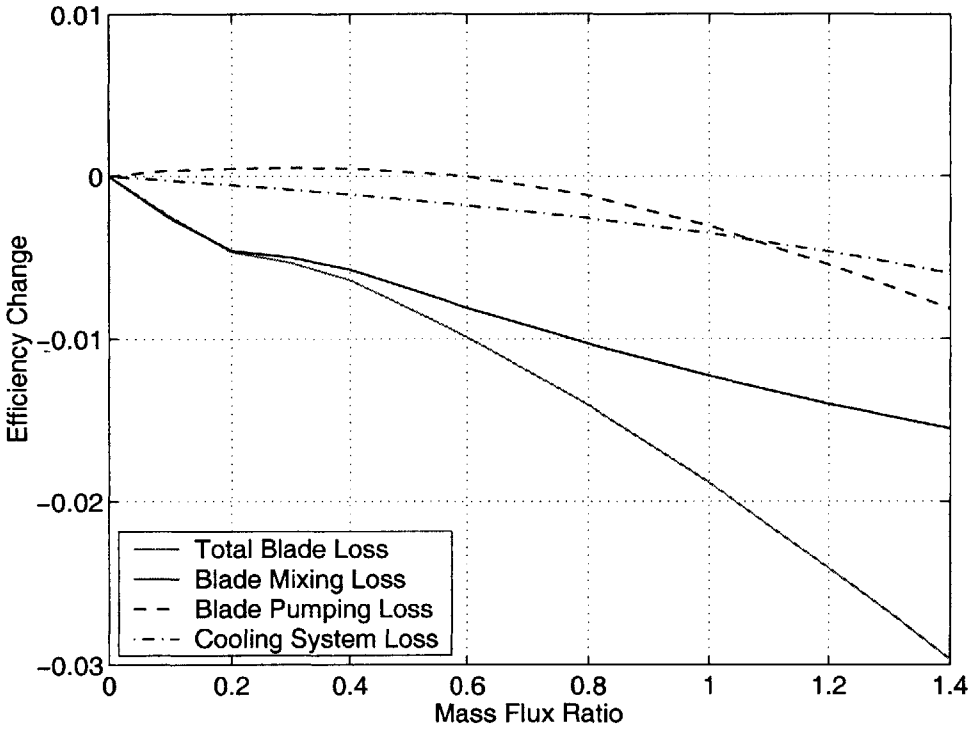

Figure 6-9: Blade loss breakdown.

Figure 6-10 shows the results an analysis to examine the uncertainty associated of some different modeling assumptions used. Firstly, the base pressure coefficient was increased from -0.15 to 0.0. Kiock [12] and Sieverding [22] reported increases in the base pressure coefficient of 0.15 and 0.16 respectively. The trailing edge hole geometry of the vane used in this study is significantly different than that reported by Kiock. The increased efficiency (due to increased base pressure resulting from trailing edge ejection) for this turbine stage may not as large as that shown in Figure 6-10.

The baseline analysis assumes that the exit Mach number for each cooling hole equals its throat Mach number. This is a reasonable assumption if the cooling hole entrance is well rounded and the length to diameter ratio of the hole is small. The cooling holes in this study are laser drilled which results in significant flaring at the hole entrance. The assumption of a well rounded entrance for the cooling hole geometry tested here may be reasonable. To assess the impact of using cooling holes with sharp edges the cooling holes were modeled as thick square edged orifices which have a discharge coefficient of 0.84. The flow was modeled as a sudden expansion from the vena contracta and was assumed to be fully mixed out at the hole exit. This results in a reduced cooling hole exit Mach number and an increased mainstream mixing loss. At the design point coolant mass flow this resulted in a further reduction in efficiency of $\approx 1\%$.

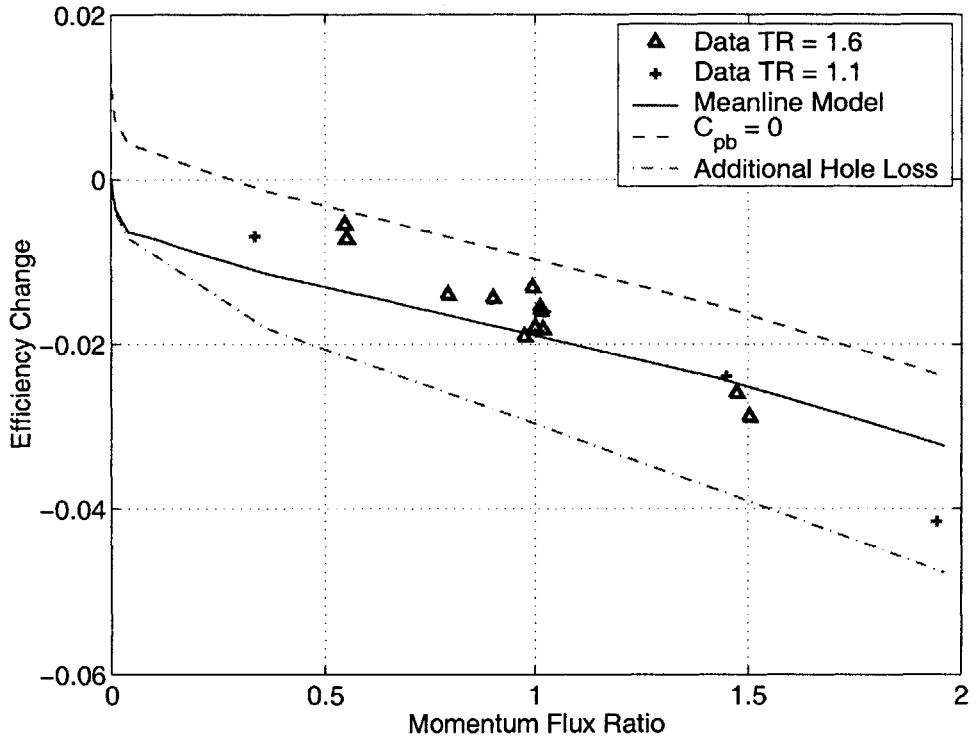

Figure 6-10: Overall stage loss using different modeling assumptions.

6.4 Summary

This chapter has provided a complete breakdown of the film-cooling losses for the fully scaled turbine stage. The film-cooling losses were classified as mainstream mixing loss, coolant pumping loss and cooling system losses. Harstel's mixing layer model was used to estimate the mainstream mixing loss. The coolant plenum pressures, which largely determine the coolant pumping loss, were determined using the airfoil static pressure distributions and the measured cooling hole discharge coefficients. The cooling system loss was estimated using a simple one dimensional analysis. The model of the coolant plenums was calibrated against the measured plenum pressures and total cooling loss was compared with the measured change in efficiency. The model of the film-cooling losses matches the measured results reasonably well for both the magnitude efficiency drop and the predicted trend for the variation of efficiency drop with coolant flow rate.

A detailed breakdown of the losses for the vane and rotor cooling is presented. The specific [3] loss for the rotor coolant is significantly higher than that of the nozzle guide vane. The difference in loss is primarily due lower vane leading edge Mach number and the larger leading edge radius which allows the cooling holes to be aligned in the streamwise direction.

[3]The loss per unit coolant mass flow.

Chapter 7

Concluding Remarks

This chapter will review the objectives for the current research program, and the approach taken in pursuit of these objectives. The primary observations and conclusions are outlined. The original contributions are noted and topics worthy of further consideration are suggested.

7.1 Objective and Approach

The goal of this research is to measure the aerodynamic performance of a film-cooled turbine stage and to quantify the loss caused by film-cooling. The primary challenge was to develop a means of testing the aerodynamic performance of the turbine stage. An appropriate testing technique should model all of the relevant fluid physics; it should be repeatable enough to measure the impact of small design changes; and it should be economically feasible.

The current research program extended the measurement capabilities of the MIT blowdown turbine test facility to measure the turbine stage mass flow and shaft torque. The new measurement techniques, along with previously developed short duration instrumentation, enabled the measurement of the stage efficiency.

The next major challenge lay in identifying the loss caused by film-cooling from the overall performance measurement. In this thesis, the loss due to film-cooling is defined as the difference in performance between the film-cooled turbine and an ideal turbine with the same velocity triangles and airfoil Mach number distributions. However, there is no uncooled turbine geometry that will have the same velocity triangles and Mach number distributions as the film-cooled turbine stage, and consequently, there is no experimental baseline that can be tested to determine the loss due to film-cooling.

In this thesis a model of the stage meanline velocity triangles was used to predict the performance of the ideal stage, and thereby estimate the loss due to film-cooling. The loss characteristics of the stage were estimated using a combination of 2-D CFD and semi-empirical loss correlations. The efficiency predictions were calibrated against measured performance of the uncooled turbine geometry. The model mass flow predictions were calibrated against the film-cooled and baseline mass flow measurements.

7.2 Observations and Conclusions

Efficiency Measurement

Short duration test facilities can match all of the relevant non-dimensional parameters to simulate the performance of a film-cooled turbine stage. These facilities also enable turbine stages to be tested for a fraction of the cost of steady state rigs. The current research program demonstrated that a short duration facility can be used to make extremely repeatable efficiency and mass flow measurements. The estimated repeatability (U_{95}) for the efficiency measurement of the uncooled turbine geometry is $\pm$ 0.14%. The repeatability of these measurements was estimated from the standard deviation of a least squares fit of the measured efficiency, corrected speed and pressure ratio [1]. Based on this measurement repeatability, the net effect of a design change can be determined with an uncertainty of just $\pm$0.1% if four measurements are repeated for each design configuration. Using the MIT blowdown turbine facility, four such tests can be completed in a single day of testing. This research program demonstrated that turbine stages can be tested in short duration facilities under fully-scaled conditions, inexpensively, and with the repeatability to examine the impact of small design changes on the performance of a high pressure turbine stage. This technique is a feasible alternative to the use of steady turbine test rigs and represents a major contribution to the field of turbomachinery research.

Film-Cooling Loss

A methodology for determining the loss due to film-cooling has been presented. The film-cooling loss cannot be measured directly, as there is no uncooled geometry that has the same velocity triangles and airfoil Mach number distributions as the as the film-cooled turbine stage. Instead, a meanline velocity triangle model of the stage and the film-cooled efficiency measurements together are used to estimate the loss due to film-cooling. The nozzle guide vane and rotor blade row loss characteristics were estimated as follows:

- MISES was used to calculate airfoil profile losses and an additional loss was added to model unsteady Von Karman type vortex shedding behind the blunt trailing edges of the vane and blade.
- The endwall losses were estimated using a semi-empirical loss correlation proposed by Sharma and Butler (1987).
- The influence of film-cooling and trailing edge ejection on the mainstream Mach number and loss is modeled using Harstel's mixing layer approach.

The meanline velocity triangle model was calibrated against the efficiency measurements of the uncooled geometry. The measured corrected mass flow for the baseline and film-cooled tests were also used to verify the modeling assumptions.

[1] This approach is discussed under the 'Applied Considerations' of the ANSI Measurement Uncertainty supplement to the Performance Test Codes PTC 19.1-1985.

This model was then used to estimate the performance of an ideal stage with the same velocity triangles and airfoil Mach number distributions as film-cooled stage, but without the coolant. The estimated loss due to film-cooling was 3.0% at the design point, which corresponds to 0.3% per percent of coolant. As the coolant flow rate is increased past the design point, the loss increases at a rate of 0.5% for each additional percent of cooling flow.

The loss due to film-cooling is small when compared to the overall benefit that is achieved from operating the gas turbine engine at higher turbine inlet temperatures. However, it is a significant source of loss that must be considered in detail to accurately predict the overall efficiency and power of a gas turbine engine. This thesis presents an experimental approach that can be used to measure the efficiency of a film-cooled turbine stage. This thesis also presents and analytical approach that can be used with the measurements to estimate the loss due to film-cooling. A detailed breakdown of the cooling losses for this stage was presented to show the losses that are unique to the test facility and to show the most important contributions to the overall loss. This research has significantly reduced the uncertainty associated with predicating the additional turbine loss associated with film-cooling for this stage.

7.3 Recommendations for Future Work

- The stage efficiency is reduced by 1.4% for each percent increase in rotor tip gap. The efficiency sensitivity to tip gap increases with corrected speed. This trend is not consistent with any tip gap correlations, however a similar trend was observed from a 3D multi-stage Navier-Stokes CFD simulation [2]. This trend, which is worthy of further investigation, may be a result of the interaction between endwall and tip gap flows, as the endwall losses for this stage are particularly high.

- The sensitivity to changes in corrected speed (blade incidence angle) changed significantly as a result of film-cooling. For the baseline stage, each percent increase in corrected speed increased the stage efficiency by 0.05%, whereas the film-cooled stage efficiency increased by 0.13%. This observation was not previously noted in any rotating rig test or cascade tests. This observation suggests that the blade leading edge ejection has significantly changed the relationship between the blade loss and incidence angle. This observation is worthy of further consideration.

- In this thesis a relatively straight forward one dimensional approach was used to estimate the ideal stage with which to compare the film-cooled results. A 3D CFD multi-stage analysis with coolant injection should be used to provide an alternative means of estimating the performance of the ideal.

- The coolant loss model used in this thesis assumes that the NVG wake is fully mixed out upstream of the rotor blade row. An alternative approach, proposed by Rose and Harvey [19], assumes the wake is convected through the rotor blade row and mixes out downstream of the rotor. The wake, because

[2]This calculation was performed by the program sponsor.

of it's lower total pressure, does less work and difference in total pressure between NGV wake an freestream is reduced, which in turn results in a reduced mixing loss. This alternative approach for modeling the NGV wake should be compared with the measured data. The model results presented in reference [19] appear to have important design implications. The loss resulting from deep NGV wakes produced by film-cooling or separation may be significantly reduced by the presence of the rotor. This may also be an important consideration for the design of a counter-rotating turbine stage where the rotor wake mixing is also influenced by differential work extraction.

- A test facility now exists to economically test turbine configurations that make use of film-cooling to enable the design of more highly loaded turbine stages. As endwall losses account for over 50% of the non-cooling loss for this stage, particular attention should be paid to secondary flows.

Appendix A

Measurement Uncertainty

A.1 Pre-Test Uncertainty Analysis

A pre-test uncertainty analysis was conducted in order to reduce the measurement uncertainty of this experiment. The pre-test uncertainty analysis was based on data and information that existed before the test, such as calibration histories, previous tests with similar instrumentation, prior measurement uncertainty analysis, expert opinions and as necessary, special tests. For this test there were alternative test designs, instrumentation arrangements, and alternative calculation procedures that were considered. The pre-test uncertainty analysis was used to guide the design of this experiment. The following analysis utilizes the ANSI/ASME [1] convention for uncertainty analysis.

For algebraic convenience, this analysis will assume calorically perfect gas behavior so that efficiency may be written as follows:

$$\eta = \frac{\mathcal{T} \cdot \omega}{\dot{m}_t C_P T_t \left(1 - \pi_t^{\frac{R}{C_P}}\right)} \tag{A.1}$$

The efficiency precision index is expressed as the root sum square of all the precision indices of the contributing measurements:

$$\begin{aligned} S_\eta = \Bigg[&\left(\frac{\delta\eta}{\delta\mathcal{T}} \cdot S_\mathcal{T}\right)^2 + \left(\frac{\delta\eta}{\delta m} \cdot S_m\right)^2 \\ &+ \left(\frac{\delta\eta}{\delta C_p} \cdot S_{C_p}\right)^2 + \left(\frac{\delta\eta}{\delta T_t} \cdot S_{T_t}\right)^2 + \left(\frac{\delta\eta}{\delta\pi} \cdot S_\pi\right)^2 \Bigg]^{\frac{1}{2}} \end{aligned} \tag{A.2}$$

This expression can be non-dimensionalized by introducing influence coefficients:

$$C_* = \frac{\delta\eta}{\delta *} \cdot \frac{*}{\eta} \tag{A.3}$$

Table A.1: Pretest Uncertainties

Quantity	C_*	$B_*/*$	$S_*/*$	t_{95}	U_{95}
T_t	1.0	0.01%	0.03%	2.0	.06%
$\dot{m}$	1.0	0.35%	0.13%	2.0	.41%
$\mathcal{T}$	1.0	0.10%	0.13%	2.0	.28%
π	1.34	0.10%	0.15%	2.0	.30%
C_p	0.07	0.20%	-	2.0	.20%
η	-	0.37%	0.37%	2.0	.65%

Then equation Equation (A.2) can be rewritten as:

$$\begin{aligned}\frac{S_\eta}{\eta} = \Bigg[&\left(C_{\mathcal{T}} \cdot \frac{S_{\mathcal{T}}}{\mathcal{T}}\right)^2 + \left(C_{\dot{m}} \cdot \frac{S_{\dot{m}}}{\dot{m}}\right)^2 \\ &+ \left(C_{C_p} \cdot \frac{S_{C_p}}{C_p}\right)^2 + \left(C_T \cdot \frac{S_{T_t}}{T_t}\right)^2 + \left(C_\pi \cdot \frac{S_\pi}{\pi}\right)^2\Bigg]^{\frac{1}{2}}\end{aligned} \tag{A.4}$$

This is a more useful form than that of equation Equation (A.2). The influence coefficient is a non-dimensional parameter that represents the how a given error source will be propagate to overall measurement error. The influence coefficient represents the relative amplification of that source error through equation A.1. The influence coefficients for $C_{\mathcal{T}}$, C_m, and C_{T_t} are:

$$C_{\mathcal{T}} = C_m = C_{T_t} = 1 \tag{A.5}$$

However the expressions C_{C_p} and C_π are considerably more complicated:

$$\begin{aligned}C_{C_p} &= \left(1 + \frac{\pi^{\frac{R}{C_p}} \cdot R \cdot ln\left(\pi\right)}{c_p \cdot \left(1 - \pi^{\frac{R}{C_p}}\right)}\right) \\ &= \left(1 + \frac{\pi^{\frac{\gamma-1}{\gamma}} \cdot \frac{\gamma-1}{\gamma} \cdot ln\left(\pi\right)}{\left(1 - \pi^{\frac{\gamma-1}{\gamma}}\right)}\right)\end{aligned} \tag{A.6}$$

Equations were derived using a symbolic differentiation program and the results were verified numerically using sample values for γ and π.

$$C_\pi = \frac{\pi^{\frac{R}{C_p}} \cdot R}{C_p \cdot \left(1 - \pi^{\frac{R}{C_p}}\right)} = \frac{\pi^{\frac{\gamma-1}{\gamma}} \cdot \frac{\gamma-1}{\gamma}}{\left(1 - \pi^{\frac{\gamma-1}{\gamma}}\right)} \tag{A.7}$$

Similarly the Bias limits can be defined as:

$$B_\eta = \left[\left(\frac{\delta\eta}{\delta\mathcal{T}}\cdot B_\mathcal{T}\right)^2 + \left(\frac{\delta\eta}{\delta m}\cdot B_m\right)^2 + \left(\frac{\delta\eta}{\delta C_p}\cdot B_{C_p}\right)^2 + \left(\frac{\delta\eta}{\delta T_t}\cdot B_{T_t}\right)^2 + \left(\frac{\delta\eta}{\delta\pi}\cdot B_\pi\right)^2\right]^{\frac{1}{2}} \tag{A.8}$$

In terms of the influence coefficients:

$$\frac{B_\eta}{\eta} = \left[\left(C_\mathcal{T}\cdot\frac{B_\mathcal{T}}{\mathcal{T}}\right)^2 + \left(C_m\cdot\frac{B_m}{m}\right)^2 + \left(C_{C_p}\cdot\frac{B_{C_p}}{C_p}\right)^2 + \left(C_T\cdot\frac{B_{T_t}}{T_t}\right)^2 + \left(C_\pi\cdot\frac{B_\pi}{\pi}\right)^2\right]^{\frac{1}{2}} \tag{A.9}$$

Table A.1 shows sample values for the influence coefficients. This shows that the uncertainty in pressure ratio will be amplified whereas the uncertainty in C_p will be significantly reduced.

A.2 Post-Test Uncertainty Evaluation

A post-test analysis was required to establish the actual uncertainty intervals. It was also used to evaluate the pretest precision estimates. The final uncertainty estimates are based on the pretest bias estimates and the post-test precision measurements.

A least squares regression analysis of the each data series was used to simplify the presentation of the results in Chapter 3. This regression analysis also yielded the standard deviation of data from the curve fit:

$$S_{fit} = \left[\frac{\sum_{j=1}^{N}\left(\eta_j - \eta\left(\Delta\pi_j, \Delta N_{c\,j}\right)\right)^2}{N-1}\right]^{\frac{1}{2}} \tag{A.10}$$

The precision index of the series, also known as the standard error of estimate, is defined as:

$$S = \left[\frac{\sum_{j=1}^{N}\left(\eta_j - \eta\left(\Delta\pi_j, \Delta N_{c\,j}\right)\right)^2}{N-C}\right]^{\frac{1}{2}} = S_{fit}\left(\frac{N-1}{N-C}\right)^{\frac{1}{2}} \tag{A.11}$$

where C is the number of coefficients of the regression, and N is the number of measurements. Higher order curve fits will reduce the standard deviation of the fit, however, the predicted trends may not be physical. The standard error of estimate gives a better estimate of the random errors in the measurements.

If there are M redundant tests for a given configuration, the following pooled estimate of the precision

indices can be used:

$$S_{pooled} = \left[\frac{\sum_{j=1}^{M} {S_j}^2}{M} \right]^{\frac{1}{2}} \tag{A.12}$$

As there is no significant change to the test setup, the two tip gap measurement series can be pooled for the purposes of estimation the precision index. Table A.2 summarizes the post-test uncertainty analysis.

Table A.2: Post-Test Uncertainties

Series	N	C	S_η/η_{fit}	M	S_η/η_{pooled}	v	t_{95}	$t_{95}S$	U_{95}
1	8	5	0.053	2	0.049	14	2.145	0.14	0.40
2	8	5	0.044	2	0.049	14	2.145	0.14	0.40
3	12	5	0.166	1	0.166	11	2.201	0.38	0.53

Appendix B

Appendix B

B.1 Multi Inflow Turbine Isentropic Exit Temperature

This appendix will derive the isentropic exit temperature (Equation4.2) for a multi-inflow turbine stage. For a constant pressure process the entropy change for each stream is:

$$\frac{s_m - s_j}{c_p} = ln\left(\frac{T_{m\,is}}{T_{is\,j}}\right)$$

For an isentropic process the mass weighted entropy change for all of the streams will sum to zero:

$$\sum_{j=1}^{n} \dot{m}_j ln\left(\frac{T_{m\,is}}{T_{is\,j}}\right) = 0$$

This expression can then be manipulated to yield the common mixed isentropic exit temperature in terms of the inlet temperatures, pressure ratios and mass flows for each of the inlet streams:

$$\sum_{j=1}^{n} ln\left(\frac{T_{m\,is}}{T_{is\,j}}\right)^{\dot{m}_j} = 0$$

$$ln\left(\prod_{j=1}^{n}\left(\frac{T_{m\,is}}{T_{is\,j}}\right)^{\dot{m}_j}\right) = 0$$

$$\prod_{j=1}^{n} T_{m\,is}^{m_j} = \prod_{j=1}^{n} T_{is\,j}^{m_j}$$

$$T_{m\,is} = \prod_{j=1}^{n} (T_{is\,j})^{\frac{\dot{m}_j}{\sum_{j=1}^{n} \dot{m}_j}}$$

$$T_{m\,is} = \prod_{j=1}^{n} \left(T_{t\,j} \pi_j^{\frac{\gamma-1}{\gamma}} \right)^{\frac{\dot{m}_j}{\sum_{j=1}^{n} \dot{m}_j}}$$

Appendix C

Trailing Edge Loss Model

The following trailing edge loss model was origonaly proposed by Stewart (1955). The basic loss model was subsequently modified by Goldman and Gaugler (1980) to include trailing edge injection. The model was again modified by Köllen (1995) to allow for trailing edge base pressures below the trailing edge freestream value. This appendix presents a further modification to include pressure and suction surface mixing layers in the analysis. This appendix presents an extension of the model proposed by Köllen. Figure C-1 shows the trailing edge control volume.

The following variables are defined in order to simplify the equations where the specific heat ratio, γ, appears frequently:

$$\gamma_1 = \frac{\gamma - 1}{2} \qquad \gamma_2 = \frac{\gamma - 1}{\gamma} \qquad \gamma_3 = \frac{\gamma}{\gamma - 1}$$
$$\gamma_4 = \frac{\gamma + 1}{2\gamma} \qquad \gamma_5 = \frac{\gamma - 1}{\gamma + 1} \qquad \gamma_6 = \frac{\gamma}{\gamma + 1} \tag{C.1}$$

The dimensionless boundary layer parameters defined:

$$\delta_1^* = \frac{\delta_{1s}^* + \delta_{1d}^*}{t \cos \alpha_1} \qquad \delta_2^* = \frac{\delta_{2s}^* + \delta_{2d}^*}{t \cos \alpha_1} \tag{C.2}$$

$$\delta_h = \frac{\delta_{hs} + \delta_{hd}}{t \cos \alpha_1} \qquad \delta_{te} = \frac{d}{t \cos \alpha_1} \tag{C.3}$$

$$\delta_{sl} = \frac{n \frac{\pi}{4} d_{sl}^2}{th \cos \alpha_1} \qquad \delta_{fe} = \frac{d}{t} \cos \alpha_1 \tag{C.4}$$

The upstream mass, momentum and energy contributions to the control volume are normalized by their

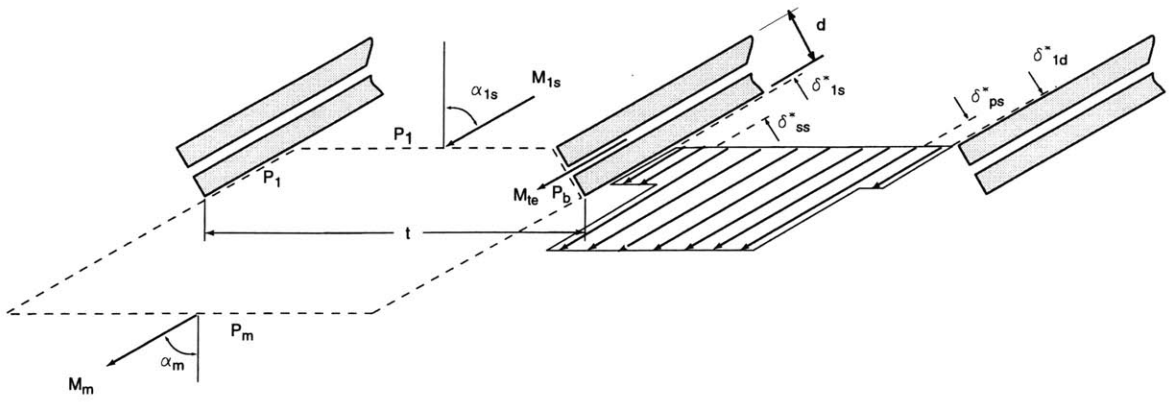

Figure C-1: Trailing Edge Loss Model.

respective inlet freestream values in order to simplify the conservation equations:

$$B_{te} = \frac{M_{te}}{M_{1s}} \left(\frac{T_{s\,te}}{T_{s\,fs}} \right)^{-\frac{1}{2}} \qquad J_{te} = \frac{M_{te}^2}{M_{1s}^2} \qquad E_{te} = \frac{T_{s\,te}}{T_{s\,fs}} \frac{M_{te}}{M_{1s}} \left(\frac{T_{s\,te}}{T_{s\,fs}} \right)^{-\frac{1}{2}}$$

$$B_{ps} = \frac{M_{ps}}{M_{1s}} \left(\frac{T_{s\,ps}}{T_{s\,fs}} \right)^{-\frac{1}{2}} \qquad J_{ps} = \frac{M_{ps}^2}{M_{1s}^2} \qquad E_{ps} = \frac{T_{s\,ps}}{T_{s\,fs}} \frac{M_{ps}}{M_{1s}} \left(\frac{T_{s\,ps}}{T_{s\,fs}} \right)^{-\frac{1}{2}}$$

$$B_{ss} = \frac{M_{ss}}{M_{1s}} \left(\frac{T_{s\,ss}}{T_{s\,fs}} \right)^{-\frac{1}{2}} \qquad J_{ss} = \frac{M_{ss}^2}{M_{1s}^2} \qquad E_{ss} = \frac{T_{s\,ss}}{T_{s\,fs}} \frac{M_{ss}}{M_{1s}} \left(\frac{T_{s\,ss}}{T_{s\,fs}} \right)^{-\frac{1}{2}}$$

The static temperature ratios are:

$$\frac{T_{s\,te}}{T_{s\,fs}} = \frac{T_{t\,te}}{T_{t\,fs}} \frac{1 + \gamma_1 M_{sf}^2}{1 + \gamma_1 M_{te}^2} \tag{C.5}$$

$$\frac{T_{s\,ps}}{T_{s\,fs}} = \frac{T_{t\,ps}}{T_{t\,fs}} \frac{1 + \gamma_1 M_{sf}^2}{1 + \gamma_1 M_{ps}^2} \tag{C.6}$$

$$\frac{T_{s\,ss}}{T_{s\,fs}} = \frac{T_{t\,ss}}{T_{t\,fs}} \frac{1 + \gamma_1 M_{sf}^2}{1 + \gamma_1 M_{ss}^2} \tag{C.7}$$

The control volume conservation equations can then be expressed as:

$$\rho_1 c_{1s} \cos\alpha_1 T1 = \rho_m c_m \cos\alpha_m \tag{C.8}$$

$$\rho_1 c_{1s}^2 \cos^2\alpha_1 T2 + p_1 (1 - \delta_{fe}) + p_b \delta_{fe} = \rho_m c_m^2 \cos^2\alpha_m \tag{C.9}$$

$$\rho_1 c_{1s}^2 \cos\alpha_1 \sin\alpha_1 T2 + (p_b - p_1) \tan\alpha_1 \delta_{fe} = \rho_m c_m^2 \cos\alpha_m \sin\alpha_m \tag{C.10}$$

$$\rho_1 c_{1s} T_{t\,1s} \cos\alpha_1 T3 = \rho_m c_m T_{t\,m} \cos\alpha_m \tag{C.11}$$

where

$$T1 = 1 - \delta_1 - \delta_{te} + B_{te}\delta_{s1} - \delta_{ps}\left(1 - B_{ps}\right) - \delta_{ss}\left(1 - B_{ss}\right) \tag{C.12}$$

$$T2 = 1 - \delta_1 - \delta_2 - \delta_{te} + J_{te}\delta_{s1} - \delta_{ps}\left(1 - J_{ps}\right) - \delta_{ss}\left(1 - J_{ss}\right) \tag{C.13}$$

$$T3 = 1 - \delta_1 - \delta_h - \delta_{te} + E_{te}\delta_{s1} - \delta_{ps}\left(1 - E_{ps}\right) - \delta_{ss}\left(1 - E_{ss}\right) \tag{C.14}$$

The critical Mach number (the Mach number based on the stagnation speed of sound) is used to simplify the solution of the conservation equations:

$$M^* = M_{1s}\sqrt{\frac{\gamma + 1}{2\left(1 + \gamma_1 M_{1s}^2\right)}} \tag{C.15}$$

Equations C.9 to C.11 are solved for the axial and tangential components of the exit critical Mach number:

$$M_u^* = D \tag{C.16}$$

$$M_a^* = \gamma_7 C - \sqrt{(\gamma C)^2 - 1 + \gamma_5 D^2} \tag{C.17}$$

where

$$C = \sqrt{\frac{T_{t\,m}}{T_{t\,0}}}\frac{T2(\cos\alpha_1{}^2 M^{*2} + \gamma_4\left(1 - \gamma_5 M^{*2}\right)\delta_{fe}P_b + \gamma_4\left(1 - \gamma_5 M^{*2}\right)\left(1 - \delta_{fe}\right)}{T1\cos\alpha_1 M^*} \tag{C.18}$$

$$D = \sqrt{\frac{T_{t\,m}}{T_{t\,0}}}\frac{T2(\cos\alpha_1\sin\alpha_1 M^{*2} + \gamma_4\left(1 - \gamma_5 M^{*2}\right)\left(P_b - 1\right)\delta_{fe}\tan\alpha_1}{T1\cos\alpha_1 M^*} \tag{C.19}$$

The total to total temperature ratio can be calculated from Equations C.9 to C.11:

$$\frac{T_{t\,m}}{T_{t\,0}} = \frac{T3}{T1} \tag{C.20}$$

The mixed out critical Mach number and exit flow angle are then calculated:

$$M_m^* = \sqrt{M_a^{*2} + M_u^{*2}} \tag{C.21}$$

$$\alpha_m = \tan^{-1}\frac{M_u^*}{M_a^*} \tag{C.22}$$

The exit Mach number is then calculated from the exit critical Mach number:

$$M_m = M_m{}^*\sqrt{\frac{2}{(\gamma + 1)\left(1 - \gamma_5 M_m^{*2}\right)}} \tag{C.23}$$

The ratio of exit to mainstream inlet temperature, pressure and total pressure are then calculated:

$$\frac{T_{s\,m}}{T_{s\,1}} = \frac{T_{t\,m}}{T_{t\,1}} \frac{1+\gamma_1 M_1^2}{1+\gamma_1 M_m^2} \tag{C.24}$$

$$\frac{P_{s\,m}}{P_{s\,1}} = \sqrt{\frac{T_{s\,m}}{T_{s\,0}}} \frac{T1 M_1 \cos\alpha_1}{M_m \cos\alpha_2} \tag{C.25}$$

$$\frac{P_{t\,m}}{P_{t\,1}} = \frac{P_{s\,m}}{P_{s\,1}} \left(\frac{1+\gamma_1 M_1^2}{1+\gamma_1 M_m^2}\right)^{\gamma_3} \tag{C.26}$$

The mainstream entropy loss coefficient is then calculated:

$$\zeta = \left(1 - \frac{P_{t\,m}}{P_{t\,1}}\right) \left(\frac{\gamma}{2} {M_m}^2\right)^{-1} \tag{C.27}$$

Bibliography

[1] ASME/ANSI PTC 19.1-4985. *Measurement Uncertainty*, 1990. The American Society of Mechanical Engineers.

[2] L.R. Anderson, W.H. Heiser, and J.C. Jackson. Axisymmetric One-Dimensional Compressible Flow - Theory and Applications. *ASME Transactions, J. of Applied Mechanics*, 1970. pp. 917-923.

[3] Y. Cai. Aerodynamic performance Measurements in a Fully Scaled Turbine. Master's thesis, Department of Aeronautics and Astronautics, MIT, 1998.

[4] J.D. Denton. Loss Mechanisms in Turbomachines. *ASME J. of Turbomachinary*, 115:621–656, January 1993.

[5] d'Hoop E.M. Flowfield Measurements in a Transonic Turbine. Master's thesis, Department of Aeronautics and Astronautics, MIT, 1995.

[6] M. Drela. An Integral Blundary Layer Formulation for Blunt Trailing Edges. *AIAA*, 1989. 89.2200.

[7] L.M. Grepin. Aerodynamic Measurement and Analysis of the Flow in an Uncooled Turbine. Master's thesis, Department of Aeronautics and Astronautics, MIT, 1998.

[8] G.R. Guenette. *A Fully Scaled Short Duration Turbine Experiment.* PhD thesis, Massachusetts Institute of Technology, 1985.

[9] J.H. Horlock. *Axial Flow Turbines.* Robert E. Keieger Publishing Company, 1973.

[10] J.J. Jacobs. Efficiency Measurements of a Single Stage Turbine in a Short Duration Facility. Master's thesis, Department of Aeronautics and Astronautics, MIT, 1998.

[11] R.C. Keogh. Shaft Efficiency Measurements of a Fully Scaled Turbine in a Short Duration Facility. Master's thesis, Department of Aeronautics and Astronautics, MIT, 1998.

[12] R. Kiock, H. Hoheisel, H.J. Dietrichs, and A.T. Holmes. The Boundary Layer Behaviour of an Advanced Gas Turbine Rotor Blade under the Influence of Simulated Film-Cooling. *AGARD CP 390.* Heat Transfer and Cooling in Gas Turbines, Bergen.

[13] O. Kollen and W. Koschel. Effect of Film-Cooling on the Aerodynamic Performance of a Turbine Cascade. *AGARD CP 390.* Heat Transfer and Cooling in Gas Turbines, Bergen.

[14] M Martinez-Sanchez. *Blade Scale Effects of Tip Leakage*, 1990. GTL report no. 202.

[15] A. Mehra. *Private Correspondence*, 2000.

[16] ASME/ANSI MFC-7M-1987. *Measurement of Gas Flow by Means of Critical Flow Venturi Nozzles*, 1987. The American Society of Mechanical Engineers.

[17] NIST14. *NIST Mixture Property Database*, 1992. NIST Thermophusics Division 838.02, Boulder, Colorado.

[18] C. Osnaghi, A. Perdichizzi, M. Savini, P. Harasgama, and E. Lutum. The Influence of Film-Cooling on the Aerodynamic Performance of a Turbine Nozzle Guide Vane. 1997. 97-GT-522.

[19] M.G. Rose and N.W. Harvey. Turbomachinery Wakes: Differential Work and Mixing Loss. In *ASME J. of Turbomachinary*, 1999. 99-GT-25.

[20] A. Shapiro. *The Dynamics and Thermodynamics of Compressible Fluid Flow: Volume1.* Ronald Press, New York, 1953.

[21] O.P. Sharma and T.L. Butler. Predictions of Endwall Losses and Secondary Flows in Axial Flow Turbine Cascades. In *ASME J. of Turbomachinary*, 1987. 86-GT-228.

[22] C.H. Sieverding, M. Stanislas, and J. Snoek. The Base Pressure Problem in Transonic Cascades. 1983. 97-GT-81.

[23] C.M. Spadaccini. Aerodynamic Performance Measurements of a Fully Scaled, Film-Cooled, Turbine Stage. Master's thesis, Department of Aeronautics and Astronautics, MIT, 1999.

[24] H.H. Youngren. Analysis and Design of Transonic Cascades with Splitter Vanes. Master's thesis, Department of Aeronautics and Astronautics, MIT, 1991.